Elastic, Inelastic, and Photofragment Scattering from Crossed Molecular Beams

Thesis by
Brian Paul Reid

In Partial Fulfillment of the Requirements
for the Degree of
Doctor of Philosophy

California Institute of Technology
Pasadena, California
1986
(Submitted April 4, 1986)

Acknowledgments

Among the people who have helped me with this work, I would especially like to thank my advisor, Randy Sparks, for the opportunity and experience involved in this research. Most of the work described herein has been shared with my coworker, Mike O'Loughlin. He contributed greatly to my understanding, and I enjoyed working with him very much. Tom Dunn deserves thanks for his helpful technical assistance as well as his amiable disposition. I thank my wife, Sally Hair, for, among many things, her unlimited work in the preparation of this thesis.

The laser used in the photodissociation experiments of Chapter 4 was provided by the Jet Propulsion Laboratory. I thank Dave Brinza for his assistance in using it.

Abstract

Three sets of crossed molecular beam scattering experiments are described. In the first experiment, total differential cross sections are measured for collisions between two methane molecules. Treating the scattering as elastic, these cross sections are used to determine an isotropic intermolecular potential energy function for the methane-methane system. The second experiment involves the measurement of total differential cross sections and time-of-flight spectra for neon-chlorine scattering. These data are modeled using the infinite order sudden approximation for rotationally inelastic scattering, and an anisotropic potential function for neon-chlorine is determined. In the third experiment, the angular and time-of-flight distributions for the products of the three-body photofragmentation of 1,2-diiodotetrafluoroethane at 266 nm are measured. These data are analyzed to determine the product translational energy distributions.

Table of Contents

Acknowledgments ii

Abstract iii

List of Figures vi

List of Tables viii

1. Crossed Beams Experiments 1

1.1 The Crossed Beams Apparatus 2

1.2 Experimental Data: Laboratory Differential Cross Sections 5

1.3 Center–of–Mass Differential Cross Sections 8

1.4 Simulation of Experimental Data 9

1.5 Scattering Examples 11

1.6 References 25

2. Methane-Methane Isotropic Interaction Potential 26

2.1 Introduction 27

2.2 Experimental Procedure 28

2.3 Analysis and Results 29

2.4 Discussion 39

2.5 Conclusions 48

2.6 References 50

3. An Anisotropic Interaction Potential for Neon-Chlorine 52

3.1 Introduction 52

3.2 Experimental Procedure 54

3.3 Analysis 56

3.4 Results 67

3.5 Discussion 67

3.6 Conclusions 83

3.7 References 85

4. UV Photodissociation of 1,2-Diiodotetrafluoroethane 87

4.1 Introduction 87

4.2 Experimental Procedure 88

4.3 Analysis 90

4.4 Results 98

4.5 Discussion 107

4.6 Conclusions 111

4.7 References 112

Appendix A. Methane-Methane Laboratory Scattering Intensities 114

Appendix B. Viscosity Calculations 117

B.1 Equations of Viscosity 117

B.2 Numerical Evaluation 119

B.3 Computer Code 120

B.4 References 131

Appendix C. Neon-Chlorine Time-of-flight Data 132

Appendix D. Rotationally Inelastic Scattering Simulation . . . 135

D.1 Computer Code 135

D.2 References 163

List of Figures

Chapter 1. Introduction

Figure 1.1 Top view of crossed molecular beams apparatus 3
Figure 1.2 Side view of crossed molecular beams apparatus 4
Figure 1.3 Velocity vectors of beams and scattered particle 7
Figure 1.4 Center-of-mass and laboratory coordinate systems 10
Figure 1.5 Newton diagram for methane–methane interaction 13
Figure 1.6 CH_4–CH_4 scattering with infinite experimental resolution . . 15
Figure 1.7 CH_4–CH_4 scattering with actual experimental resolution . . 16
Figure 1.8 Newton diagram for Ne–Cl_2 scattering 19
Figure 1.9 Time-of-flight spectrum for neon chlorine scattering 20
Figure 1.10 Newton diagram for photofragmentation of $C_2F_4I_2$ 23

Chapter 2. Methane-Methane Isotropic Interaction Potential

Figure 2.1 Identical particle effects in methane–methane interaction . . 33
Figure 2.2 CH_4–CH_4 potential energy function 36
Figure 2.3 CH_4–CH_4 laboratory scattering intensities 37
Figure 2.4 CH_4–CH_4 second virial coefficient and viscosity data 38
Figure 2.5 CH_4–CH_4 potential compared to other work 45

Chapter 3. An Anisotropic Interaction Potential for Neon-Chlorine

Figure 3.1 Coordinates of an atom–diatom interaction 58
Figure 3.2 Ne–Cl_2 total angular distributions 69
Figure 3.3 Ne–Cl_2 time–of–flight spectra 70
Figure 3.4 Ne–Cl_2 equipotential contour plot 71
Figure 3.5 Ne–Cl_2 potential energy function at $\gamma = 0°$ and $90°$ 72
Figure 3.6 Legendre expansion of the Ne–Cl_2 potential 73
Figure 3.7 Differential cross sections versus final rotational state 78
Figure 3.8 Ne–Cl_2 angular distributions with $r_{m\perp}$=3.5Å 82

Chapter 4. UV Photodissociation of 1,2-Diiodotetrafluoroethane

Figure 4.1 Newton diagram for the photodissociation of $C_2F_4I_2$ 91

Figure 4.2a Time-of-flight spectra of iodine at 10°, 15°, 20°, and 25° . . 99

Figure 4.2b Time-of-flight spectra of iodine at 30°, 40°, and 50°. . . 100

Figure 4.3 Time-of-flight spectra of C_2F_4 at 20° and 30°. 101

Figure 4.4 Total angular intensity of iodine 103

Figure 4.5 Energy flux distribution for the first dissociation 104

Figure 4.6 Energy flux distribution for the second dissociation 105

Figure 4.7 Angular distribution for the second dissociation 106

List of Tables

Chapter 2. Methane-Methane Isotropic Interaction Potential

Table 2.1 Beam source characteristics 30

Table 2.2 MMSV potential parameters CH_4–CH_4 35

Table 2.3 Rms deviations for CH_4–CH_4 potentials 43

Table 2.4 Potential parameters for CH_4 and Kr systems 49

Chapter 3. An Anisotropic Interaction Potential for Neon-Chlorine

Table 3.1 Neon and chlorine beam source characteristics 55

Table 3.2 Potential parameters for Ne–Cl_2 68

Chapter 4. UV Photodissociation of 1,2-Diiodotetrafluoroethane

Table 4.1 Beam source characteristics for $C_2F_4I_2$ 89

Appendix A. Methane-Methane Experimental Data

Table A.1 Methane-Methane data, 1080 K collision energy 114

Table A.2 Methane-Methane data, 745 K collision energy 115

Table A.3 Methane-Methane data, 448 K collision energy 116

Appendix C. Neon-Chlorine Experimental Data

Table C.1 Neon-chlorine data, 1476 K collision energy 132

Table C.2 Neon-chlorine time-of-flight data 133

Chapter 1
Crossed Beams Experiments

The crossed molecular beams technique is a versatile method for studying molecular interactions. Applications of crossed beams experiments can involve elastic, inelastic, and reactive scattering processes. Since these processes are strongly dependent upon intermolecular potential energy surfaces, crossed beams data can provide details, often difficult to obtain using other methods, about features of the potentials.

This thesis describes three sets of experiments, all performed with a crossed molecular beams apparatus. The first experiment is an attempt to quantify the methane-methane interaction using an isotropic potential energy function and treating the scattering as elastic. The second examines the elastic and inelastic processes of the neon-chlorine molecule interaction and results in an anisotropic intermolecular potential. The third describes the energy partitioning in the fragmentation processes which occur when 1,2-diiodotetrafluoroethane absorbs an ultraviolet photon.

This first chapter provides an introduction to the crossed beams apparatus and the type of data obtained. The first section describes the apparatus, and the second introduces the fundamental datum of a scattering experiment, the differential cross section, from an experimental viewpoint. Then follows a discussion of scattering experiments using the systems of this work as examples. This lays groundwork for the understanding of the following chapters which relate the details of the three experiments.

1.1 The Crossed Beams Apparatus

Crossed beams instruments are designed to monitor the scattering which occurs when particles in two intersecting beams collide. Detailed observation of the scattered particles, with spatial and energy resolution, provides data with which to reconstruct the collision and subsequent processes. Since the convolution of many different sorts of collisions which lead to the same observation makes the reconstruction process difficult, if not impossible, the collision conditions must be well defined. The requirements for detection resolution and collision conditions underlie the design of the apparatus used to perform the experiments described herein.

The instrument is a high resolution Sparks version[1] of a crossed beams instrument described by Lee, *et al.*[2] Details particular to the apparatus used have been documented[3] and only a brief overview is given here. A schematic top view of the instrument is shown in Figure 1.1 and a more detailed cross section in Figure 1.2. The design has several features which are highly advantageous for crossed beams experiments. The molecular beam sources are designed for supersonic expansions which provide intense beams with narrow velocity distributions. Two stages of differential pumping and small defining apertures allow well collimated beams to enter the scattering chamber. The scattering chamber is precision machined so that the beams can be aligned at a right angle. This main chamber of the apparatus provides a high vacuum ($\approx 2 \times 10^{-8}$ torr) region to ensure single collision events between particles in the beams. An ultrahigh vacuum (partial pressures less than 10^{-10} torr) chamber rotates in the plane of the molecular beams and about their intersection. This chamber houses an electron impact ionizer, a quadrupole mass filter, and an ion detection system

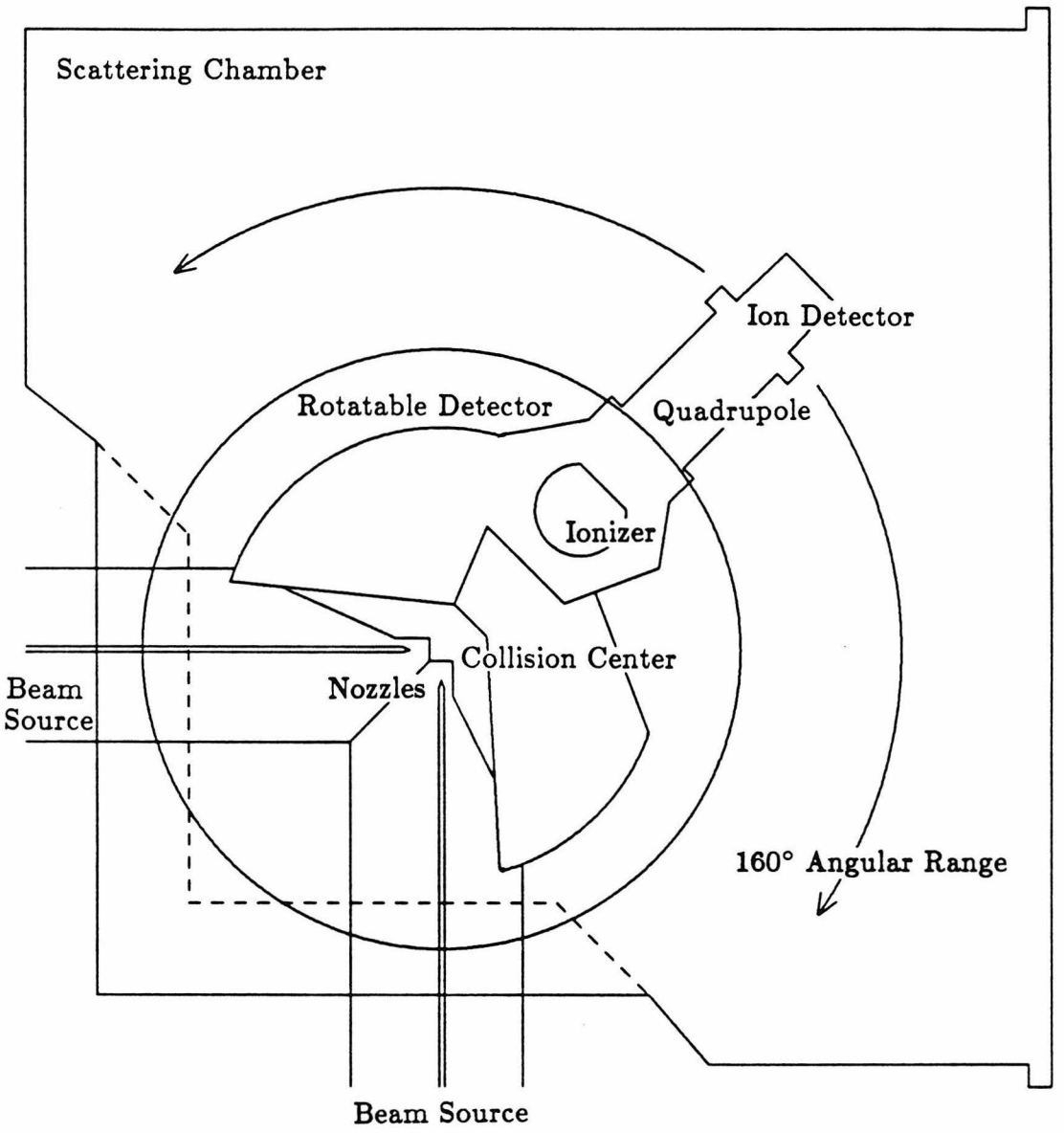

Figure 1.1 Top view of the crossed molecular beams apparatus. (Figure adapted from Reference (1).)

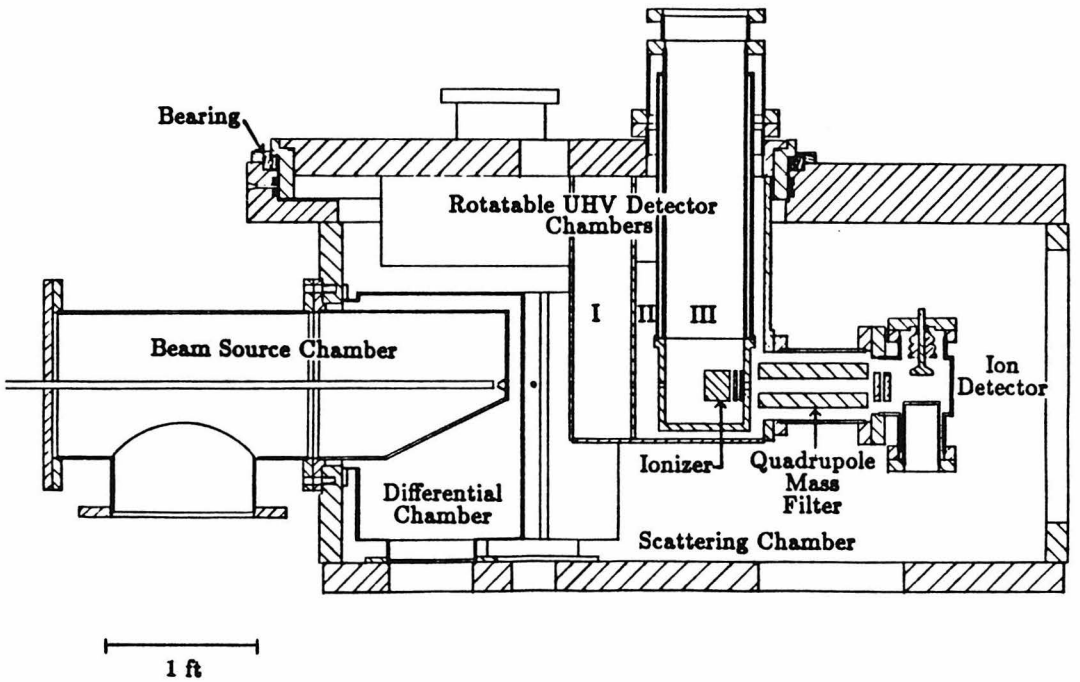

Figure 1.2 Side view of crossed molecular beams apparatus. (Figure from Reference (3).)

to form a "universal" detector for chemical species. Three differential pumping regions (labeled I, II, and III in Figure 1.2) within the rotating detector produce the low partial pressures required for sensitive detection of scattered products. The rotation of the detector and its small collimating apertures allow for the determination of spatial scattering distributions.

The instrumental design allows for several relatively easy modifications. Two important modifications were used in the present work. One is the placement of a rotating slotted disk in front of the detector opening. This provides a means to measure the translational energy of scattered particles and of incident beams by measuring the time of flight of the particles. The 30 cm flight path from the wheel to the ionizer and the $\approx$ 1 cm ionizer length determine the translational energy resolution. The second modification is the replacement of one of the molecular beam sources with a window through which a laser beam may pass. This allows the interactions of photons and molecules, photofragmentation processes in particular, to be studied.

1.2 Experimental Data: Laboratory Differential Cross Sections

The preceeding section described an instrument which can detect scattered particles at a specific angle and with a particular time-of-flight over a known flight path. These quantities define a laboratory velocity vector, and it is convenient to look at velocity vector diagrams, called "Newton" diagrams, in order to understand and analyze scattering experiments. Consider a general experiment with the scattering of molecules 1 and 2 resulting in 3 and 4:

$$1 + 2 \rightarrow 3 + 4 \tag{1.1}$$

Figure 1.3 shows a perspective diagram defining the directions of the beam velocities, $\mathbf{V_1}$ and $\mathbf{V_2}$, and the laboratory scattering angles Θ and Φ for particle 3 scattered with velocity $\mathbf{V_3}$. The diagram also shows the rotation axis of the detector and the angular limits of the detector opening centered at the angles $\Theta_0 = \Theta$ and $\Phi_0 = 0$. Figure 1.3 illustrates that the detector accepts scattering over a range of angles defined by the solid angle, $\Delta\Omega$, subtended by the detector. The time resolution of the detector will also be finite. The experimentally determined quantity, $S_3(\tau_n, \Theta_0, \Phi_0; \mathbf{x})$, will be the number of particles of type 3 which are detected per unit time with the detector located in the direction defined by the angles Θ_0 and Φ_0 and having times of flight in a range $\Delta\tau$ centered at τ_n. The parameter $\mathbf{x}$ includes all of the experimental parameters upon which S_3 depends. The important components of $\mathbf{x}$ are the spatial, velocity, and internal state distributions of the beams and the geometry, efficiency, and state selection of the detector. In order to relate the quantity S_3 to other experiments and to theory, it is desirable to obtain a distribution which is independent of the parameters particular to a given instrument. First we define a quantity, $\frac{d^2\sigma}{dV_3 d\Omega}(V_3, \Theta, \Phi; \mathbf{E}_{Lab})$, by Equation 1.2:

$$\frac{d^2\sigma}{dV_3 d\Omega}(V_3, \Theta, \Phi; \mathbf{E}_{Lab}) = \lim_{\mathbf{x}\to\infty}\left[\frac{S_3(\tau, \Theta, \Phi; \mathbf{x})}{\Delta V \Delta\Omega F_{rel} D}\right]. \tag{1.2}$$

The parameter $\mathbf{E}_{Lab}$ contains the limiting velocities and internal states of the beams, as well as the internal states of the scattered particles. To make $\frac{d\sigma}{d\Omega}$ independent of the experimental apparatus, S_3 is first divided by those parameters to which it is directly proportional: the relative flux of colliding particles, F_{rel}, the solid angle subtended by the detector, $\Delta\Omega = \Delta\cos\Theta\Delta\Phi$, the detector efficiency, D, and the velocity interval corresponding to the time interval over which S was measured, ΔV. When $\Delta\Omega$, ΔV, and all beam spreads go to

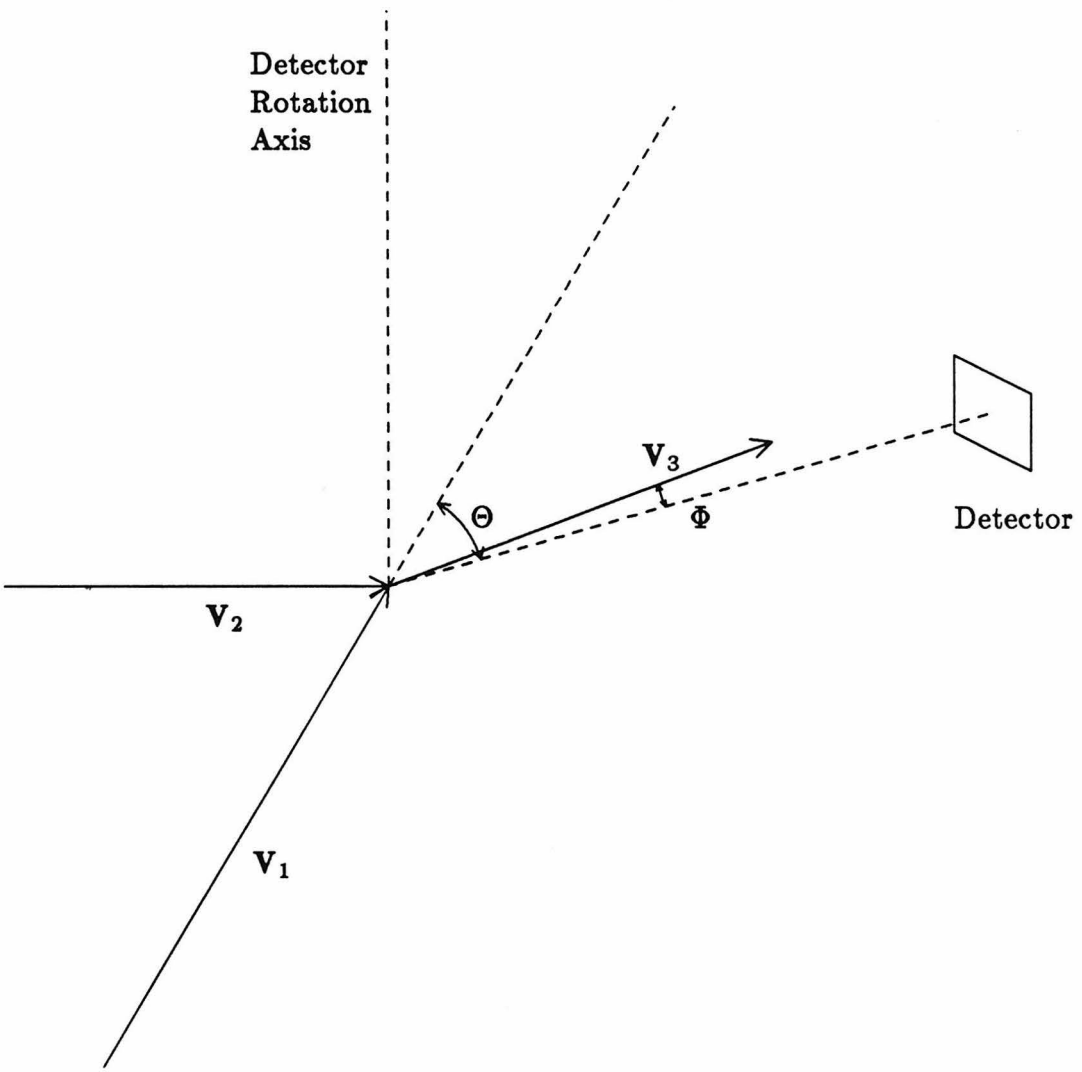

Figure 1.3 Velocity vector diagram showing beam velocity directions and a velocity vector of a scattered particle. The scattered velocity vector $\mathbf{V}_3$ makes the angle Θ in the plane and Φ out of the plane formed by the beams. The detector rotates about the indicated axis and is in the plane formed by the two beams.

zero $\frac{d^2\sigma}{dV_3 d\Omega}$ becomes independent of the experimental resolution. The limit in Equation 1.1 represents this limit of infinite experimental resolution. The quantity $\frac{d^2\sigma}{dV_3 d\Omega}$ is termed a laboratory double differential cross section. It is a differential quantity with respect to Ω and V_3, and as a cross section has units of area per unit velocity per unit solid angle. Physically, this is the probabiltity distribution function per unit incident flux per unit time for scattering at (Θ, Φ) with velocity V_3.

1.3 Center-of-Mass Differential Cross Sections

A further simplification of the scattering data is to reduce the dependence of $\frac{d^2\sigma}{dV_3 d\Omega}$ on both beam velocities to a dependence upon only the relative velocity. This is done by transforming $\frac{d^2\sigma}{dV_3 d\Omega}$ to the center-of-mass coordinate system. The center of mass is defined so that it has the position coordinate, $\mathbf{R}_{cm}$, given in Equation 1.3,

$$\mathbf{R}_{cm} = \frac{m_1}{M}\mathbf{R_1} + \frac{m_2}{M}\mathbf{R_2}, \tag{1.3}$$

in which m_1 and m_2 are the masses of the particles in the two beams, $\mathbf{R_1}$ and $\mathbf{R_2}$ are their position vectors and $M = m_1 + m_2$. If $\mathbf{V}_{cm}$ is the vector which describes the time rate of change of $\mathbf{R}_{cm}$, then the reference frame which has velocity $\mathbf{V}_{cm}$ in the laboratory frame is commonly termed the "center-of-mass" frame. Since, in a Hamiltonian representing the system, any potential energy function will be independent of $\mathbf{R}_{cm}$ and the absolute orientation of the system, the motion of $\mathbf{R}_{cm}$ may be factored out of the system. The motion which cannot be factored out is the relative motion within the center-of-mass system. This can be described by only one coordinate, $\mathbf{r}_{12} = \mathbf{R_1} - \mathbf{R_2}$ whose time rate of change is $\mathbf{v}_{12}$. The relationships between $\mathbf{V}_{cm}$, $\mathbf{v}_{12}$ and the beam velocities in

the laboratory, $\mathbf{V}_1$ and $\mathbf{V}_2$, and in the center-of-mass system, $\mathbf{v}_1$ and $\mathbf{v}_2$, are conveniently summarized in the Newton diagram of Figure 1.4.

Since the important motion is in the center-of-mass system, the fundamental theoretical quantity to relate to a scattering experiment is the center-of-mass differential cross section, $\frac{d^2\sigma}{dvd\omega}(v,\theta,\phi;E)$, where the lower case variables are analogous to the upper case variables in the laboratory frame. The factor which relates the center-of-mass differential cross section to the laboratory differential cross section is, as it is for any coordinate transformation of differential quantites, the Jacobian, $J_{Lab\rightarrow cm} = J(\frac{V_3,\Omega}{v_3,\omega})$, of transformation between the two reference frames:

$$\frac{d^2\sigma}{dv_3d\omega} = J(\frac{V_3,\Omega}{v_3,\omega})\frac{d^2\sigma}{dV_3d\Omega}. \tag{1.4}$$

In all situations encountered here, the center-of-mass differential cross sections are independent of ϕ and hence this variable will be dropped from the notation.

1.4 Simulation of Experimental Data

If the experiment is of high resolution and the system being studied is amenable, the center of mass differential cross sections may be extracted from the measured quantity S_3. In all the work detailed herein, however, this approach was presumed not to be reliable. Instead, trial-and-error procedures were used in which center-of-mass differential cross sections are estimated, either theoretically or empirically, and then convoluted over the experimental parameters to calculate an estimate for S_3. This procedure is repeated until the calculated and experimental distributions are the same. The procedure for convoluting the center-of-mass cross sections can be quantified by reversing the

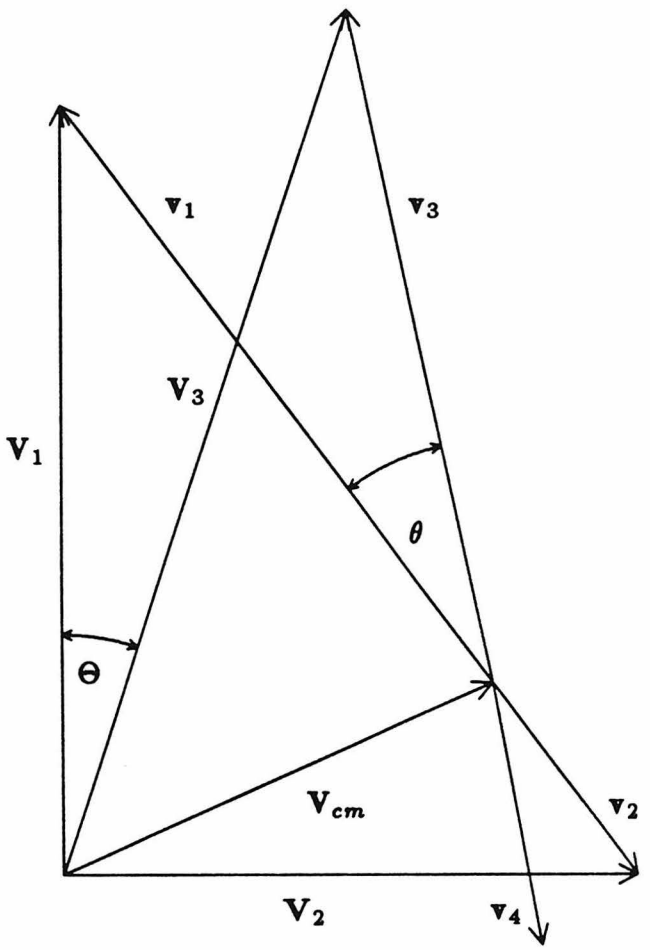

Figure 1.4 Relation of center-of-mass coordinates (lower case) to laboratory coordinates (upper case).

procedure used above to go from S_3 to $\frac{d^2\sigma}{dv_3 d\omega}$. Equation 1.5 gives a schematic view of this:

$$S_3(\tau_n, \Theta_0; \mathbf{x}) = \int_{\mathbf{x}} \frac{d^2\sigma}{dv_3 d\omega} J(\frac{v_3, \omega}{V_3, \Omega}) D F_{rel}\, dV_3\, d\Omega\, d\mathbf{x}. \tag{1.5}$$

Since the detector of the apparatus can only rotate in the plane defined by the molecular beams, Φ_0 is constant, can be taken as zero, and is dropped from the notation. Explicitly including the averaging over the instrument parameters contained in $\mathbf{x}$ and relating the relative flux to the velocity number densities of the beams, $n_1(\mathbf{V}_1, \mathbf{r}_c)$ and $n_2(\mathbf{V}_2, \mathbf{r}_c)$, the relative velocity and the collision volume, $\int d\mathbf{r}_c$, we can write equation 1.6:

$$\begin{aligned} S_3(\tau_n, \Theta_0; \mathbf{x}) = & \int_{\mathbf{r}_c} \int_{\mathbf{V}_2} \int_{\mathbf{V}_1} \int_{\Omega} \int_{\tau} \frac{d^2\sigma}{dv_3 d\omega} \\ & \times J(\frac{v_3, \omega}{V_3, \Omega}) n_1 n_2 v_{12} J(\frac{V_3}{\tau}) D\, d\tau\, d\Omega\, d\mathbf{V}_1\, d\mathbf{V}_2\, d\mathbf{r}_c. \end{aligned} \tag{1.6}$$

Each integral over a vectoral quantity denotes three scaler integrals over each of the vector components. The Jacobian, $J(\frac{V_3}{\tau})$, from velocity space to time space is included to transform the integration into time. The integration over τ includes all appropriate factors concerning the finite resolution of the ionizer and the time-of-flight wheel slits.

1.5 Scattering Examples

Equation 1.5 shows the bridge between theoretically calculated quantities, $\frac{d^2\sigma}{dvd\omega}$, and the experimental scattering signal, S. The expression is fairly general in nature, and all the simulations of experimental data described here are special cases of this equation. This section describes in more detail these special cases. In doing so, each of the experiments of the following chapters is introduced.

1.5.1 Methane-Methane Scattering

A representative Newton diagram for the methane-methane scattering of Chapter 2 is shown in Figure 1.5. The analysis in Chapter 2 assumes that the scattering is elastic, *i.e.*, the relative translational energy and thus the magnitudes of the methane velocities in the center-of-mass system are the same before and after collision. For a "spherical" molecule such as methane, this could be a reasonable approximation. In the case of elastic scattering, the conservation of energy and momentum constrain the velocity vectors of the scattered products to lie on a sphere centered at the tip of V_{cm} (see Figure 1.5). Since the speed, v_3, of the detected particle in the center-of-mass frame is not an independent variable, a cross section differentiated with respect to v_3 is unnecessary. To maintain the formalism of Equation 1.5 we can write:

$$\frac{d^2\sigma}{dv_3 d\omega}(v_3, \theta; \mathbf{E}) = \frac{d\sigma}{d\omega}(\theta; \mathbf{E})\delta(v_3 - v_s), \tag{1.7}$$

in which v_s is the scattered speed in the center-of-mass system. This has the effect of eliminating the integration over t (or V_3) in Equation 1.6 and allows the scattering to be measured only as a function of angle. The Jacobian, $J(\frac{\omega}{\Omega})$, now does not include a transformation between the speed coordinates and becomes

$$J(\frac{\omega}{\Omega}) = \frac{V_3^2}{v_3^2 \cos\delta}, \tag{1.8}$$

where δ is the angle between $\mathbf{v}_3$ and $\mathbf{V}_3$.[4] Combining Equations 1.7 and 1.8 in Equation 1.6 yields

$$S_3(\Theta_0; \mathbf{x}) = \int_{\mathbf{r}_c}\int_{\mathbf{V}_2}\int_{\mathbf{V}_1}\int_{\Omega} \frac{d\sigma}{d\omega} \times \frac{V_3^2}{v_3^2 \cos\delta} n_1 n_2 v_{12} D \, d\Omega \, d\mathbf{V}_1 \, d\mathbf{V}_2 \, d\mathbf{r}_c. \tag{1.8}$$

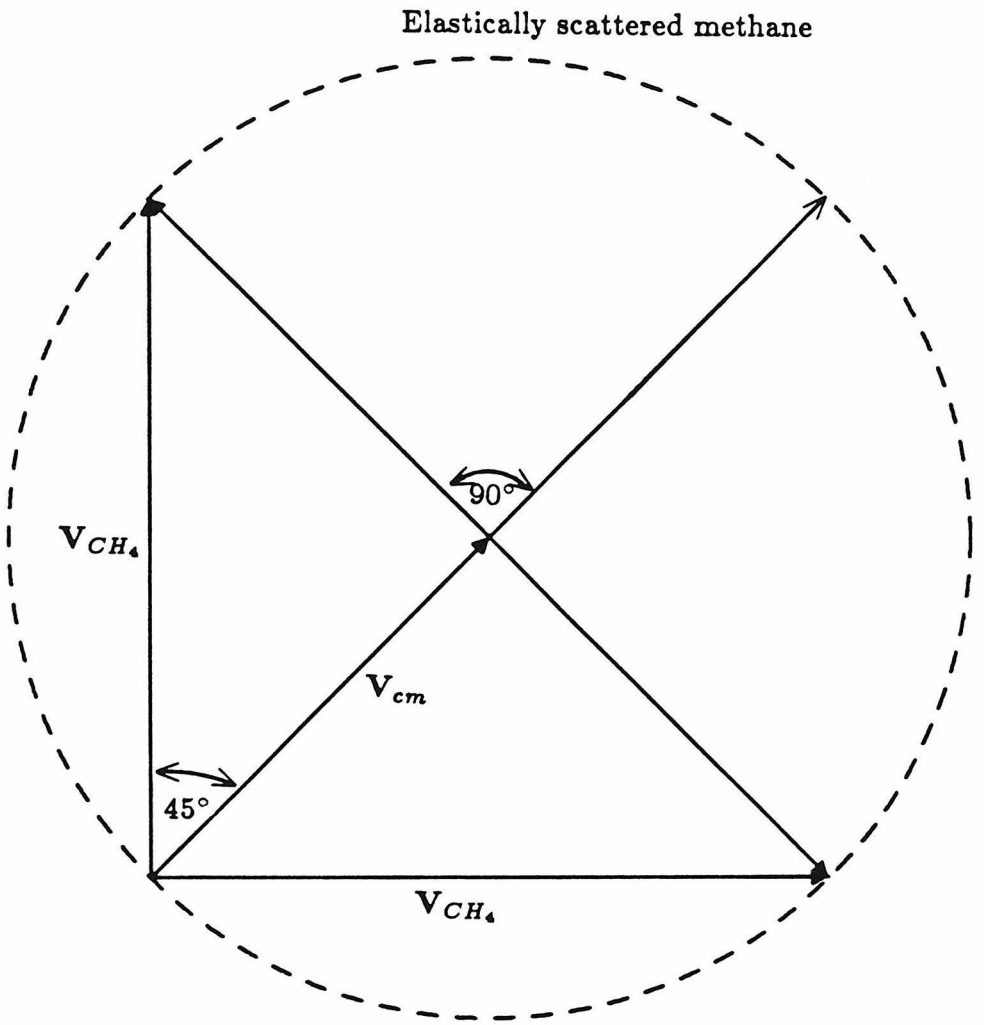

Figure 1.5 A Newton diagram for methane-methane elastic scattering.

The symmetry of the methane-methane system allows a scan of 90° in the center-of-mass frame to cover all possible scattering and this translates, as seen in Figure 1.5, into 45° in the laboratory frame. The features of elastic scattering from a weak, van der Waals type of attraction can be expected over this region. These features can be observed in the theoretical calculation for the methane-methane system shown in Figure 1.6. This calculation corresponds to the limit of infinite experimental resolution. The scattering is usually strongly peaked in the forward direction, that of the incident beam at 0° (although for methane-methane scattering it is impossible to tell from which beam the detected particle came), and has an exponential decrease with increasing scattering angle. Two types of oscillatory behavior are often observed. Rainbow oscillations are large period undulations which arise from the potential having an attractive well. The broad hump in Figure 1.6 between 9 and 16° is a rainbow maximum. There are also higher frequency oscillations which are related to diffraction effects during the scattering process. These oscillations are useful in determining the range of the interaction. The oscillations seen in Figure 1.6 are significantly damped in actual experimental data due to the averaging processes embodied in Equation 1.9. When these averaging effects are included the scattering appears as shown in Figure 1.7. In the methane-methane case, a third sort of oscillation can arise from symmetry restrictions upon the wave functions of systems with identical particles. The scattering from normal methane, as described in Chapter 2, will result in a combination of contributions from even wave functions, odd wave functions and even plus odd wave functions The effects on the observed scattering can be seen in the interference effects at angles larger than 12° in Figure 1.7.

When the interaction is quantified in an isotropic potential energy function, elastic scattering differential cross sections can be easily calculated using well

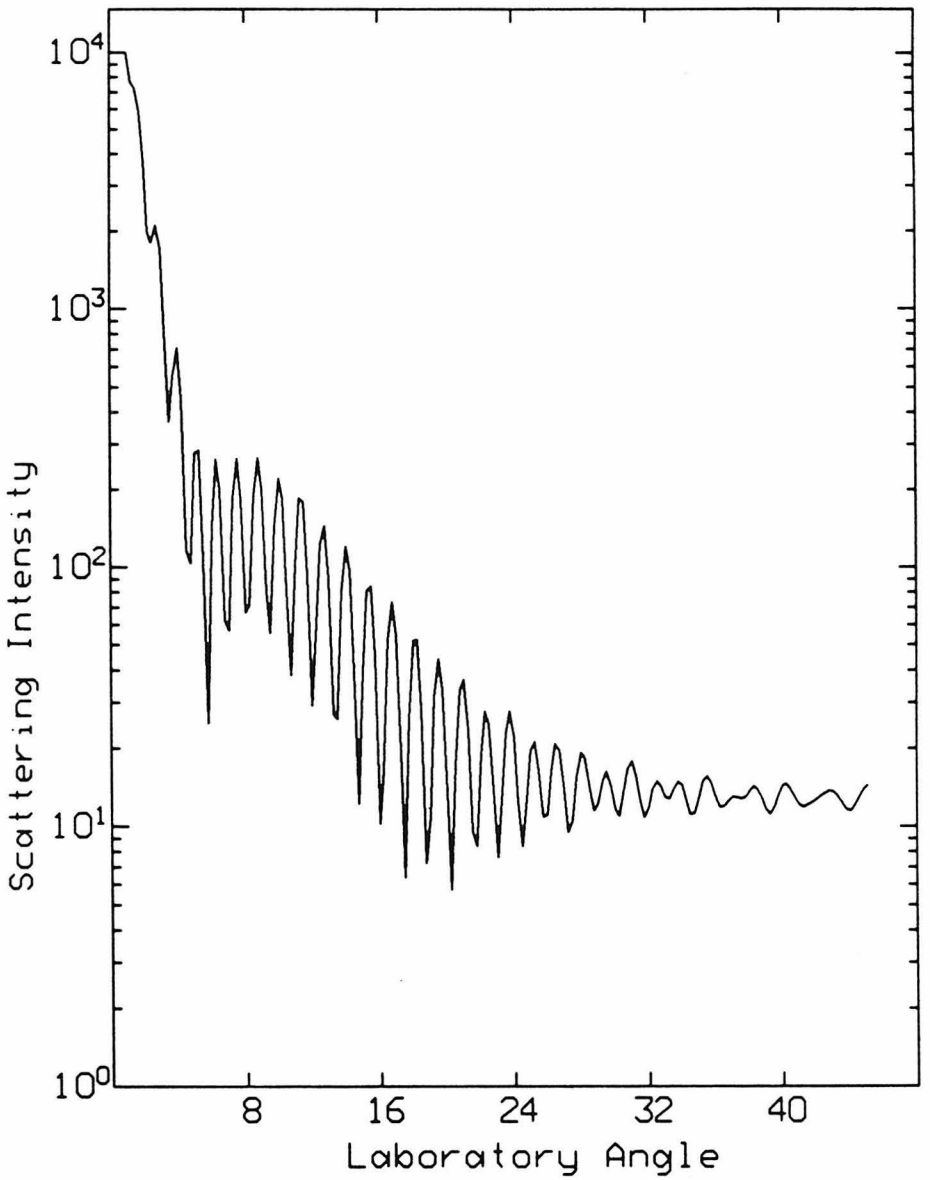

Figure 1.6 A calculation of methane-methane scattering from a spherical potential with infinite experimental resolution. The collision energy is 745 Kk_B, where k_B is the Boltzmann constant. The rapid diffraction oscillations and the rainbow maximum are clearly visible.

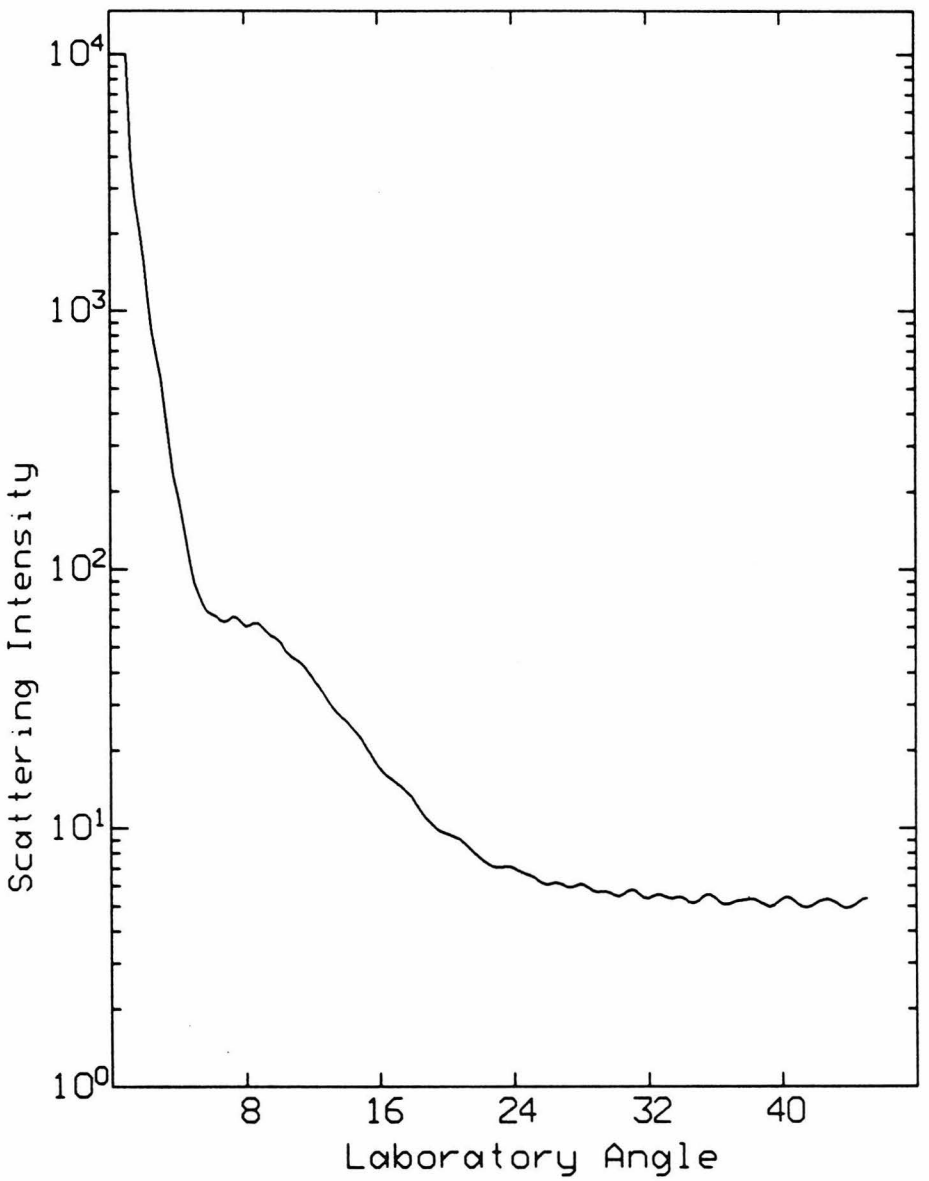

Figure 1.7 A calculation of methane-methane scattering from a spherical potential with the effects of instrument averaging included. The diffraction oscillations are severely quenched but are still visible around 8°. The rainbow maximum is clearly resolved. Interference patterns which arise from symmetry restrictions upon the methane-methane wavefunctions are visible down the outer side of the rainbow structure and at large angles.

developed theory.[5] Variation of an estimated potential until the calculated scattering fits the experimental data, as done in Chapter 2, provides an empirical potential which can be used in modeling other methane and methane-like interactions.

1.5.2 Neon-Chlorine Inelastic Scattering

The neon-chlorine system should be significantly more anisotropic than the spherical-like methane-methane system. This suggests that a spherical approximation will probably fail. It also implies that there will be significant inelastic transitions. At low collision energies the inelasticity is rotational. Although the scattering is not confined to a single velocity as it is for elastic scattering, it is confined to a set of discrete velocities corresponding to the discrete rotational energy states of the chlorine molecule. Thus, the center-of-mass differential cross sections are not continuous with respect to velocity, but there are a set of differential cross sections to cover the range of inelastic transitions energetically available. Equation 1.10 is the analog for discrete inelastic scattering of Equation 1.7 for elastic scattering:

$$\frac{d^2\sigma}{dv_3 d\omega}(v_3, \theta; \mathbf{E}) = \sum_{if} \frac{d\sigma}{d\omega}(\theta; i \rightarrow f, E)\delta(v_3 - v_{if}). \tag{1.10}$$

In this equation, v_{if} represents the center-of-mass velocity of the detected particle scattered from initial state i to final state j. Since the rotational constant, B_e, of chlorine is small, we cannot resolve individual rotational energy states experimentally. This results in a continuous laboratory time-of-flight spectrum and prohibits the direct determination of the state-to-state differential cross sections suggested by Equation 1.10. Modeling of the data must again be done by using Equation 1.6. Since the velocities in the center-of-mass system are discrete,

the Jacobian of equation 1.8 must be used. This is troublesome, as can be seen by studying Figure 1.8, a Newton diagram for the neon-chlorine system. The Jacobian is numerically well behaved in many cases, for example, the detection of the neon at velocities near elastic scattering velocities. But consider the scattered chlorine when the detector is placed such that the laboratory velocity, $\mathbf{V}_{Cl_2}$, is perpendicular to the center-of-mass velocity, $\mathbf{v}_{Cl_2}$. This results in a singularity in the Jacobian since $\frac{1}{\cos\delta}$ goes to infinity at this point. Physically this is a laboratory angle, one side of which there can be no scattering at the given inelastic transition and the other side of which there can be. The scattering probability density distribution will therefore go to inifinity at this point. Of course, $\frac{d\sigma}{d\Omega}\Delta\Omega$ will be finite, but the explicit inclusion of the Jacobian in a quadrature is numerically dangerous. A reasonable alternative is to transform the limits of integration over the detector to the limits in the center-of-mass frame and remove the explicit form of the Jacobian. If this is done only for the Θ variable, then, for the detection of chlorine, Equation 1.6 becomes:

$$S_{Cl_2}(\tau_n, \Theta_0; \mathbf{x}) = \int_{\mathbf{r}_c}\int_{\mathbf{V}_2}\int_{\mathbf{V}_1}\int_{\tau}\int_{\Phi}\int_{\theta}\sum_{if}\frac{d\sigma}{d\omega}(\theta; i \rightarrow f, E)J(\frac{\phi}{\Phi})$$
$$\times n_1 n_2 v_{12} J(\frac{V_{Cl_2}}{\tau}) D\, d\theta\, d\Phi\, d\tau\, d\mathbf{V}_1\, d\mathbf{V}_2\, d\mathbf{r}_c. \qquad (1.11)$$

Time-of-flight distributions calculated from Equation 1.11 are shown in Figure 1.9. The distributions are for detection of chlorine scattered from neon with the detector at an angle of 14° from the chlorine beam. The two peaks correspond to scattering on opposite sides of the Newton circles show in Figure 1.8 and in the inset in Figure 1.9. The peaks are at different center-of-mass angles but, since 14° is near the velocity of the center of mass, each peak contains contributions from only a small range of center-of-mass angles. The figure shows

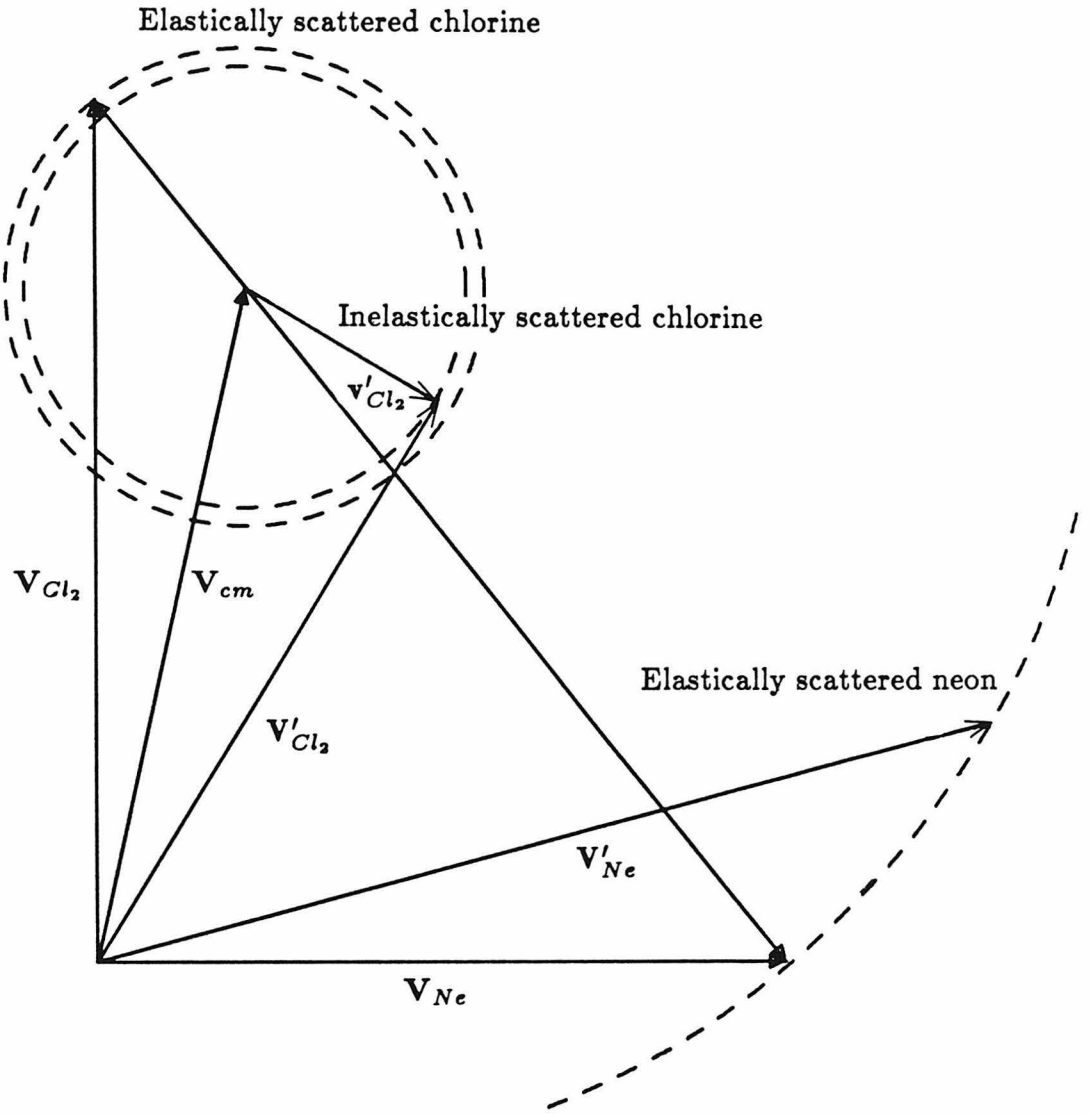

Figure 1.8 A Newton diagram for neon-chlorine scattering. The primed vectors refer to velocities of scattered particles.

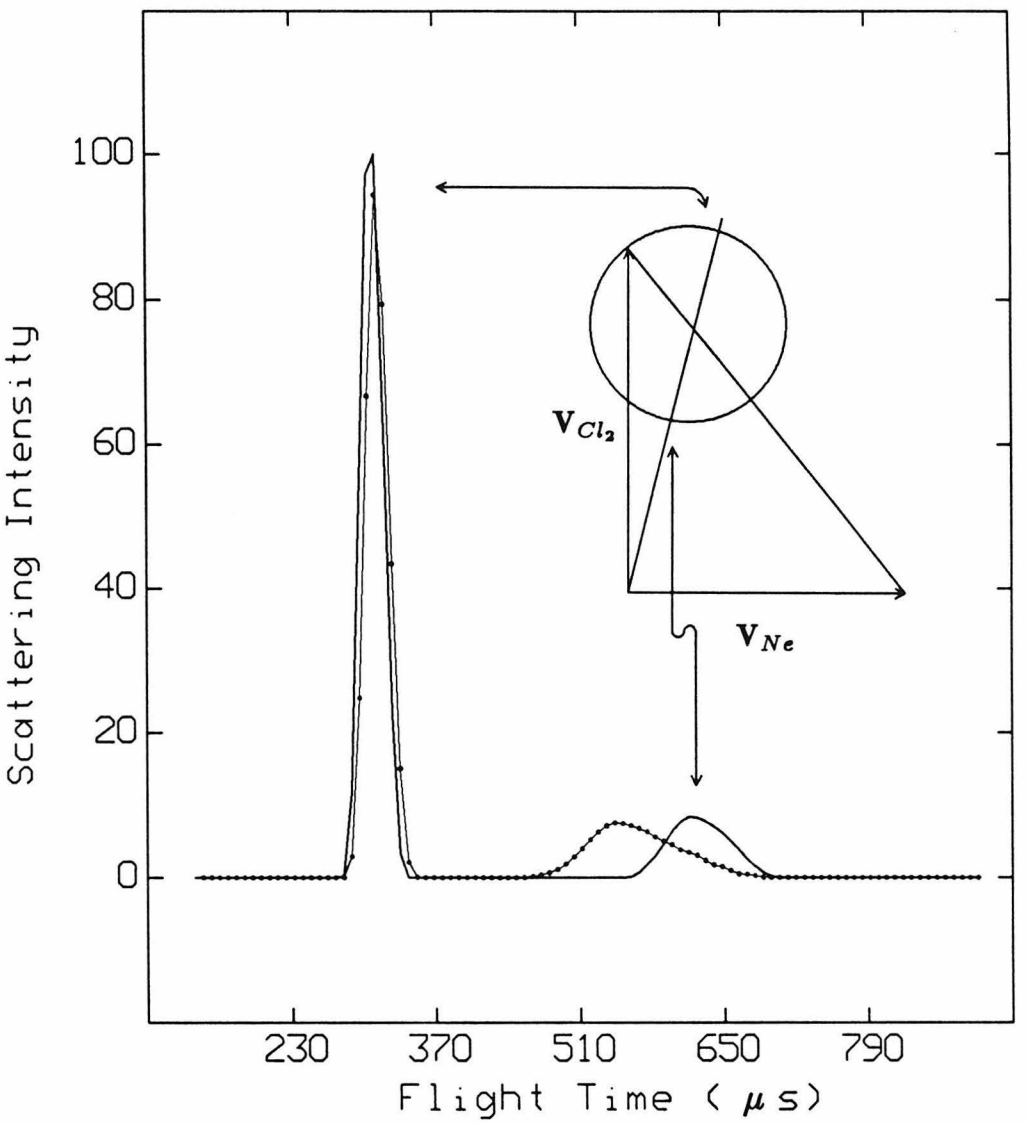

Figure 1.9 Time-of-flight spectrum calculated for chlorine scattering from neon. The heavy line shows elastic scattering from a spherical potential averaged over the experimental conditions in Chapter 3. The dotted line is inelastic scattering from an anisotropic potential. The inset Newton diagram shows the regions in velocity space which correspond to the time-of-flight peaks.

the difference between elastic scattering from a spherical potential and inelastic processes from an anisotropic potential. The amount of inelastic scattering is very sensitive to the anisotropy of the potential energy function.

Integrating the time-of-flight spectra over time produces angular distributions which are akin to summing the state-to-state differential cross sections at a given center-of-mass angle. These angular distributions are termed laboratory total differential cross sections and they show the same sort of behavior as the elastic scattering cross sections discussed in the previous section. The oscillatory features are not as sharp, however, since the anisotropic potential and the resulting inelastic scattering smear them out.

To complete the theoretical calculation of the scattering, all that is needed is an estimate of the state-to-state center-of-mass differential cross sections. These can be calculated from an anisotropic intermolecular potential by use of the infinite order sudden approximation (IOSA),[6] which is expected to be reasonable for the neon-chlorine system. A brief outline of the IOS approximation is provided in Chapter 3 while details of the exact calculations are provided by the computer code in Appendix D. Fitting both the time-of-flight spectra and angular distributions calculated from an estimated potential energy function to the experimental data allows the anisotropic interaction to be quantified.

1.5.3 Photodissociation of 1,2-Diiodotetrafluoroethane

The last example of scattering experiments is the photodissociation of 1,2-diiodotetrafluoroethane. In this instance one of the molecular beams has been replaced by an ultraviolet laser. We can postulate two processes occuring:

$$C_2F_4I_2(1) + h\nu(2) \rightarrow C_2F_4I(3) + I(4), \qquad (1.12a)$$

and

$$C_2F_4I(3) \rightarrow C_2F_4(5) + I(6). \qquad (1.12b)$$

Figure 1.10 shows a Newton diagram of the situation and depicts possible scattering of the products. In this experiment, the beam velocity, $\mathbf{V}_{C_2F_4I_2}$ is the velocity of the center of mass, $\mathbf{V}_{cm}$. The first dissociation, Equation 1.12a, produces the fragments C_2F_4I and I with the velocities $\mathbf{v}_{C_2F_4I}$ and $\mathbf{v}_{I(4)}$ in the center-of-mass frame. After some length of time the C_2F_4I fragment, internally excited from the initial dissociation, unimolecularly fragments to produce C_2F_4 and I with velocities $\mathbf{w}_{C_2F_4}$ and $\mathbf{w}_{I(6)}$ measured in the reference frame of the C_2F_4I radical.

The internal states of the polyatomic fragments are densely spaced and cannot be resolved experimentally. We can treat the differential cross sections as if they were true continuous functions of velocity, just as originally defined in Equation 1.4. Equation 1.6 simplifies in this case because one of the molecular beams has been eliminated. For example, the calculation of the scattering of the iodine from the first dissociation process can be described by Equation 1.13:

$$S_{I(4)}(\tau_n, \Theta_0; \mathbf{x}) = \int_{\mathbf{r}_c} \int_{\mathbf{V}_1} \int_{\Omega} \int_{\tau} \frac{d^2\sigma}{dv_4 d\omega} J\left(\frac{v_4, \omega}{V_4, \Omega}\right) n_1 f_2 J\left(\frac{V_4}{\tau}\right) D \, d\tau \, d\Omega \, d\mathbf{V}_1 \, d\mathbf{r}_c. \qquad (1.13)$$

The photon flux is given by f_2. The actual detected signal of iodine will include contributions from both dissociation processes. The calculation of the differential cross sections for the products from the second dissociation is complicated by the convolution of all possible outcomes of the first process.

The fitting of the center-of-mass angular distributions of the scattering from the first dissociation provides information about the orientation of the

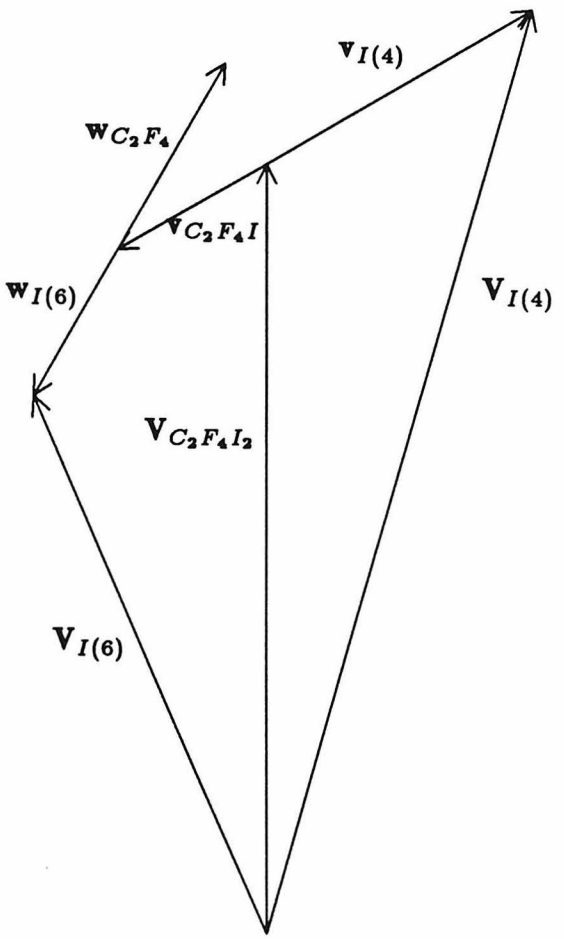

Figure 1.10 A Newton diagram for the photofragmentation of 1,2-diiodotetrafluoroethane.

electronic transition moment for the photon absorption with respect to the C-I bond which fractures.[7] The angular distribution of the second dissociation is somewhat dependent upon the lifetime of the C_2F_4I fragment. The translational energy distributions can indicate the dynamics and energy partitioning, including electronic excitation of the iodine, in the dissociation processes. The details are presented in Chapter 4.

1.6 References

[1] R.K. Sparks, *Ph.D. Thesis* (University of California, Berkeley, 1979).

[2] Y.T. Lee, J.D. McDonald, P.R. LeBreton and D.R. Herschbach, Rev. Sci. Instrum. **40**, 1402–1408 (1969).

[3] M.J. O'Loughlin, *Ph.D. Thesis* (California Insititute of Technology, Pasadena, 1986).

[4] For a discussion of transformation Jacobians with respect to differential cross sections see, G.L. Catchen, J. Husain, and R.N. Zare, J. Chem. Phys. **69**, 1737 (1978).

[5] See, for example, H. Pauly, in *Atom - Molecule Collision Theory: A Guide for the Experimentalist*, edited by R.B. Bernstein (Plenum Press, New York, 1979), Chapter 4.

[6] For a review of the IOSA see, D.J. Kouri, *ibid*, Chapter 9.

[7] For a review of photofragmentation dynamics see, S.R. Leone, Adv. Chem. Phys. **44**, 255 (1982).

Chapter 2
Methane-Methane Isotropic Interaction Potential*

Abstract

Total differential cross sections (DCS) for methane-methane scattering at three collision energies were determined using the crossed molecular beams technique. These DCS's were used along with literature viscosity and second virial coefficient data to determine a spherical methane-methane interaction potential energy function. The potential has a zero crossing point, σ, of 3.62 Å, a well depth, ϵ, of 200 K, and an intermolecular separation at the minimum, r_m, of 4.02 Å.

*Published in modified form as:

Methane-Methane Isotropic Interaction Potential from
Total Differential Cross Sections

Brian P. Reid, Michael J. O'Loughlin, and Randal K. Sparks

The Journal of Chemical Physics **83**, 5656, (1985).

2.1 Introduction

The methane-methane van der Waals interaction, while being of interest for the determination of methane properties, can also serve as a prototype for modeling of more complex molecules. Such "nonbonding" interactions are essential components in the "force-field" approach to the determination of molecular structure.[1] In the structural determination of proteins and other biological molecules where structures are critical to the function of the molecules, the complexity of the problem precludes the use of *ab initio* methods.[2] If an accurate methane-methane potential energy function were available, it could be used within the force-field method to simplify the conformational analysis of these large organic molecules. The interest in an accurate characterization of the methane-methane interaction has led to many attempts to develop a suitable intermolecular potential for this system.[3] However, the results of these attempts, often based on only one physical property measured over a small range of interaction energies, are inconsistent.

As part of our work on the intermolecular potentials of methane-containing systems, we have performed crossed molecular beams total differential cross section studies on the methane-methane system. The determination of a complete, accurate anisotropic potential based on a fit to methane-methane total differential cross sections (DCS) is not practical using methods currently available. Therefore we have modeled the methane interactions as isotropic. The pseudo-spherical nature of methane suggests that this approximation could be reasonable and, in fact, it has often been used in order to determine isotropic methane-methane potentials from bulk data. The well developed methodology of determining isotropic potentials using scattering and bulk data indicates that

the application of such procedures to the methane-methane system would be relatively easy and produce a useful methane-methane potential.

In order to determine such an isotropic methane-methane potential we have followed the same general procedure given in our work on the neon-methane and argon-methane systems.[4] We have determined the parameters of an isotropic potential form by fitting the properties calculated from the potential to experimental data. The data used include our DCS's measured at three collision energies and literature for viscosity and virial coefficients which span broad temperature ranges. In this paper we present our experiment and results for the methane-methane system. Included are a comparison of our potential with previously determined potentials and a discussion of the validity and nature of modeling methane interactions as isotropic.

2.2 Experimental Procedure

The experiment is similar to that previously described by O'Loughlin *et al.*[4] We briefly summarize it here and detail only those aspects particular to the methane-methane system. In the molecular beams apparatus two methane beams were crossed at 90°, and the scattered methane was detected using a quadrupole mass spectrometer which rotates in the plane defined by the two beams. The beams were produced by the expansion of methane gas (Matheson purity, 99.99% min., used without further purification) through .075 mm nozzles, and the collision energy was selected by controlling the temperature of the gas in the stagnation region of the beam source. Velocity distributions, $P(v)$, of

the beam sources were measured using time-of-flight techniques and fit to the functional form shown in Formula 2.1.

$$P(v) \propto v^2 e^{s^2(v-v_0)^2/v_0^2} \tag{2.1}$$

The parameter s is the speed ratio of the beam and v_0 is the flow velocity of the beam. For the three collision energies studied, beam source temperatures, stagnation pressures, velocities and speed ratios[4] are given in Table 2.1. Detector aperture dimensions and beam dimensions are the same as those given in Reference (4). Intensity distributions of the scattered methane were obtained by scanning from 2.5° to 45° measured with respect to the primary beam (the narrower of the two beams). The secondary beam was modulated with a 150 Hz tuning fork chopper to account for the background from the primary beam. In addition, modulated background from the secondary beam was accounted for by performing the data counting cycle with the primary beam alternately blocked and unblocked. The measured distributions and experimental uncertainties are given in Appendix A for scattering at three collision energies of 1180, 745 and 448K k_B, where K stands for Kelvin and k_B is the Boltzmann constant.

2.3 Analysis and Results

The analysis of the data has also been described in detail by O'Loughlin *et al.*[4] To determine an effective spherical potential for methane we chose an analytical potential form and varied its parameters so that the properties calculated from that potential fit the experimental data. The potential we used

Table 2.1

Beam source characteristics for methane-methane at the three collision energies.

Beam Source Characteristic (Primary/Secondary)	Collision Energy/k_B (K)		
	1180	745	448
Stagnation pressure(torr)	800/1175	920/920	320/400
Stagnation temperature(K)	303/303	193/202	118/118
Velocity(10^4 cm/sec)	11.25/10.91	8.71/8.91	6.79/6.84
Speed ratio	7.6/8.2	9.9/9.9	9.4/9.8

for these calculations was a Morse-Morse-spline-van der Waals (MMSV) form, which is given by Equation 2.2.

$$f(x) = \begin{cases} \omega^{-1} e^{\beta_1 - x\beta_2\omega}[e^{\beta_1 - x\beta_2\omega} - 2] & \text{for } x < 1 - \beta_2^{-1}\ln 2 \\ e^{\beta_2(1-x)}[e^{\beta_2(1-x)} - 2] & \text{for } 1 - \beta_2^{-1}\ln 2 \le x \le x_1 \\ b_1 + (x - x_1)\times & \\ \{b_2 + (x - x_2)[b_3 + (x - x_1)b_4]\} & \text{for } x_1 < x < x_2 \\ -c_6 x^{-6} - c_8 x^{-8} & \text{for } x_2 \le x \end{cases} \tag{2.2}$$

The potential is written in reduced form ($x = r/r_m$, $f(x) = U(x)/\epsilon$, where r_m is the intermolecular separation and ϵ the depth at the potential minimum). In the equation, $\omega = (\beta_1 - \ln 2)/(\beta_2 - \ln 2)$, and $c_i = C_i/\epsilon r_m^i$ where the C_i are the long range van der Waals dispersion coefficients. The spline coefficients, b_i, are determined by the constraints that the potential and its first derivative be continuous at x_1 and x_2.

With this potential, center of mass DCS's were calculated using standard formulae for elastic scattering.[5] In calculating the scattered wavefunctions, approximately 400 partial waves were used. The phase shifts were calculated using the JWKB approximation, and averaging was done over the instrument parameters to determine laboratory scattering intensities. Since collisions are between identical particles, the symmetry of the scattered wavefunctions, as well as the scattering from both beams, must be accounted for. Methane has three possible total nuclear spins with values 0, 1, or 2. The population of the total nuclear spin states in the methane beams was assumed to be that for normal methane: $\frac{2}{16}$ spin 0, $\frac{9}{16}$ spin 1, and $\frac{5}{16}$ spin 2.[6] Since the total nuclear spin of a methane molecule is always integral, each molecule was treated as a boson. For collisions between molecules with the same total nuclear spins (43 % of the collisions), the standard weighting of symmetric and antisymmetric spatial wavefunctions was employed (approximately two thirds even partial waves and

one third odd).[5b] For collisions between molecules in different total spin states symmetry requirements on the scattered wavefunctions are not necessary. In Figure 2.1 we show a section of the 745K k_B scattering date which illustrates the effect of identical particle scattering. Small symmetry oscillations are apparent in the data, and they appear in the proper scattering calculation but not when identical particle considerations are neglected.

Second virial coefficients, $B(T)$, were calculated from the intermolecular potential using the classical formula plus the first order quantum correction which are summarized in Equation 2.3.[7]

$$B(T) = 2\pi N_A \int_0^\infty \{1 - e^{-U(x)/kT} + \frac{h^2}{48M\pi^2k^3T^3} e^{-U(x)/kT}[U'(x)]^2\} r^2\, dr \quad (2.3)$$

N_A is Avagadro's number, M is the mass of methane, T is the absolute temperature, and x, as before, is r/r_m. Numerical evaluations were performed as described by O'Loughlin *et al.*[4] Experimental values for $B(T)$ for methane were obtained from Dymond and Smith.[7]

The equations and the numerical procedures employed to calculate the viscosity coefficients of methane are detailed in Appendix B, which also contains the computer code used. Briefly, viscosities were calculated to second order using the first order Chapman-Enskog term and the second order Kihara approximation.[8] The generalized cross sections and collision integrals were computed using JWKB phase shifts calculated at 30 energies between 13 and 30,000K k_B except that below 60K k_B exact quantum phase shifts were used. Identical particle effects are negligible for this system in the temperature range for which experimental data are available and were not included in the calculations.

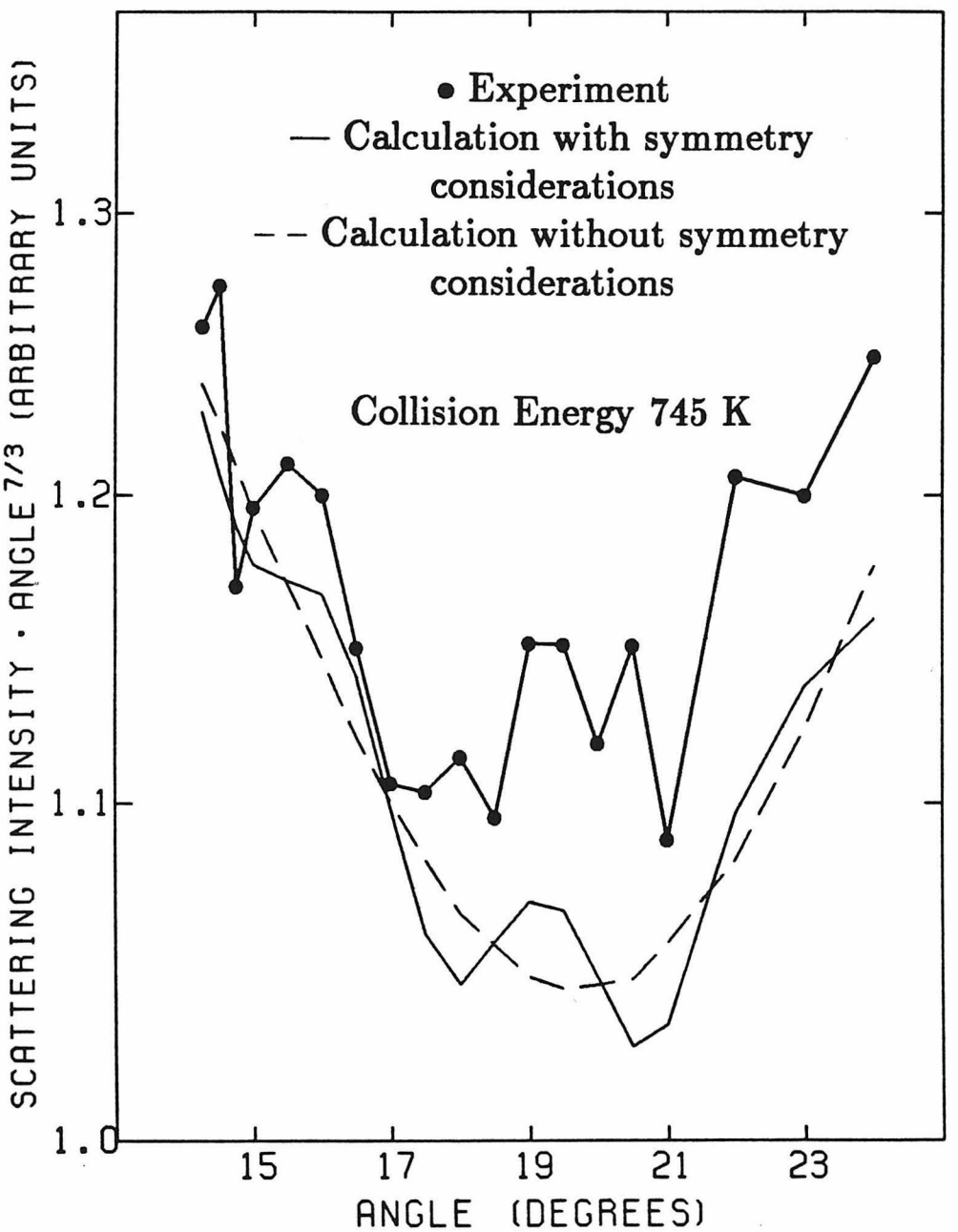

Figure 2.1 Identical paritcle effects in methane-methane scattering are apparent in the data and calculations. A calculation including proper wave function symmetries (solid line) shows oscillations also visible in the data. These do not occur in the same calculation ignoring symmetries (dashed line). The curves are calculated from Potential D.

The calculated viscosities were compared with 18 values given in a critical compilation by Maitland and Smith[9].

The potential parameters were adjusted to give the lowest dimensionless root mean square (rms) deviation from the experimental data.[10] This was done simultaneously for the scattering, viscosity and virial data. All potential parameters were adjusted with the following qualifications. The spline parameters, x_1 and x_2, were restricted so that the potential had no oscillations in the spline region. The van der Waals coefficient C_6, chosen as that given by Thomas and Meath,[11] was kept fixed to ensure the correct theoretical asymptotic form of the potential. Since theoretical estimates for C_8 and C_{10} vary widely we did not include C_{10} in the potential and adjusted the C_8 coefficient (but did not allow it to become negative) in order to determine an effective C_8.

The MMSV potential parameters resulting from such minimized rms deviation fits to several combinations of the different sets of experimental data are presented in Table 2.2. The parameters of Potential A correspond to a fit to all three sets of scattering data and both bulk properties, Potential B to the two highest energy sets of scattering data and both bulk properties, and Potentials C, D, and E to the 1180, 745, and 448K k_B scattering data individually along with the bulk properties. Potential F was determined just from the scattering data at all three collision energies (no bulk properties were used). Potentials G, H, and I were determined only from the scattering data at 1180, 745, and 448K k_B respectivley. Potential B is shown in Figure 2.2 with estimated limits of uncertainty. The upper and lower bounds shown were chosen so that Potentials A through E in Table 2.3 would lie within these limits. The scattering and bulk properties predicted by Potential B are shown in Figures 2.3 and 2.4.

Table 2.2

MMSV parameters for methane-methane potentials determined from fits to the data indicated. Viscosity data are indicated by η.

Potential	ϵ (K)	r_m (Å)	β_1	β_2	x_1	x_2	C_6 (K nm^6)	C_8 (K nm^8)
Potential A (1180,745,448 K,η, $B(T)$)	201	4.03	15.7	6.64	1.07	1.74	0.898	0
Potential B (1180,745 K, η, $B(T)$)	199	4.02	7.50	7.22	1.09	1.49	0.898	.141
Potential C (1180 K, η, $B(T)$)	202	4.01	8.80	7.06	1.09	1.52	0.898	.101
Potential D (745 K, η, $B(T)$)	195	4.03	7.60	7.17	1.09	1.48	0.898	.161
Potential E (448 K, η, $B(T)$)	195	4.13	5.54	6.60	1.07	1.67	0.898	0
Potential F (1180,745,448 K)	195	4.36	6.55	6.98	1.06	1.79	0.898	0
Potential G (1180 K)	197	4.10	5.35	7.34	1.09	1.55	0.898	.131
Potential H (745 K)	182	4.12	6.30	7.46	1.09	1.52	0.898	.141
Potential I (448 K)	191	4.25	5.61	6.24	1.07	1.72	0.898	0

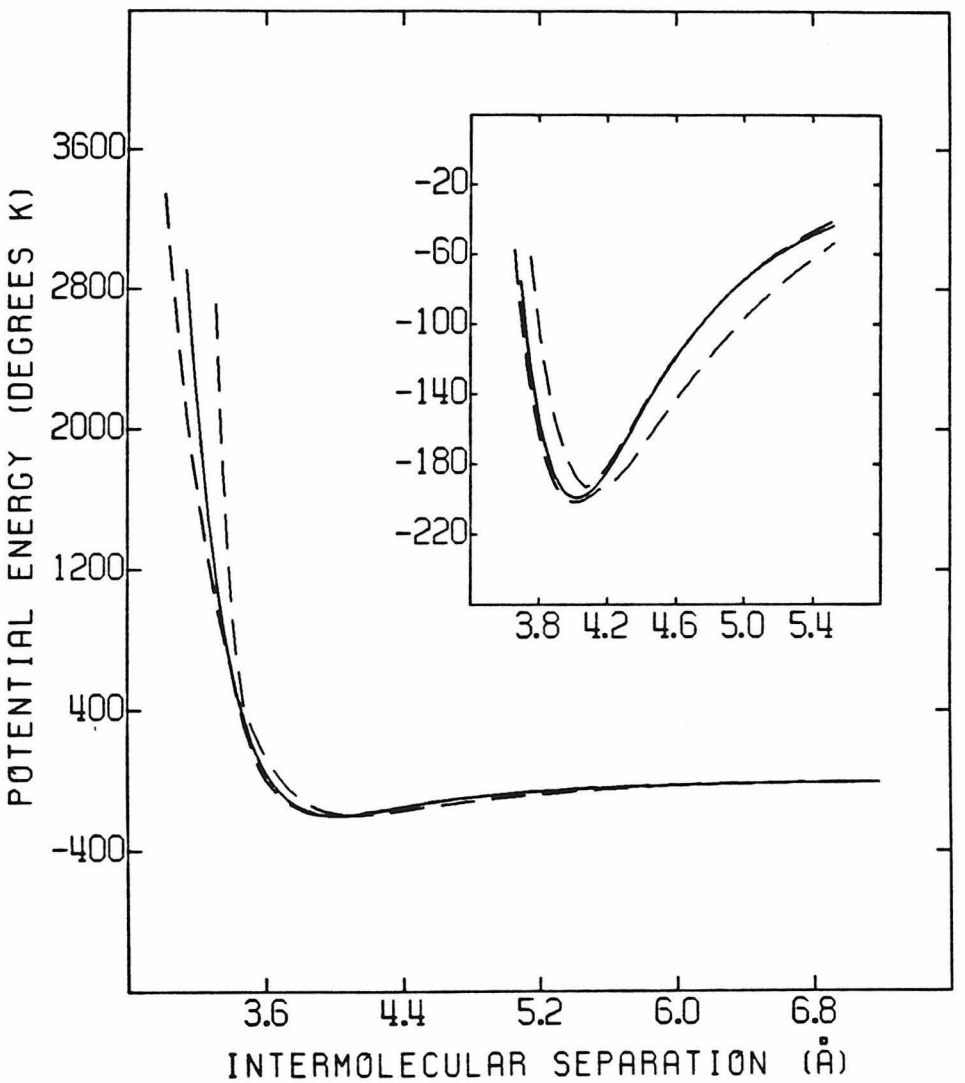

Figure 2.2 Methane-methane potential B (solid line) with limits of uncertainty (dashed lines). A detail of the wall region is shown in the inset.

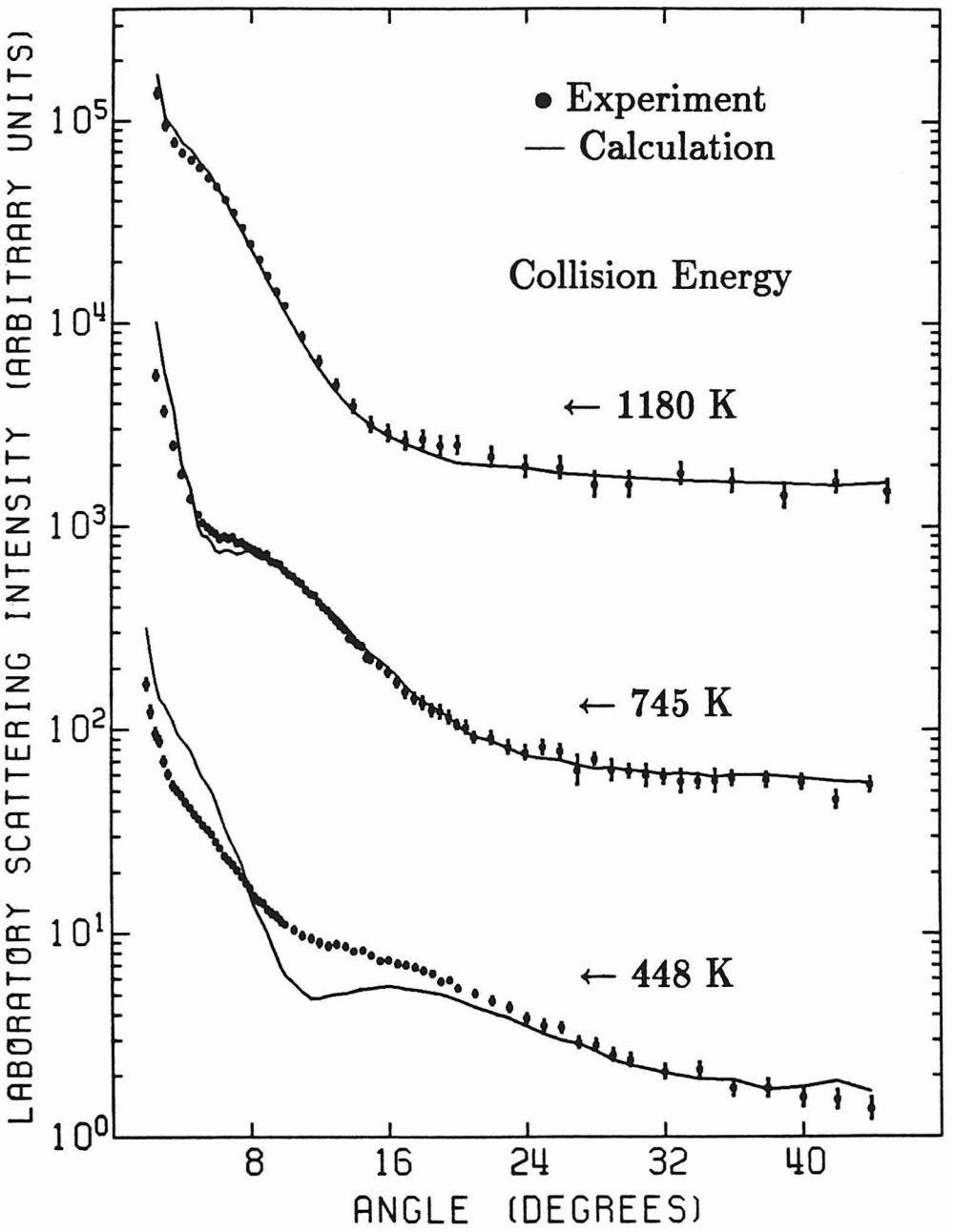

Figure 2.3 Laboratory scattering intensities are plotted as a function of laboratory angle, with the data for the different collision energies offset and the uncertainties shown by the error bars. The solid line is calculated from potential B whose parameters are given in Table 2.2.

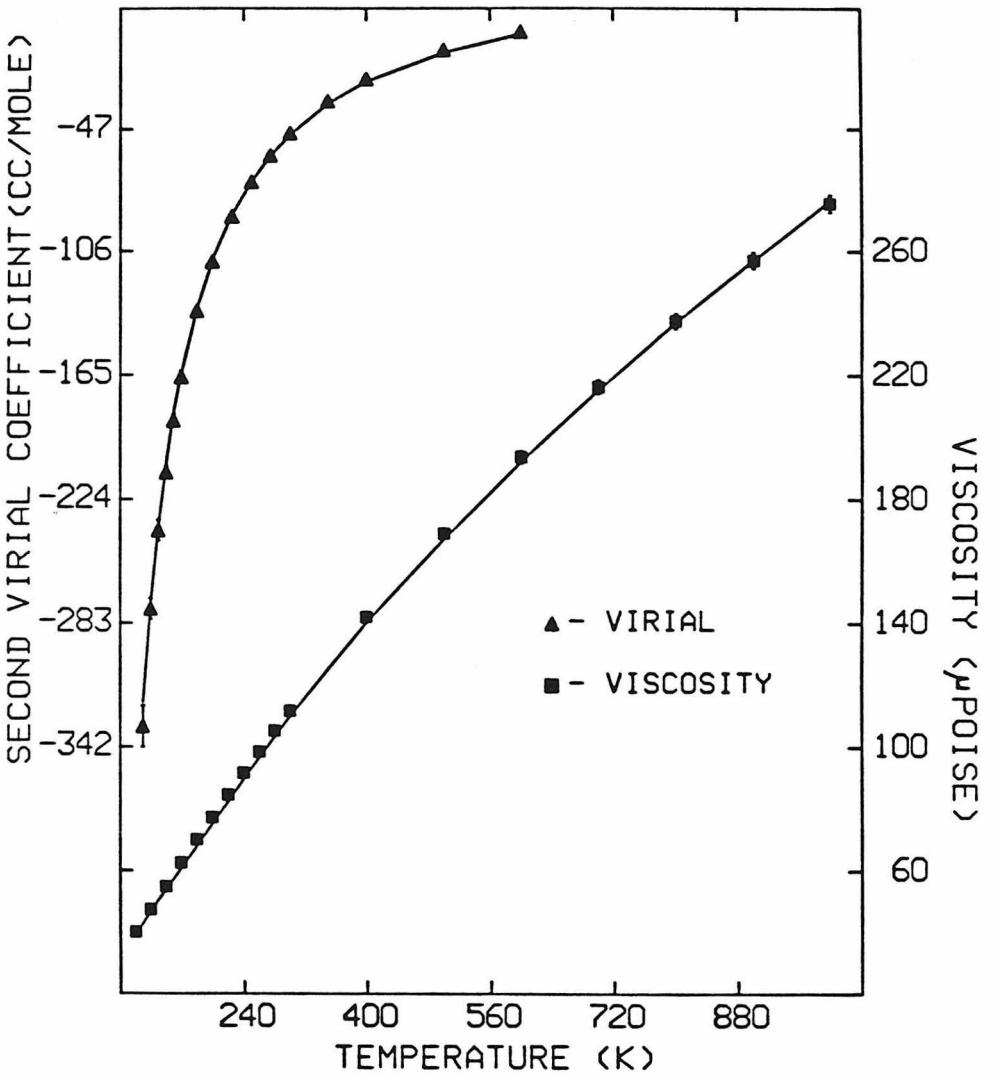

Figure 2.4 Second virial coefficient data (triangles) from Ref. 7 and viscosity data (squares) from Ref. 11 are displayed along with the solid lines calculated from potential B. Experimental uncertainties are shown where they are larger than the data markers.

2.4 Discussion

Using the spherical approximation we have determined intermolecular potential energy functions which fit our new scattering data and the literature bulk property data. Although these potentials are spherical they are not necessarily identical to the solid angle spherical average of the true anisotropic potential. Rather, our potentials are effective spherical potentials. Relating effective isotropic potentials to the true anisotropic potential is not a well resolved problem. Several types of isotropic potentials based on anisotropic potentials have been suggested. These include the spherical average or mean, the spherical median,[12] and the spherical limit.[13] When the anisotropy of the system is large, spherical averages have been shown not to accurately reproduce the properties of the anisotropic potential. The median potential, which is the median of the anisotropic potential at fixed internuclear distance, has been shown, for a diatom-diatom system, to be close to the effective spherical potential that results from the inversion of bulk, thermophysical data, even when the anisotropy of the system is large.[14] The spherical limit is defined for an anisotropic potential which has the same form but different parameters at different angular orientations. When only the first term in the angular expansion of the parameters is used in the potential form, the spherical limit results. It has been shown in some cases that scattering and bulk properties are predicted well by the spherical limit.[13] In this section we consider these types of spherical potentials in relation to our effective potentials. Specifically, we discuss possible effects of the true anisotropic nature of the potential on our data and our effective isotropic potential, compare our work to previously determined potentials, both isotropic and anisotropic, and

present a comparison of the isotropic modeling of methane to the truly isotropic interactions of krypton with other atomic species.

2.4.1 Anisotropic Effects

The deviations of our spherically produced fits from the experimental data give an indication of the anisotropy present in the methane-methane interaction. The fits illustrate that the lowest energy scattering data (448K k_B) are the most difficult to reproduce using our spherical potential form. Attempts to force the potential to fit the 448K k_B scattering data, using either the individual 448K k_B data set or all three sets of scattering data together, degrade the fits to the bulk data and to the higher energy scattering data. When the C_6 van der Waals coefficient is adjusted in the fitting procedure, it becomes unrealistically small for the individual fit to the low energy scattering data (approximately one half the theoretical estimate), but it stays very close to the theoretical estimate for the individual fits to both the higher energies. Part of the problem in fitting the low temperature data could be due to potential form not being flexibile enough to model the anisotropic data. However, the effect of the anisotropy upon the scattering would be expected to become most noticable at the lowest collision energy, and the deviation from a spherical calculation should be most prominent there. Anisotropies in intermolecular interactions have been shown to damp the rainbow oscillations in the scattering, compared to the scattering from the spherical limit of the potential.[13] This effect is apparent when our data and spherical fits are compared, especially in the damping of the rainbow oscillations of the 448K k_B scattering shown in Figure 2.3. Also, although it is possible to fit any individual set of scattering data fairly well, it is very difficult to fit all the sets with the same potential. These observations indicate that the scattering

data, especially the low energy data, contain some important information about the anisotropy of the system.

Although the bulk data are more easily fit with a spherical potential than the scattering data, this does not necessarily mean that the anisotropy has less effect on the bulk properties. In work concerning direct inversion of bulk data for anisotropic systems to yield an effective isotropic potential, it has been found that the isotropic potentials have deeper wells at shorter separation than the spherical average of the anisotropic potential.[15] This effect grows as the anisotropy of the system increases. In order to see the effect of the bulk data on our potentials we performed the fitting procedure without the bulk data. As seen in Table 2.2 this results in slightly shallower wells and larger separations at the minimum. This may indicate that effective spherical potentials based solely on total DCS data maybe somewhere between the spherical average of the potential and an effective potential determined from inversion of bulk data.

In order to minimize the effect of the anisotropy, while still including the sensitive information contained in the scattering data, we determined Potential B using only the 745 and 1180K k_B scattering data along with the two sets of bulk property data. The anisotropy should be less significant at these two higher energies, and spherical potentials are able to reproduce the scattering data at these energies more accurately than at the low energy. Since Potential B also gives very good fits to the bulk properties, it gives the best overall fit to those data which are most easily fit by a spherical potential.

2.4.2 Comparison with Previous Potentials

While investigating previously determined methane-methane potentials, we have looked both at how they compare to our potentials and how well they

predict the scattering and bulk data relative to our potentials. In comparing our scattering data with calculations from the various potentials we rely not only on the numerical deviation but also on the reproduction of the rainbow maxima. In Figure 2.3 one can see the rainbow structure, which is typical in scattering from potentials with both attractive and repulsive regions, at 6, 9, and 16° for the three different collision energies. For a given potential energy form, the position of the rainbow in center-of-mass coordinates is directly dependent upon the ratio of the well depth of the potential to the collision energy. This is apparent in the laboratory data: as the collision energy decreases, the rainbow angle increases. In the lowest energy data one can see a small additional feature around 6° which is a supernumerary rainbow. Our Potential A predicts all the rainbows at the proper angles while Potential B reproduces the rainbow oscillations of the two higher energy sets of data quantitatively and gives the correct positions of the low energy rainbow oscillations. Potential B also fits the bulk properties with a fair degree of accuracy.

We have compared several of the many methane-methane potentials in the literature to our data and our potential. The selections include several potential forms determined from both theoretical and empirical work. In Table 2.3 we list three potentials representative of the previous work. These include work by Matthews and Smith (MS-1976),[3a] Righini, Maki and Klein (RMK-1981),[3b] and Böhm, Ahlrichs, Scharf, and Schiffer (BASS-1984).[3c] The table lists our Potentials A and B as well as the Kr-Kr potential[16] (see section IV C). The parameters σ (the point where $U(\sigma/r_m) = 0$), ϵ, and r_m as well as the dimensionless rms deviations of the properties predicted by the potentials

Table 2.3

Dimensionless rms deviations from experimental methane data for various potentials. Viscosity data is indicated by η. Kr-Kr potential is from Reference (16).

Potential (type)	Basis	Parameters			RMS Deviations					
		σ (Å)	ϵ/k_B (K)	R_m (Å)	1180 K Data	778 K Data	448 K Data	Virial Data	Viscosity Data	Total (Total less 448 K data)
Potential A (MMSV)	DCS, $\eta, B(T)$	3.61	201	4.03	3.7	6.3	8.7	2.6	2.3	5.3(4.1)
Potential B (MMSV)	DCS, $\eta, B(T)$	3.63	199	4.02	2.3	3.2	15.3	1.0	1.1	7.1(2.1)
MS-1976 (L-J 20-6)	$\eta, B(T)$	3.56	217	3.88	2.8	7.2	14.7	1.0	0.6	7.4(3.9)
RMK-1981 (Spherical Average)	$B(T)$, solid state	3.69	174	4.14	7.2	4.8	13.9	3.2	1.2	7.5(4.7)
BASS-1984 (Spherical Average)	*ab initio*, $B(T)$	3.92	80	4.38	16.7	21.0	20.1	47.8	9.9	26.5(27.9)
BMW-1985 (Barker)	DCS, $B(T)$	3.64	205	3.96	3.4	2.7	14.3	2.2	1.6	6.8(2.6)
Kr-Kr (HFGRK)	krypton data	3.59	200	4.01	2.5	5.7	14.0	4.3	2.4	7.2(4.0)

from the actual experimental data are also given. These potential functions are displayed in Figure 2.5.

To summarize the comparisons for effective isotropic potentials based on viscosity or virial data, we find that in general the potentials with well depths shallower (deeper) than ours predict rainbow structure at angles smaller (greater) than in the actual experiment. While the position and depth of the minimum vary widely among these previous isotropic potentials, the values of σ seem quite similar to ours. The representative potential in this category is the numerical potential of Matthews and Smith which was determined by inversion of viscosity and virial data. For our calculations we have only used the Lennard-Jones 20:6 form which they fit to their numerical potential. Since the 20:6 form did not reproduce the shape of the numerical well it may not be an adequate substitute for the numerical potential, but it is similar and more convenient. The large well depth of this potential produces the scattering rainbows at angles slightly larger than the experimental data. Although its minimum is 0.15 Å smaller than ours (Potentials A and B), its value for σ is only about 0.06 Å smaller. Again we point out that the fits to the scattering data alone, without the bulk data, give smaller ϵ's and larger separations at the minimum, and this seems to indicate that the inversion potential and the potential that best fits the scattering data are not the same.

We have spherically averaged the anisotropic potentials, RMK-1981 and BASS-1984, and it is the results for these average potentials which are given in Table 2.3. The anisotropic potentials have been determined in the form of atom-atom exponential repulsions and electrostatic interactions with added dispersion energies. We have averaged them analytically following the method

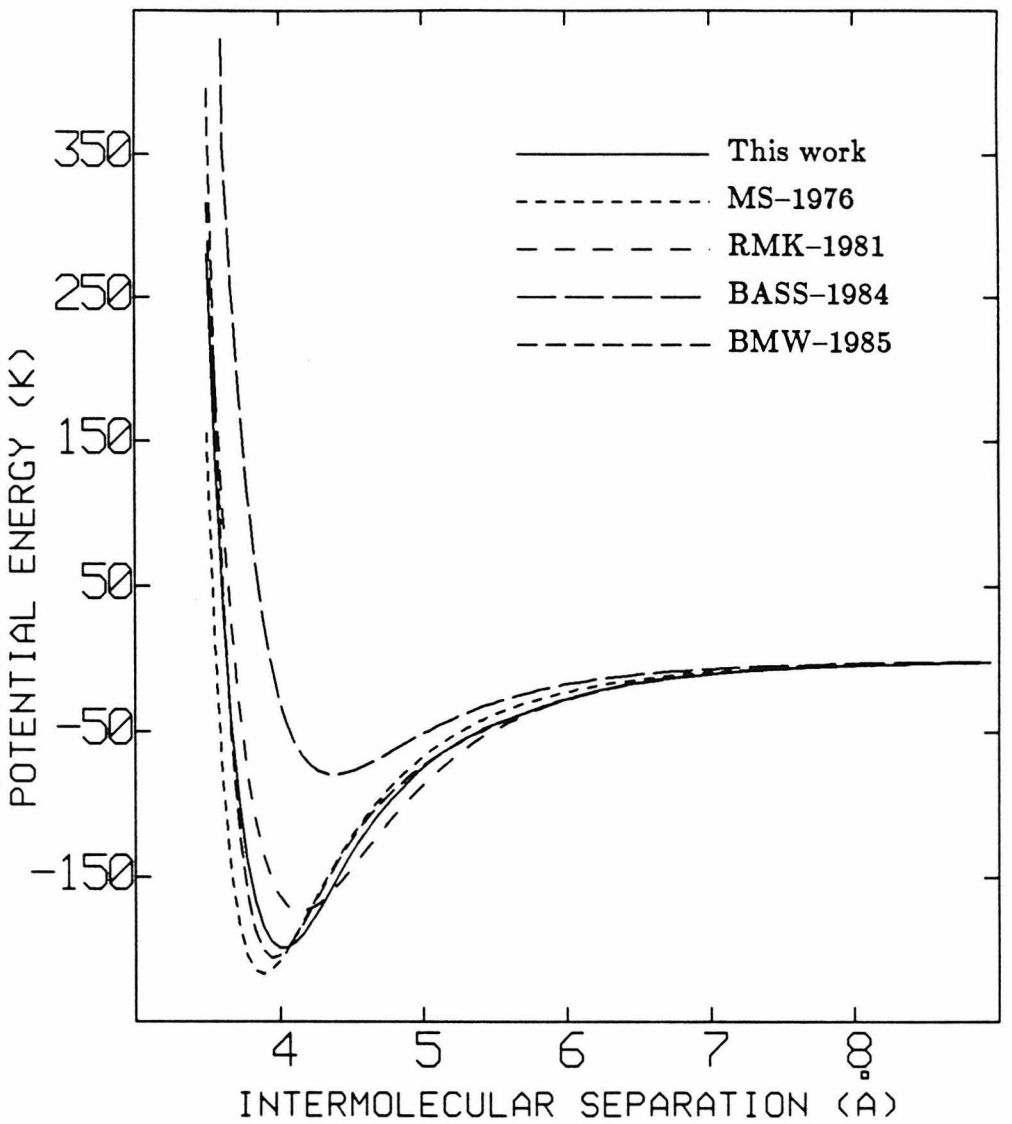

Figure 2.5 Our Potential B is displayed along with the MS-1976 potential, the spherical averages of the RMK-1981 and BASS-1984 potentials, and the BMW-1985 potential.

implied by Meinander and Tabisz.[17] When spherically averaged, the electrostatic interactions cancel and the resulting isotropic potential involves only the atom-atom repulsions and the dispersion energies. When averaging the BASS-1984 potential we did not damp the dispersion energies for the carbon-hydrogen and hydrogen-hydgrogen interactions in the same anisotropic manner as was indicated in the original paper. Instead we averaged the dispersion energies undamped and then included an isotropic damping factor. The error that this approximation could introduce was found to be less than 8K k_B in the well depth and 0.05 Å in the minimum. The RMK-1981 potential is based on virial coefficients and solid state data and the authors suggest that it is perhaps the result of the true anisotropic potential averaged, in some sense, over the ground state librational wavefunction of the solid. Indeed the RMK-1981 spherical average is closer to our effective spherical potentials and the complete RMK-1981 potential is less anisotropic than the BASS-1984 potential which is based on *ab initio* calculations and virial data. As can be seen in Table 2.3, the RMK-1981 average predicts reasonable experimental properites while the BASS-1984 is clearly not useful in a spherically averaged form. This indicates that the spherical average of the true anisotropic potential may indeed be significantly different than our effective spherical potentials in the manner found for the bulk data inversion potentials,[15] the former having shallower wells at greater intermolecular separation.

2.4.3 Comparison with Other Crossed Beams Data

Since the completion of this work, other total differential cross section data has been reported by Boughton, *et al.*[18] They report room temperature beam data, and their measured intensities are the same as our highest energy data to within a few percent at angles from 2.5° to about 12°. At larger angles their data

are higher than ours. This is accounted for by the fact that their cross sections were measured using a bolometric detector which is sensitive to the energy of the particles being detected. Since the laboratory velocity of the scattered methane increases with increasing angle, a larger bolometric signal is expected.

The parameters of their reported isotropic potential, BMW-1985, are given in Table 2.3, and the potential is displayed in Figure 2.5. Their potential is extremely similar to ours and reproduces our data well. One small difference is that the repulsive wall of the BMW potential is slightly steeper than ours. This is reflected in the large angle scattering, where their potential predicts cross sections slightly too high. Boughton, *et al.* discuss this discrepancy but were unable to resolve it. The influencing of the methane internal energy upon the bolometer is uknown and introduces some uncertainty in their large angle scattering. Our measured and calculated cross sections do not suffer from these problems. Overall, however, the very good agreement between the data from the two instruments and the similarity of the determined potentials lend support to the results.

2.4.4 Comparison of Methane with Krypton

It was pointed out by Righini *et al.* that the spherical average of the RMK-1981 potential was quite close to the krypton-krypton interaction potential.[16] We have noticed that our effective isotropic methane-methane potentials are also extremely similar to the Kr-Kr potential, and in Table 2.3 we have included the deviations of the methane-methane properties predicted by the Kr-Kr potential. The relatively small deviations are astounding in light of the fact that the Kr-Kr potential was not fit to any data relating to methane. Since we[4] and others[19,20] have determined several isotropic methane-atom interactions it is interesting to

compare the resulting potentials with those for the same systems with methane replaced by krypton.[16,21,22] The comparison is summarized in Table 2.4. The comparison is quite good for the methane-, argon- and neon-methane systems but is less so for helium and hydrogen. The deviations are somewhat systematic with the methane seeming effectively larger and slightly less attractive to the smaller interaction partners. The similarity between krypton and methane is most likely related to their similar polarizabilities, 2.60Å^3 for methane[8a] and 2.47Å^3 for krypton.[23] The correlation between the potential parameters for van der Waals interactions and the polarizabilities of the interacting particles has been examined and appears to be general.[24]

2.5 Conclusions

We have performed cross molecular beam studies at three collision energies on the methane-methane van der Waals system. These sets of scattering data provide detailed information about the methane-methane interaction. Using the new data and previously reported viscosity and second virial coefficient data we have determined effective, spherical methane-methane potential energy functions which can adequately reproduce the scattering data and accurately reproduce the bulk property data. Such effective isotropic potentials for this system appear to be somewhat different from the spherical average of the true anisotropic potential. Effects of the anisotropy in the potential are visible in the fits to the scattering data, and this indicates that our scattering data could be used to determine an accurate anisotropic potential surface when the methodology to perform the necessary calcluations becomes available.

Table 2.4
Potential parameters for methane and krypton systems.

	ϵ (K k_B)	R_m (Å)
CH_4-CH_4[a]/ Kr-Kr[b]	199/200	4.02/4.01
CH_4-Ar[c]/ Kr-Ar[d]	170/168	3.85/3.88
CH_4-Ne[c]/ Kr-Ne[e]	66/70	3.68/3.70
CH_4-He[f]/ Kr-He[d]	23/30	3.85/3.67
CH_4-H[g]/ Kr-H[d]	58/68	3.69/3.57

(a) This work.
(b) From reference (16).
(c) From reference (4).
(d) From reference (21).
(e) From reference (22).
(f) From reference (19).
(g) From reference (20).

2.6 References

[1] N.L. Allinger, Adv. Phys. Org. Chem. **13**, 1 (1976).

[2] H.A. Scheraga, Adv. Phys. Org. Chem. **6**, 103 (1968).

[3] See (a) G.P. Matthews, E.B. Smith, Mol. Phys. **32**, 1719 (1976);
(b) R. Righini, K. Maki, M. Klein, Chem. Phys. Lett. **80**, 301 (1981);
(c) H.J. Böhm, R. Ahlrichs, P. Scharf, H. Schiffer, J. Chem. Phys. **81**, 1389 (1984);and references therein.

[4] M.J. O'Loughlin, B.P. Reid, and R.K. Sparks, J. Chem. Phys. **83**, 5647 (1985).

[5] See, for example,(a) M.S. Child, *Molecular Collision Theory* (Academic Press, New York, 1974); (b) H. Pauly, in *Atom - Molecule Collision Theory: A Guide for the Experimentalist*, edited by R.B. Bernstein (Plenum Press, New York, 1979), Chapter 4.

[6] G. Herzberg, *Molecular Spectra and Molecular Structure Vol. II* (Van Nostrand Reinhold, New York, 1945).

[7] J.H. Dymond and E.B. Smith, *The Virial Coefficients of Pure Gases and Mixtures* (Oxford University Press, Oxford, England, 1980).

[8] (a) J.O. Hirschfelder, C.F. Curtis, and R.B. Bird, *Molecular Theory of Gases and Liquids* (John Wiley and Sons, New York, 1954);
(b) S. Chapman and T.G. Cowling, *The Mathematical Theory of Non-Uniform Gases* (Cambridge University Press, New York, 1952).

[9] G.C. Maitland and E.B. Smith, J. Chem. Eng. Data **17**, 150 (1972).

[10] R.T Pack, J.J. Valentini, C.H. Becker, R.J. Buss, and Y.T. Lee, J. Chem. Phys. **77**, 5475 (1982).

[11] G.F. Thomas and W.J. Meath, Mol. Phys. **34**, 113 (1977).

[12] J.L. Lebowitz and J.K. Percus, J. Chem. Phys. **79**, 443 (1983).

[13] R.T Pack, J.J. Valentini, and J.B. Cross, J. Chem. Phys. **77**, 5486 (1982).

[14] C.G. Gray and C.G. Joslin, Chem. Phys. Lett. **101**, 248 (1983).

[15] E.B. Smith and A.R. Tindell, Faraday Disc. Chem. Soc. **73**, 221 (1982).

[16] R.A. Aziz, Mol. Phys. **38**, 177 (1979).

[17] N. Meinander and G.C. Tabisz, J. Chem. Phys. **79**, 416 (1983).

[18] C.V. Boughton, R.E. Miller and R.O. Watts, Mol. Phys. **56**, 363 (1985).

[19] J.T. Slankas, M. Keil, and A. Kuppermann, J. Chem. Phys. **70**, 1482 (1979).

[20] G.O. Este, G. Knight, and G. Scoles, Chem. Phys. **35**, 421 (1978).

[21] G. Scoles, Ann. Rev. Phys. Chem. **31**, 81 (1980).

[22] R. Candori, F. Pirani and F. Vecchiocattivi, Mol. Phys. **49**, 551 (1983).

[23] R.R. Teachout and R.T Pack, At. Data **3**, 195 (1971).

[24] G. Luiti and F. Pirani, Chem. Phys. Lett. **122**, 245 (1985).

Chapter 3

An Anisotropic Interaction Potential for Neon-Chlorine

3.1 Introduction

The intermolecular transfer and intramolecular redistribution of energy are fundamental to chemical phenomena. van der Waals molecules composed of an atom and a diatom provide simple systems for studying these processes. For closed shell, ground electronic state atoms and molecules, a single potential energy surface formed within the Born-Oppenheimer approximation will serve to summarize the forces involved in such systems at low energies. The nature of this potential energy surface determines the dynamics of dissociation of the weak van der Waals bond.[1,2] Spectroscopic studies of rare gas-halogen molecule systems have provided interesting results about such dissociations.[3] In particular, a very long lived (over 10 μs) metastable state of neon-chlorine has been observed with a quantum of vibrational excitation in the Cl-Cl stretch.[4] The amount of energy in that vibrational quantum is several times the energy required to break the van der Waals bond. The determination of accurate potential energy surfaces for such systems will help to quantify the dynamics involved in such processes.

The scattering of atoms with diatomic molecules also strongly depends upon the potential surface. The analysis of crossed molecular beams scattering data, which has proved to be an important tool for quantifying spherical atom-atom van der Waals potentials,[5] has been applied to molecular systems with anisotropic potentials.[6] While the same features seen in atom-atom elastic scattering provide

information about the general size and strength of an atom-diatom interaction, the effects of translation-to-rotation energy transfer in the scattering can be used as a sensitive probe of the anisotropy of the potential.

In order to help determine the anisotropic interaction potential for the neon-chlorine system, we have measured the angular intensity distribution of neon scattered from chlorine at two collision energies as well as time-of-flight spectra of chlorine scattered from neon at a single collision energy. The angular distributions determined by detecting neon are similar to center-of-mass total differential cross sections of the neon-chlorine system. The rainbow scattering observed in these distributions provides information on the well depth and well depth anisotropy of the potential while the barely resolved diffraction oscillations are a measure of the position of the repulsive wall. The time-of-flight spectra measure the energy changes that occur during collision, which are determined by the state-to-state differential cross sections . These are highly sensitive to the anisotropy in the range of the potential.

The infinite order sudden approximation (IOSA),[7] provides a method for the quantitative calculation of differential cross sections. The computational quickness provided by the IOSA allows a potential to be fit by comparison of calculated cross sections with the scattering data. The IOS approximation is expected to be valid when the relative kinetic enery of the system before and after collision is large compared to the rotational energy change and compared to the well depth of the interaction. The small rotational constant of chlorine and the relatively weak attraction between neon and chlorine make the choice of the IOSA reasonable.

O'Loughlin[8] has calculated center-of-mass total differential cross sections for both the neon-chlorine and helium-chlorine systems using the infinite

order sudden approximation and transformed these to the laboratory frame as elastic differential cross sections. Varying parameters of a potential form within constraints imposed by preliminary fits to the time-of-flight data and spectroscopic data,[9] he produced an anisotropic potential for the system. However, in more detailed analyses, it has not proved possible to find a potential which is consistent with the spectroscopic data, the total angular scattering data, and the time-of-flight spectra. The analysis herein produces a potential with features significantly different from the spectroscopic data and from the potential fit to only the total angular distributions.

3.2 Experimental Procedure

The angular intensity distributions of neon (^{20}Ne) were measured at two collision energies, 464 K and 612 K. Throughout the following discussion, energies given in units of K have been divided by the Boltzman constant, k_B. The procedure was essentially that employed in Chapter 2 for the methane-methane angular distributions; the experimental details and the data are available in Reference (8).

For the time-of-flight spectra, we detected chlorine (^{35}Cl–^{35}Cl and ^{35}Cl–^{37}Cl) in order to take advantage of its high pumping speed and high detection efficiency compared to neon. In order to narrow the velocity distribution of the chlorine beam we used a mixture of 10% chlorine seeded in helium. This mixture produced a beam with less than 0.5% chlorine molecule dimers and negligible helium-chlorine van der Waals molecules, as detected by the electron impact ionization mass spectrometer. The beam source defining slits and geometries were modified from those given in References (8) and (10). The beam source conditions and geometry are listed in Table 3.1. Data at seven angles equally

Table 3.1

Beam source characteristics for neon and chlorine at 1467 K collision energy.

	Ne	Cl_2(in He)
stagnation pressure(torr)	1225	1100
stagnation temperature(K)	303	303
velocity(m/sec)	790	971
speed ratio	20.3	16.9
angular width	1.8°	0.5°
angular height	2.8°	0.9°
nozzle diameter (μm)	76	76

spaced between six and thirty degrees from the chlorine beam were taken and are given in Appendix C.

The time-of-flight spectra were obtained using a 255 channel cross correlation wheel rotating at 490.2 Hz.[11] The detected molecules must pass through the slotted wheel and traverse a 30 cm flight path before being ionized and counted in 8-microsecond bins by a custom designed multichannel scaler. Background counting was performed at those angles where time dependent background was observed. For the angles at which no time dependent background was observed, the average of the first several channels was used as the background signal. The data which appear in Appendix C and which are displayed in this chapter are the correlated data with background subtracted.

3.3 Analysis

Since individual state-to-state differential cross sections are not resolvable in the time-of-flight data, we have modeled the experiment by calculating center-of-mass state-to-state differential cross sections from a parametric potential and convoluting these over the experimental conditions to produce a calculated distribution for comparison with the experimental data. A trial-and-error procedure was used to vary the potential parameters in order to achieve a fit to all of the data.

In the analysis, we have included no vibrational effects of the Cl-Cl bond. We have assumed a rigid rotor structure for Cl_2. This approximation is expected to be adequate for the present analysis.[6] Cooling in the expansion of the chlorine beams, although somewhat inefficient for the vibrational degree of freedom, should produce a beam with only a small fraction of vibrationally excited chlorine, approximately 2% for a beam cooled vibrationally to 200 K. Since

a quantum of vibrational energy in the Cl_2 stretch is about 800 K, only at the highest collision energy is excitation of the chlorine vibration energetically possible. Even in this case,the scattering is expected to be dominated by rotational transitions.[6]

3.3.1 Potential Form

The choice of an appropriate potential form to model the neon-chlorine system was based on several factors. Since the chlorine is assumed to be a rigid rotor, the potential need only be a function of two variables, r and γ, as shown in Figure 3.1. Anisotropic potentials which are formed from an isotropic potential whose parameters are allowed to vary as a function of γ have been found to converge more quicky than direct expansions of the potential.[12] A Morse-Morse-van der Waals form was chosen for the isotropic potential. At short and medium range the potential is described by a Morse function:

$$U_M(r) = \epsilon\, e^{\alpha(r_m - r)} \left[e^{\alpha(r_m - r)} - 2 \right], \tag{3.1}$$

in which ϵ is the depth of the well at the minimum r_m. The potential is joined smoothly at the minimum to a second Morse function of the form,

$$U_{M'} = \epsilon\, e^{\beta/r_m(r_m - r)} \left[e^{\beta/r_m(r_m - r)} - 2 \right]. \tag{3.2}$$

At long range the potential has the van der Waals expansion form:

$$U_V(r) = -\frac{C_6}{r^6} - \frac{C_8}{r^8}. \tag{3.3}$$

The complete potential is given by Equation 3.4,

$$U(r) = \begin{cases} U_M & \text{if } r \le r_m \\ U_{M'} & \text{if } r_m < r < r_i \\ U_V + [U_{M'} - U_V]\, e^{-\rho(\frac{r_i - r}{r_m})^2} & \text{if } r_i \le r\ , \end{cases} \tag{3.4}$$

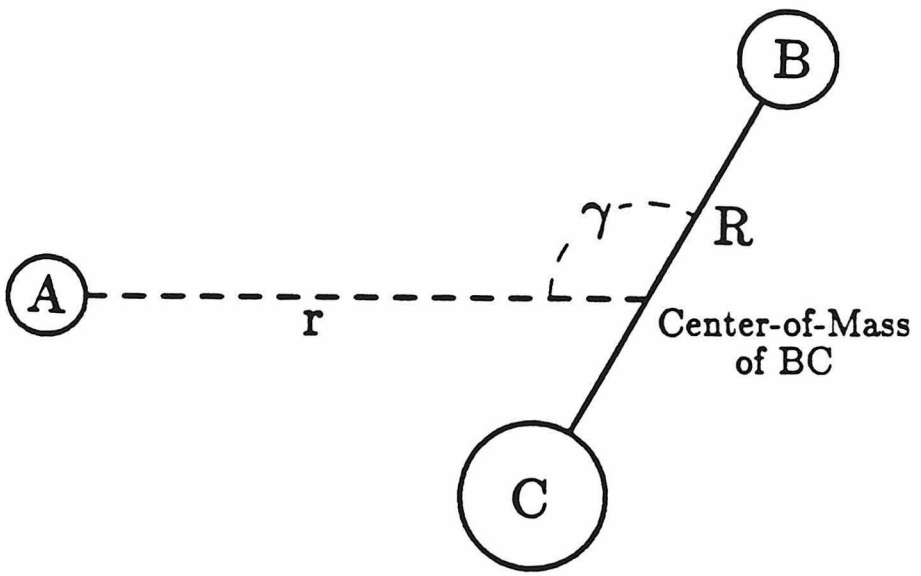

Figure 3.1 The coordinates r, R, and γ are defined for a general atom–diatom interaction. (Figure from Reference 8.)

where $r_i = r_m(1 + \ln 2/\beta)$ is the inflection point of the second Morse function.

The Morse-Morse-van der Waals form was chosen for the isotropic potential because variation of the well depth and position of the minimum is simple with the Morse function, and the correct asymptotic form is assured with the van der Waals expansion. The second Morse function is included to assure that the short range and long range regions are not spuriously affected by each other. To join the Morse region to the van der Waals region a weighted average of the Morse and the van der Waals parts is used at values of r greater than the inflection point of the Morse function. The resulting function behaves very much like the Morse near the inflection point and becomes asymptotically close to the van der Waals function. This method was used instead of a spline function,[13] since the spline functions are prone to unsettling oscillations. The averaging function has a parameter ρ which essentially allows the Morse function to change to the van der Waals expansion quickly or slowly as r increases. This factor was kept at four in order to allow a fairly quick but smooth transition.

To make the potential anisotropic, the parameters are expanded in Legendre polynomials, $P_i(\cos\gamma)$. For example, the well depth, ϵ, is expanded as

$$\epsilon(\gamma) = \epsilon_0 P_0(cos\gamma) + \epsilon_2 P_2(cos\gamma) + \epsilon_4 P_4(cos\gamma) + \cdots \quad . \tag{3.5}$$

The symmetry of the chlorine allows only even functions to be included when the slight shift in the center-of-mass of ^{35}Cl–^{37}Cl is neglected. The parameters, $\epsilon(\gamma)$, $\alpha(\gamma)$, $C_6(\gamma)$ and $C_8(\gamma)$ have been expanded as in Equation 3.5 with truncation at the P_2 term. The expansion of $r_m(\gamma)$ also includes a P_4 coefficient. The second Morse parameter β was not expanded in order to limit the number of variables. It was felt that this would be acceptable since the parameter is essentially a reduced quantity and would not be expected to vary much with angle. The inclusion of

its expansion also would probably not affect the overall results of the calculated scattering or the final potential.

3.3.2 Cross sections from the IOS approximation

We briefly state the equations used in the IOS approximation to calculate rotational state-to-state differential cross sections for an atom-symmetric rigid rotor system. The IOSA involves two approximations, the centrifugal sudden (CS) and the energy sudden (ES) approximations, which treat as constant the angular momentum operators in the Hamiltonian in order to decouple the equations of motion.[7] The energy sudden approximation replaces the rotational angular momentum operator, J^2, of the diatomic rotor by a constant, eigenvalue form, $\bar{j}(\bar{j}+1)\hbar^2$. The centrifugal sudden approximation assumes that the orbital angular momentum operator L^2 can be replaced by an eigenvalue form $\bar{l}(\bar{l}+1)\hbar^2$. The choice of $\bar{l}$ as either the intial, l, or the final, l', orbital angular momentum quantum number of the collision, leads to the simple expressions listed below.[14] However, these choices for the orbital angular momentum predict the phase of odd Δj transitions incorrectly.[15] This deficiency is corrected when $l_{ave} = \frac{1}{2}(l+l')$, the average of the initial and final angular momentum, is used for $\bar{l}$. Approximate differential cross sections derived from the l_{ave} choice reduce to the form given below for even Δj transitions.[15] Since, for Ne-Cl_2, the scattering will be dominated by even Δj transitions, the simple forms should be sufficient.

Equation 3.6 gives the differential cross section at the center-of-mass angle, θ, from rotational state j to j' in terms of a 'matrix element' of the scattering amplitude:

$$\frac{d\sigma}{d\omega}(\theta; j' \leftarrow j, E) = (2j+1)^{-1}\frac{\bar{k}^2}{k_j^2}\sum_{m_j}|\langle j'm_j|f^{\bar{k}}(\theta;\gamma)|jm_j\rangle|^2. \qquad (3.6)$$

In Equation 3.6, the scattering amplitude $f^{\bar{k}}(\theta;\gamma)$, a function of the relative atom-diatom orientation angle, γ, is

$$f^{\bar{k}}(\theta;\gamma) = \frac{i}{2\bar{k}} \sum_{l=0}^{\infty} (2l+1)\{1 - \exp[2i\eta_l^{\bar{k}}(\gamma)]\} P_l(\cos\theta), \tag{3.7}$$

where $\eta_l^{\bar{k}}(\gamma)$ is the lth phase shift calculated from the isotropic potential formed by varying r at constant γ. $\bar{k}$ is defined by

$$\bar{k}^2 = k_{\bar{j}}^2 = \frac{2\mu}{\hbar^2}\left[E - \frac{\hbar^2 \bar{j}(\bar{j}+1)}{2I}\right], \tag{3.8}$$

in which E is the energy of the system and I is the moment of inertia of the diatomic molecule. The IOS approximation also allows the entire matrix of state-to-state cross sections to be calculated from only one column of the matrix. This takes numerical form in Equation 3.9,

$$\frac{d\sigma}{d\omega}(\theta; j' \leftarrow j, E) = \frac{k_0^2}{k_j^2} \sum_{j''} C^2(j, j'', j'|000) \frac{d\sigma}{d\omega}(\theta; j'' \leftarrow 0, E), \tag{3.9}$$

which shows that all differential cross sections can be calculated as a sum over Clebsch-Gordon coefficients times the $j = 0$ to j'' cross sections. When $j = 0$ is placed in Equation 3.6, one integral over γ is left:

$$\frac{d\sigma}{d\omega}(\theta; j'' \leftarrow 0, E) = (2j''+1)\frac{\bar{k}^2}{2k_0^2}\left[\int_{-1}^{1} f^{\bar{k}}(\theta;\gamma) P_{j''}(\cos\gamma)\, d\cos\gamma\right]^2. \tag{3.10}$$

To evaluate Equation 3.10 numerically, Gauss-Legendre quadrature was used. The number of points in the quadrature must be, at the least, larger than j''. Since, at the largest collision energy encountered, j'' could be over 65, 80 point quadrature was used. To evaluate the integrand in Equation 3.10 at the points of the quadrature, the phase shifts were expanded in Legendre

polynomials of $\cos\gamma$ with the expansion coefficients evaluated by 12 point Gauss-Legendre quadrature.[14] The results using 12 points did not differ significantly from the results obtained using 64 points. Phase shifts for 250 partial waves were evaluated using the JWKB approximation and seven point Gauss-Mehler quadrature.[15] In these evaluations the choice of $\bar{j}$ was variable. For initial fitting purposes, the simple and computationally quick choice of $\bar{j}$=0 was used. Since this choice may overestimate very inelastic transitions at large scattering angles, the choice of $\bar{j}$ so that $\bar{k}^2 = \frac{1}{2}\left[k_0^2 + k_{j''}^2\right]$, was used for the final stages of fitting. This choice has been shown to improve the IOS approximation for wide angle scattering.[15] So that different phase shifts would not have to be calculated for every j'', $\bar{j}$ was changed only for every tenth j'' value. These selections of j'' are discussed in Section 3.5.3 below.

3.3.3 Calculation of Laboratory Scattering Distributions

To obtain a laboratory time-of-flight distribution we first form a laboratory velocity distribution from the cross sections calculated in Equation 3.10. This is shown in Equation 3.11:

$$N(V,\Theta_0)\,dV = \int_{\mathbf{r}_c}\int_{\mathbf{V}_2}\int_{\mathbf{V}_1}\sum_j P_j \sum_{j'}\int_\Omega \frac{d\sigma}{d\omega}(\theta; j' \leftarrow j, E) \times J(\frac{\omega}{\Omega}) n_1 n_2 |\mathbf{V}_1 - \mathbf{V}_2| D(V)\,d\Omega\,d\mathbf{V}_1\,d\mathbf{V}_2\,d\mathbf{r}_c \qquad (3.11)$$

The sums include all possible transitions which can produce scattering observable with the detector at Θ_0 and with the laboratory velocities between V and $V + dV$. The eleven integrals (integrals over vectoral quantities imply integrals over the three scaler components of each vector) describe instrument averaging over the collision volume, $\int d\mathbf{r}_c$, the beam source velocities, $\mathbf{V}_1$ and $\mathbf{V}_2$, and the solid angle, Ω, subtended by the detector. The probability that the chlorine is intially

in rotational state j is given by P_j. The number density distribution for each beam at $\mathbf{r}_c$ and velocity $\mathbf{V}_i$ is described by $n_i(\mathbf{r}_c, \mathbf{V}_i)$. $J(\frac{\omega}{\Omega})$ is the Jacobian of the transformation from the center-of-mass coordinate system to the laboratory coordinate system. $D(V)$ is the detector efficiency for the detected species with velocity V. Since the electron impact ionizer is sensitive to number density and since only relative intensities are measured, $D(V)$ is taken as proportional to $1/V$.

The expression for $N(V, \Theta_0)$ is simplified by several approximations. Variations of the integrand in Equation 3.11 with coordinates out of the plane of the beams and the detector were neglected. Beam velocities at different points in the collision volume were assumed to be only in the direction of streamlines radiating from the nozzle and to have the speed distributions measured along the beam axis. The spatial distributions of the beams were assumed to be constant over the collision volume. In a very simple case of the reduction of integration described by Pack,[17] the integrations over the two "in-plane" dimensions of the scattering volume and the integration over the in-plane detector angle, Θ, were replaced by an integration over the relative angle of intersection, ξ, of the two beams and an integration over an effective detector width to account for the absolute orientation of the beams and the detector width.

In the detection of the inelastically scattered products, especially when detecting chlorine, many cases arise in which the Jacobian, $J(\frac{\omega}{\Omega}) = \frac{v^2}{V^2 \cos\delta}$, from the center-of-mass system to the laboratory coordinate system becomes infinite. This occurs when δ, the angle between the laboratory velocity $\mathbf{V}$ and the center-of-mass velocity v of the scattered product, is 90°. To handle this numerically troublesome situation, the domain of the integration over the laboratory angle Θ was transformed to the center-of-mass angle θ. Multiplying the remaining

Jacobian, $J(\frac{\phi}{\Phi}) = \frac{V \sin\Theta}{v \sin\theta \cos(\Phi-\phi)}$,[17] by $d\cos\theta$ produces no singularities in the regions of interest.

The preceeding approximations, simplifications and transformation, change Equation 3.11 to Equation 3.12:

$$N(V,\Theta_0)\,dV = c \int_\xi \int_{V_2} \int_{V_1} \sum_j P_j \sum_{j'} \int_\theta \frac{d\sigma}{d\omega} P_e(\xi, V, \Theta_0, \theta) \times n_1(V_1) n_2(V_2) \frac{|\mathbf{V}_1 - \mathbf{V}_2|}{v}\, d\theta\, dV_1\, dV_2\, d\xi \qquad (3.12)$$

In this equation, $P_e(\xi, V, \Theta_0, \theta)$, is an effective detector weighting function, and the constant c includes the collision volume $\Delta\mathbf{r}_c$, the approximately constant quantity $\sin\Theta_0\Delta\Phi$, and the detector efficiency $D(V)V$.

In order to determine the signal $S_n(\Theta_0)$ measured in channel n of the multichannel scaler, the $N(V,\Theta_0)$ distribution must be averaged over the the channel width, $\Delta\tau_c$, of the scaler, the length of the ionizer, Δl, the finite width of the slots in the time-of-flight wheel, and the size of the detector aperture. This is described in Equation 3.13:

$$S_n(\Theta_0) = \int_{-\Delta\tau_a/2}^{\Delta\tau_a/2} \int_{-\Delta\tau_s/2}^{\Delta\tau_s/2} \int_{(n-\frac{1}{2})\Delta\tau_c}^{(n+\frac{1}{2})\Delta\tau_c} \int_{f-\Delta l/2}^{f+\Delta l/2} N(V,\Theta_0) \frac{dV}{dt}\, dl\, d\tau_c\, d\tau_s\, d\tau_a \qquad (3.13)$$

The quantity $\Delta\tau_s$ is the time it takes for one channel in the time-of-flight wheel to pass the midpoint of the detector while $\Delta\tau_a$ is the time it takes for the midpoint of a wheel slot to pass across the detector aperture. The flight length to the middle of the ionizer is f, while $V = l/t$ is the laboratory velocity and $t = \tau_c + \tau_s + \tau_a + \tau_0$ is the flight time. τ_0 is an offset determined mainly by the flight time of the ions from the ionizer to the ion detector. The Jacobian, $\frac{dV}{dt}$, is included to transform the integration from velocity to time space.

To evaluate Equation 3.12 numerically, dV was approximated by a finite $\Delta V = 3$ m/s. The integrations over ξ and θ were approximated by Gauss-Legendre quadrature. The quadrature over θ used seven points. The integrations over V_1 and V_2 were done using an extended trapezoidal rule[19] quadrature over regions approximately twice the full width at half maximum of the speed distributions. Six points were used for the chlorine velocity, V_1, while two points were used for the neon velocity, V_2. This velocity averaging procedure provides much better results for time-of-flight spectra than the Gauss-Hermite quadrature used for velocity averaging of total differential cross sections.[8,10] When we simulated the argon-helium elastic scattering time-of-flight spectra of Meyer,[20] where no inelastic effects interfere, ten by ten point Gauss-Hermite quadrature could not reproduce the experiment as well as five by five points of the trapezoid technique. This simulation also accurately reproduced the observed scattering of argon from helium near points where $J(\frac{\omega}{\Omega})$ is singular, verifying the treatment of the transformation singularities. In Equation 3.13, the integrations over τ_s and τ_a were combined into a single integration with an appropriate convolution function. No correction was made for the cross-correlation time-of-flight,[11] but this omission is neglible for the slit and aperture sizes used.

The distributions for P_j were approximated by assuming Boltzmann distributions at reasonable rotational temperatures. For the chlorine beam seeded in helium the translational temperature was 2 K and the rotational temperature was chosen as 6 K. The distribution was truncated at $j = 8$. Although Boltzmann distributions have been shown not to accurately describe rotational populations in supersonic beams,[21] they are probably a reasonable approximation. The calculated scattering was relatively insensitive to the exact temperature chosen, but a definite difference was seen between assuming a 0 K

and a 6 K distribution. For fitting purposes, only the ^{20}Ne and ^{35}Cl isotopes were used, while in the final calculations all natural isotopic abundances were included.

3.3.6 Laboratory Angular distributions

The total laboratory angular distributions are found by integrating NdV:

$$S_T(\Theta_0) = \int N(V, \Theta_0)\, dV. \tag{3.14}$$

For the data for which time-of-flight measurements exist, the integral of Equation 3.14 can be evaluated by simply summing the contributions from all the channels, $S_n(\Theta)$. For the other data, some savings in computer time was found by choosing ΔV in Equation 3.12 to include all possible scattering at a given angle. Making sure to transform each cross section from the center-of-mass frame to the laboratory frame properly, the methods described above were employed for these calculations. To ensure proper averaging over the rather wide detector in the sensitive region of the diffraction oscillations, seven points were used in the Gauss-Legendre quadrature over θ for the total angular distributions. For the pure chlorine beams, the translational temperature of 22 K was used as the rotational temperature.

3.3.7 Determination of Potential Parameters

The van der Waals coefficients, $C_{6,0}, C_{6,2}, C_{8,0}$, and $C_{8,2}$, were estimated as described in Reference (8). These were not varied in the fitting procedure. The remaining parameters were varied to achieve reasonable fits to both the angular and time-of-flight distributions. Since the calculations which include full velocity and detector averaging, many initial rotational states, and different $\bar{j}$ values for different j'' values are very time consuming, initial fitting was done using a

limited amount of averaging and a reduced number of j and $\bar{j}$ values. Once the parameters were adjusted to near their final values, fine adjustments were made using the full averaging procedures. While numerical deviations were used as a guide in the selection of parameter values, no attempt was made to find the absolute minimum of the total numerical deviation of calculated scattering from the experimental data. Some experimental discrepancies in the time-of-flight data made such an attempt unproductive (see Section 3.5.2).

3.4 Results

The potential parameters determined by fitting the data are listed in Table 3.2. The simulated angular distributions are shown with the experimental data in Figure 3.2, while the time-of-flight spectra are displayed in Figure 3.3. A contour plot of the potential is shown in Figure 3.4, while Figure 3.5 shows cross sectional cuts of the potential at γ=0° and γ=90°. Figure 3.6 is included to show the Legendre polynomial expansion defined by Equation 3.15:

$$U(r,\gamma) = \sum u_i(r) P_i(cos\gamma). \tag{3.15}$$

The first five nonzero functions $u_i(r)$ are displayed.

3.5 Discussion

Several aspects of the analysis and results deserve attention. This section includes a discussion of the simulations of the total angular and the time-of-flight distributions, an examination of the rotational excitation found in the neon-chlorine system, and a comparison of the potential with other data.

Table 3.2
Morse-Morse-van der Waals potential parameters for neon-chlorine.

ϵ_0/k_B	76.5 K
ϵ_2/k_B	-42.3 K
$\epsilon_\perp/k_B$	97.6 K
$r_{m,0}$	4.52 Å
$r_{m,2}$	0.80 Å
$r_{m,4}$	-.17 Å
$r_{m\perp}$	4.05 Å
Δr_m	1.10 Å
α_0	1.65 $Å^{-1}$
α_2	-.20 $Å^{-1}$
β	7.5
$C_{6,0}/k_B$	.397 K nm^6
$C_{6,2}/k_B$	.063 K nm^6
$C_{8,0}/k_B$	.030 K nm^8
$C_{8,2}/k_B$	.015 K nm^8
ρ	4

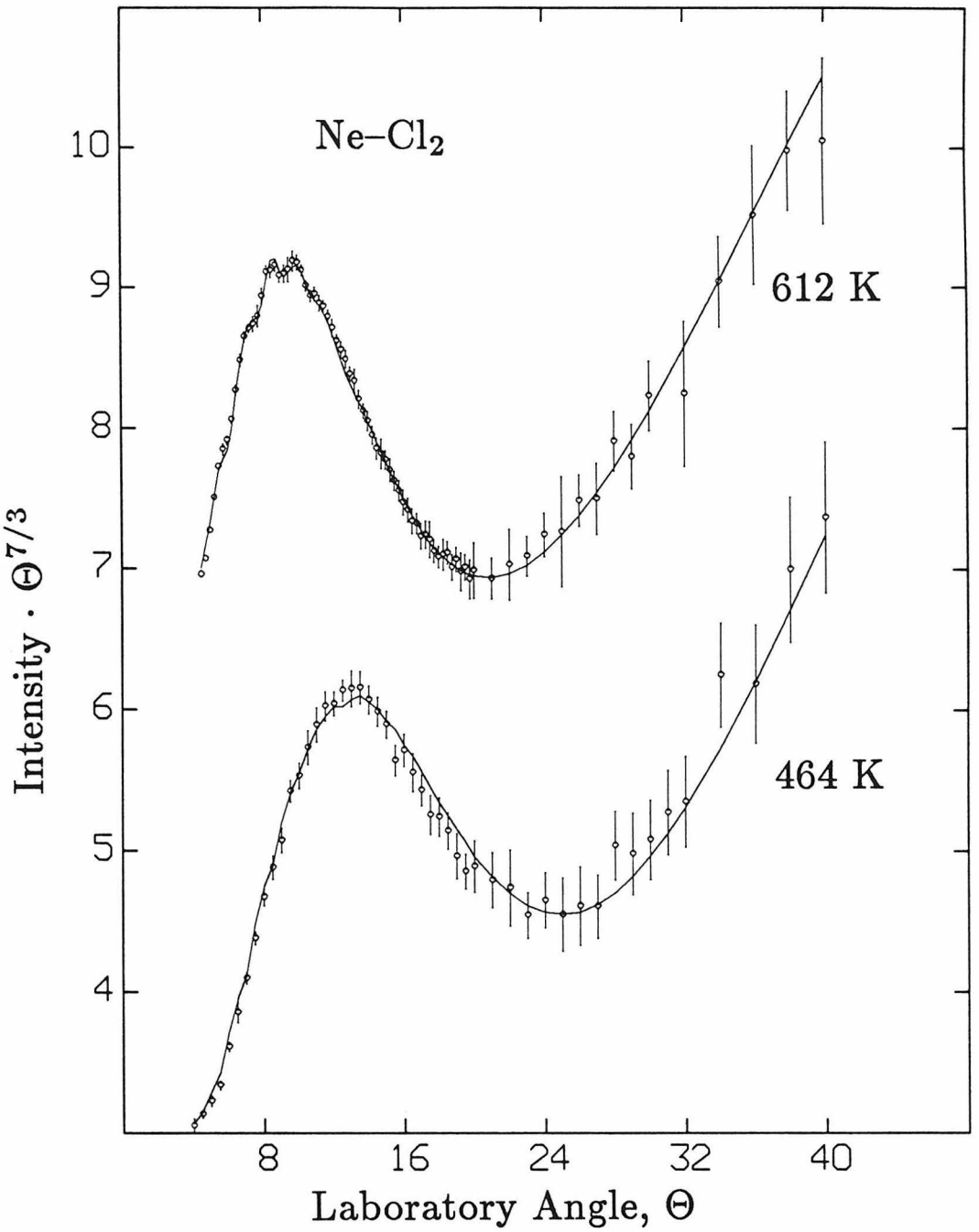

Figure 3.2 The total angular distribution of neon scattered from chlorine are compared to the calculated scattering from the potential whose parameters are given in Table 3.2.

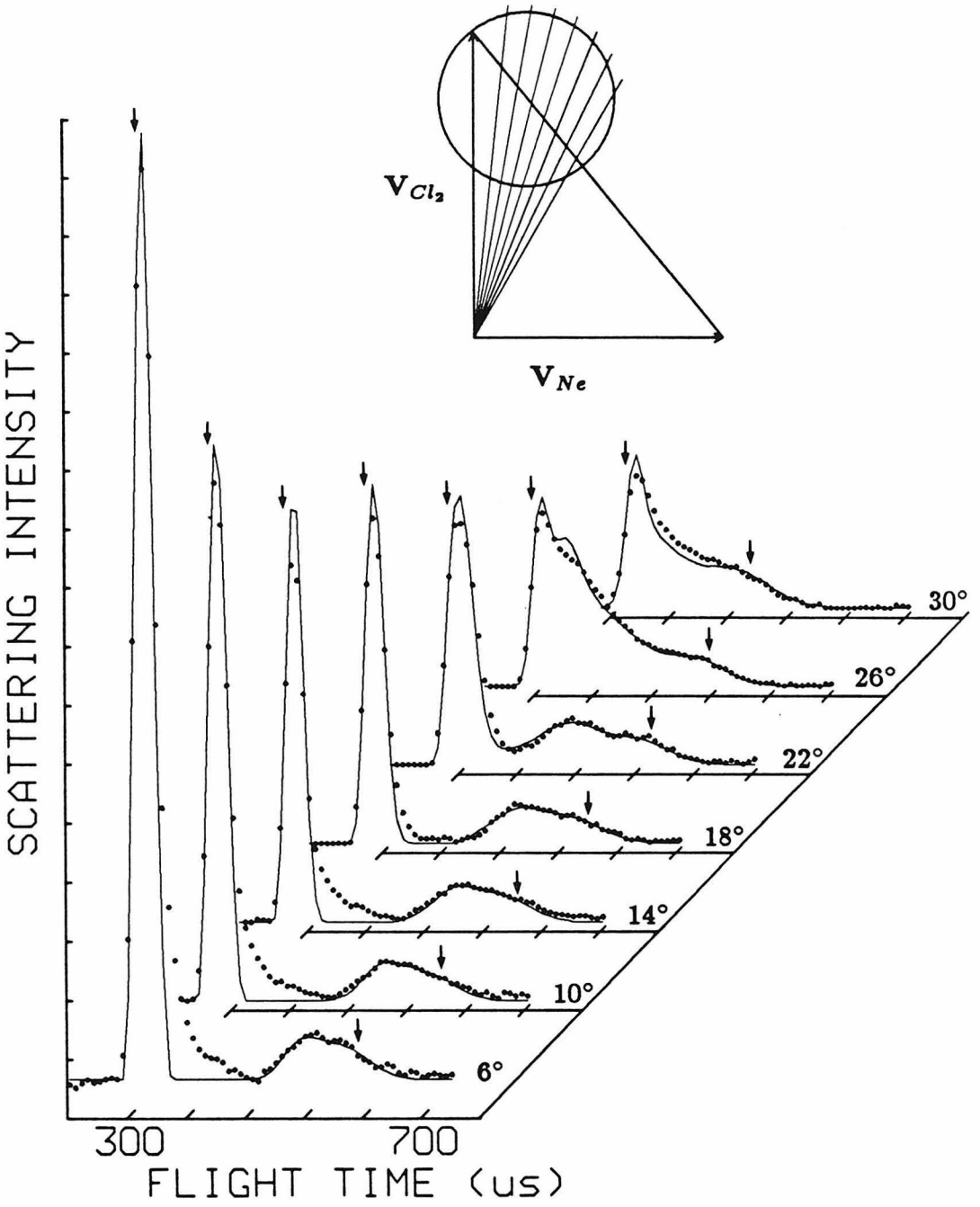

Figure 3.3 Time-of-flight spectra of chlorine scattered from neon are displayed with the simulated scattering. The inset shows a Newton diagram for the experiment with an elastic scattering circle. The arrows indicate the positions of elastic transitions. Flight times include the ion flight time on 28 μs.

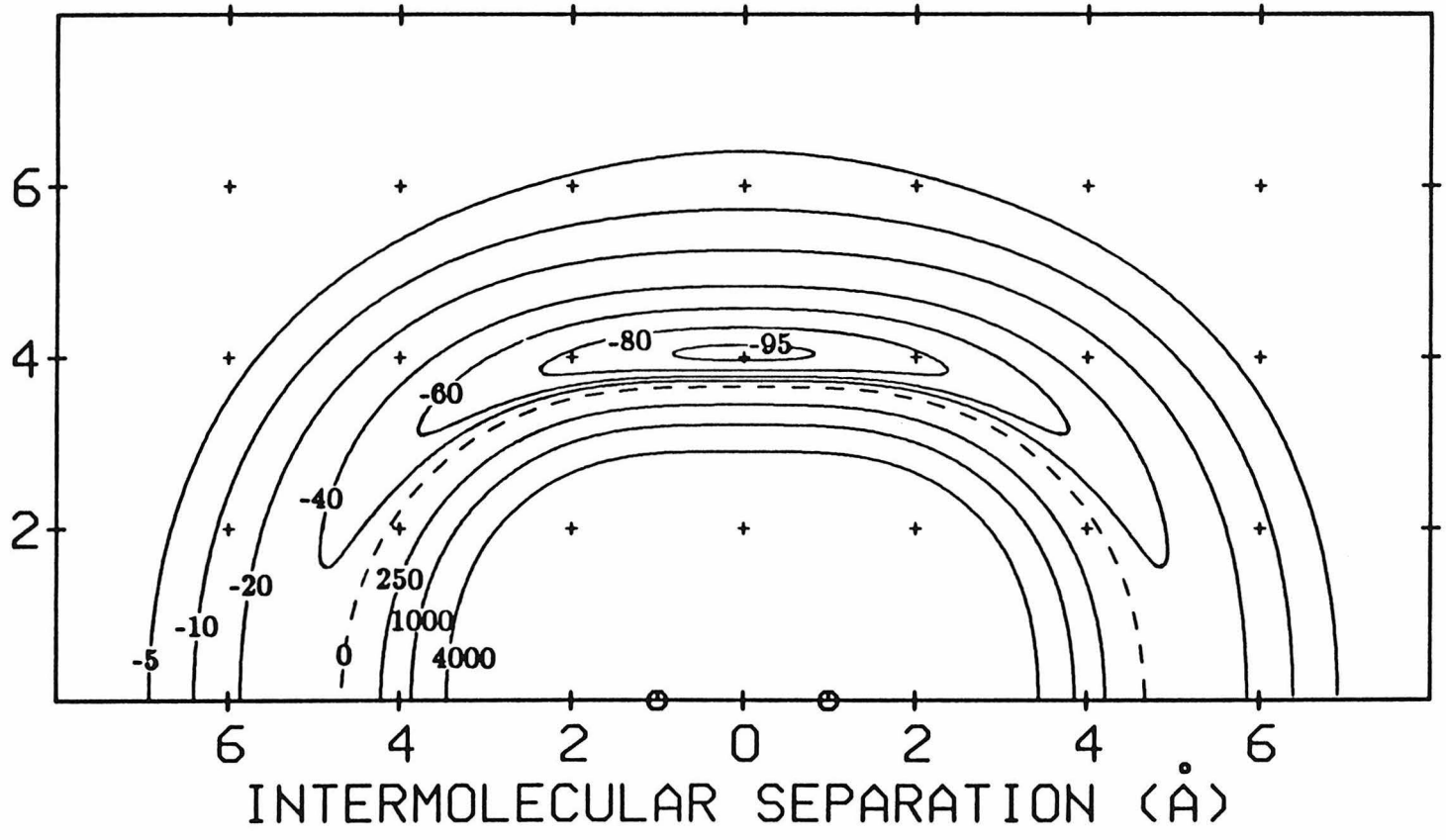

Figure 3.4 A contour plot of the Ne–Cl_2 potential. The chlorine atoms are located at 1 Å to either side of zero. The equipotential contours are in units of K.

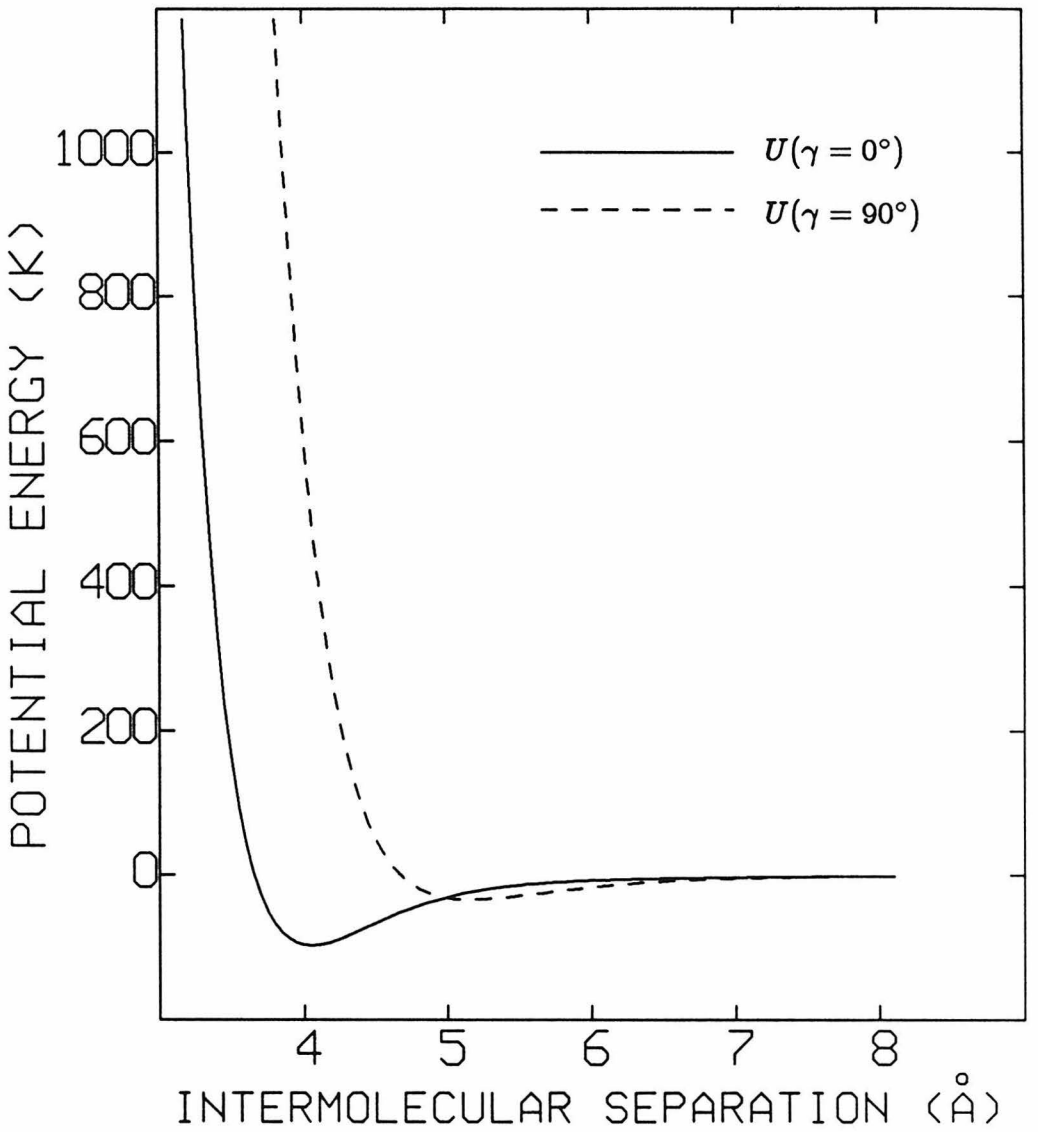

Figure 3.5 Cross sections of the Ne–Cl_2 potential at γ=0° and γ=90°.

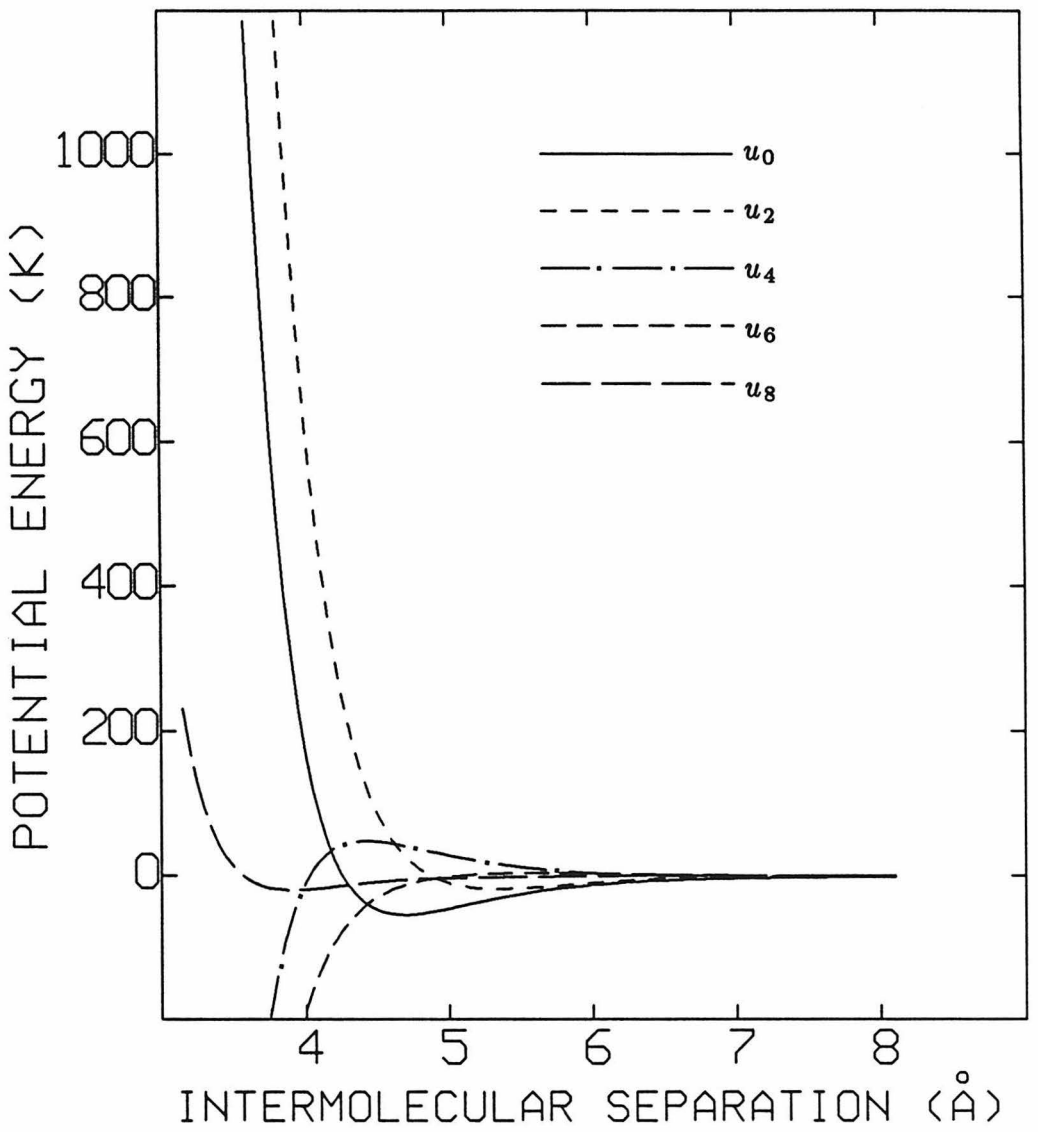

Figure 3.6 The first five non-zero functions of a Legendre expansion of the Ne–Cl_2 potential.

3.5.1 Total Angular Distributions

The IOS expression for state-to-state cross sections, Equation 3.10, includes an integration over $\cos\gamma$. The laboratory total angular distributions, being sums over the individual inelastic transitions, will be essentially an average of spherical scattering over the orientation angle γ with $\sin\gamma$ weighting. This IOSA relation is exactly true in the center-of-mass system.[14] Thus, the total angular distributions are more sensitive to the region around $\gamma = 90°$.

Since the angular distributions can be thought of as an average over "spherical" scattering from different orientations, it is not surprising that the scattering apears like that of scattering from spherical systems with averaging or damping effects present. The diffraction oscillations, small but definitely visible, in the higher energy distribution (upper curve of Figure 3.2) are sensitive to the range of the potential. These are damped to a large extent by both the anisotropic potential and instrument resolution. It was found, however, that to fit these oscillations properly, while also maintaining the correct time-of-flight spectra, determined $r_{m,0}$ or $r_{m\perp}$, the position of the minimum in the T-configuration, to within $\pm.15$ Å. In Figure 3.2, resolved rainbow structure is quite apparent. The positions of the rainbow structure should not be significantly influenced by damping and instrument resolution. These provide a measure of the attractive well of the potential. With other parameters fixed, the variation of ϵ_0 and ϵ_2 directly determines the position and damping of the rainbows. With other parameters close to the values listed in Table 3.2, ϵ_0 and ϵ_2 could vary by ± 3 K before significant deviation of the calculated distribution and data occur. Since there is some correlation with other the parameters, this uncertainty should be at least doubled.

Overall, the calculated distributions shown in Figure 3.2 fit the data fairly well at most angles. The deviations, which appear mostly in the lower energy scattering, stem from the inability to reproduce the scattering at both energies perfectly. The lower energy data would be better fit by a slightly smaller well depth, but still within 2 or 3 K of the reported value. This may be due to some systematic experimental error or to lack of complete flexibility of the potential form.

3.5.2 Time–of–Flight Distributions

The time-of-flight distributions, being comprised of the unresolved individual rotational transitions, are very sensitive to the anisotropy of the potential. The individual inelastic transitions include the spherical harmonics in the integration over γ. This makes these sensitive to variations in the scattering amplitude as a function of γ. The time-of-flight distributions show significant inelasticities which are related to the anisotropy in the range of the potential. Since the inelasticities are most directly related to the anisotropy in the location of the repulsive wall, they are indirectly related to the anisotropy in r_m. It was found that the $r_{m,2}$ term in the expansion of r_m highly influenced the average positions of the peaks in the time-of-flight, especially the highly inelastic "slow" peaks (those at longer flight times) which correspond to wide angle scattering. The particular shapes of these peaks in the time-of-flight data at 14°, 18°, and 22° are influenced by the $r_{m,4}$ term. The values of the expansion parameters of r_m are influenced by the choice of α_0 and α_2, since they determine the position of the hard wall with respect to the minimum. Furthermore, a reduced potential form has a disadvantage in that when ϵ_0 and ϵ_2 are varied, the anisotropy in

the repulsive wall changes. Thus there is some coupling between the ϵ and r_m anisotropy parameters.

In the 6°, 10°, and 14° time-of-flight spectra, deviation of the data from the simulation is apparent in the 360 to 460 μs region. No potential could fit this region while also fitting the slow time-of-flight peak distributions. Some deviation may be due to inadequate modeling, however, this region is near the center-of-mass for Cl_2–Cl_2 dimer scattering from neon. The contributions from scattering of these dimers would be localized in this region. When the stagnation pressure of the source was increased so that more dimers formed, these regions gained intensity, although reduction of the stagnation pressure below that listed in Table 3.1 did not further decrease the intensity in the regions. These relatively small descrepancies were ignored in the fitting procedure and should not affect the fitting of the slow peaks which mainly determined the anisotropy in the range of the potential.

3.5.3 The IOSA and Rotational Energy Transfer

While the uncertainties in the experimental data and in the fitting procedures introduce uncertainties in the potential, the IOSA, being an approximate theory, may also be a source of substantial uncertainty. The centrifugal sudden approximation is expected to be valid, among other conditions, for rotational transitions in which the relative kinetic energy of both the initial and final states is greater than the well depth of the interaction.[7] Since the collision energies studied here, 500 to 1500 K, are considerably larger than the maximum well depth of 120 K, this constraint will limit the validity of the CS approximation only for extremely large Δj transitions. Such transitions will tend to be sizable only at large scattering angles. The CS approximation is

also expected to break down for inelastic scattering from large impact parameter collisions. These collisions would result in very small angle scattering. Since most of the measured small angle scattering is elastic or near elastic, which is expected to be well treated in the CS approximation, this should not be a problem, at least for the total angular distributions. The validity of the energy sudden approximation relies upon the relative motion of the atom and diatom being reasonably fast compared to the rotational motion of the diatom. Since chlorine has a small rotational constant, the rotation of the chlorine will be relatively slow for all but the highest energetically accessible rotational states.

The previous discussion suggests that the IOSA should be reasonable for the total angular distributions of neon, since they are taken over a moderate range of laboratory angles where no large IOSA breakdowns are expected. The time-of-flight spectra, however, include contributions from practically all center-of-mass angles. The very inelastic transitions, occurring at large scattering angles, may not be well approximated by the IOSA. To see just how inelastic the transitions are, Figure 3.7 shows plots of $\frac{d\sigma}{d\omega}(j'' \leftarrow 0)$, as a function of j'', for several center-of-mass angles and a collision energy of 1500 K. These plots show the rotational rainbow structure typical of inelastic scattering from a mainly repulsive potential.[22] It is seen that at the smaller scattering angles the rotational energy change, while definitely not zero, is relatively small. For example, $\Delta E(10 \leftarrow 0)$ is 39 K, less than 3% of the 1500 K collision energy. At the large angles, much more inelasticity is observed. At 180°, the scattering shows significant transitions with the final rotational energy at 60% of the collision energy ($j'' = 50$). The IOSA may lose quantitative accuracy for these transitions, although qualitative accuracy would still be expected. To estimate the magnitude of possible error,

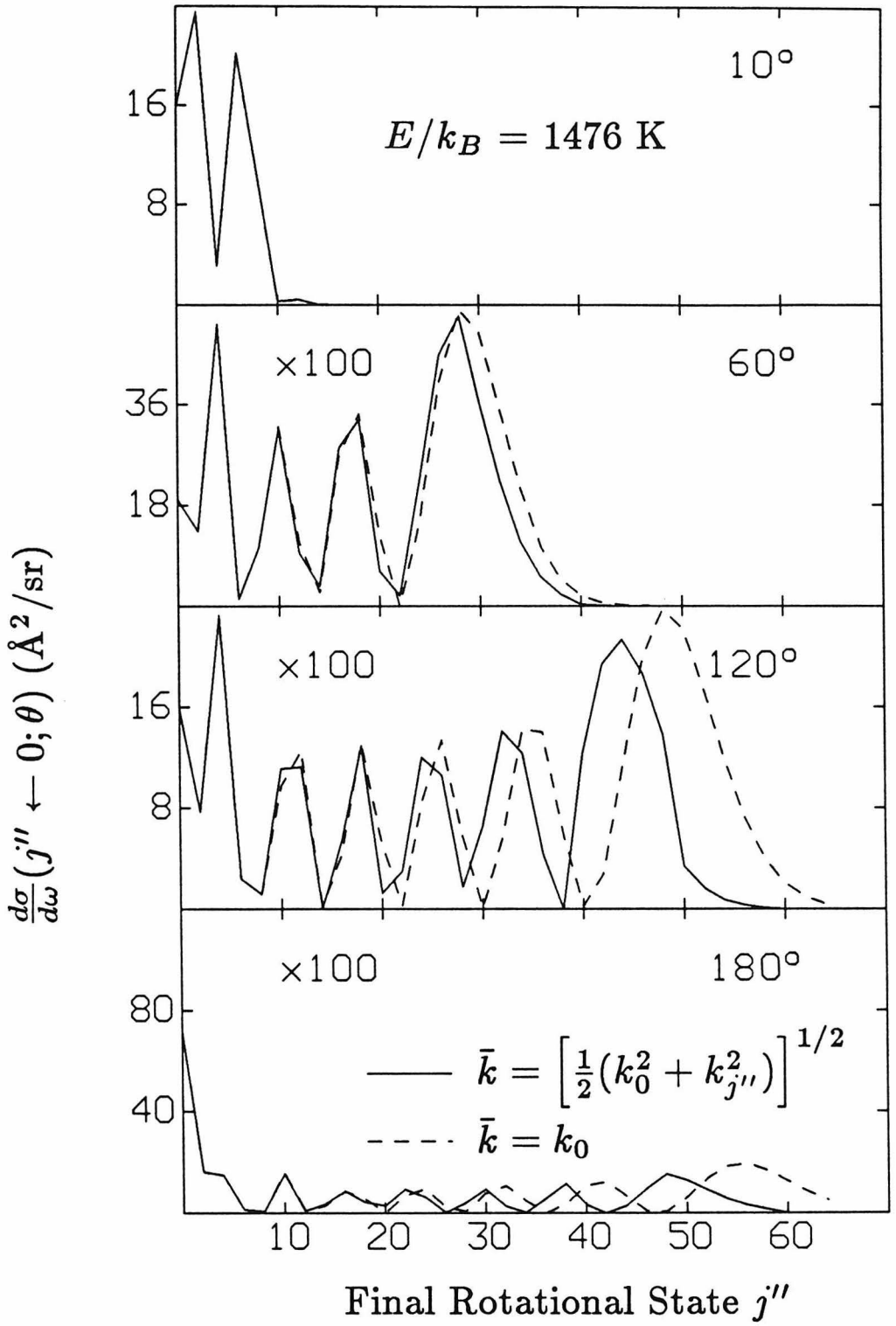

Figure 3.7 Differential cross sections for $j = 0 \rightarrow j''$ as a function of the final rotational state. The difference between two choices of $\bar{k}(\bar{j})$ is also shown. The solid lines show those cross sections which reproduce the experimental data.

the effect of the choice of $\bar{k}$ ($\bar{j}$) on the calculated scattering was investigated. The difference between choosing $\bar{k} = k_0$ and $\bar{k}^2 = \frac{1}{2}(k_0^2 + k_{j''}^2)$, which approximates the rotational energy half way between the initial and final values, is shown in Figure 3.7. When the $\bar{k} = k_0$ method is used to fit a potential, $\Delta r_m = r_{m\|} - r_{m\perp}$, where $r_{m\|}$ is the postion of the minimum in the collinear configuration, decreases by 0.1 Å. This can be used to give a range of uncertainty for Δr_m of ± 0.1 Å.

An interesting point related to the inelastic transitions and to the choice of $\bar{k}$ is the proper transformation of the inelastic cross sections from the center-of-mass system to the laboratory system for the total angular distributions. For systems with small anisotropy or small reduced mass,[24] total angular distributions have been calculated using the extremely simple formula for center-of-mass total differential cross sections:[14]

$$\frac{d\sigma}{d\omega}(\theta) = \frac{1}{2}\int \frac{d\sigma}{d\omega}(\gamma, \theta)\, d\cos\gamma, \tag{3.16}$$

where $\frac{d\sigma}{d\omega}(\theta)$ is the total differential cross section and $\frac{d\sigma}{d\omega}(\gamma, \theta)$ is the differential cross section calculated as if the scattering were elastic from the isotropic potential formed by keeping γ constant. These cross sections were then transformed as elastic. While this approximation is acceptable for systems with small velocity changes upon collision, it has been shown to be incorrect for heavy systems with large anisotropy such as Ar-CO_2,[24] especially for wide angle scattering. The present case has a moderately heavy reduced mass scattering from a relatively anisotropic potential. The simple formula of Equation 3.16 assumes $\bar{k} = k_0$. For the Ne-Cl_2 potential determined here, this choice tends to slightly overestimate the scattering at wide angles compared to the other choice of $\bar{k}$. The transformation of the cross sections, on the other hand tends to underestimate the laboratory wide angle scattering. These two effects tend to

cancel and for the potential given in Table 3.2 the use of Equation 3.16 and elastic transformations results in wide angle laboratory scattering only slightly smaller than the proper calculations. The substantial savings in computational effort afforded by Equation 3.16 make its use attractive for systems such as Ne-Cl_2.

3.5.4 Comparison With Other Results

The anisotropy in the position of the repulsive wall of the potential as measured by $\Delta\sigma = \sigma_\perp - \sigma_{||}$, where $\sigma_{||}$ is the zero crossing point of the potential in the collinear configuration and $\sigma_\perp$ is that point in the T-shape configuration, is 1.05 Å. This is very close to half the bond distance of the chlorine molecule and is close to the value of the anisotropy, 0.95 Å, found by Hoffbauer, *et al.* in the modeling of their argon-chlorine scattering data with a classical rotational rainbow analysis.[25] The absolute range of the potential is described by $r_{m\perp} = 4.05$ Å, the minimum of the potential in the T-shape. This value is very different from the the Ne–Cl_2 van der Waals bond distance of 3.565± .035 Å determined spectroscopically by Evard *et al.*[9] for the van der Waals molecule with a quantum of vibration in the chlorine-chlorine stretch. This value is clearly smaller than our value of $r_{m\perp}$ and out of the range of mutual uncertainties. While the two quantities measure different properties, our value being the minimum of the well and theirs being the expectation value of the position of the wave function in that well, it is difficult to imagine there being so large a discrepancy from this distinction.

Considerable effort was spent in constraining the $r_{m\perp}$ to values close to the spectroscopic result and varying the other parameters of the Morse-Morse-van der Waals potential form. No fit was found that satisfactorily reproduced the

diffraction oscillations of the 612 K data while still maintaining the proper time-of-flight spectra. A more flexible Morse-Morse-Morse-van der Waals forms was also tried, but it did not produce significantly better fits. A typical fit with $r_{m\perp}$ constrained to 3.5Å is shown in Figure 3.8. The fit is not unreasonable; at least one diffraction oscillation lines up well with the 612 K data. The diffraction oscillation spacing is incorrect, however.

To investigate this discrepancy in $r_{m\perp}$, we can compare other anisotropic potentials which have been determined for atom-diatom systems. The closest system is helium–chlorine.[8] It has been observed that for spherical interactions between different sized partners that the position of the minimum is largely determined by the more polarizable (larger) interaction component.[26] Using this as a guide, one would expect the minimum positions for neon–chlorine to be similar to those for helium–chlorine. Several potentials were fit to total differential cross sections in Reference (8), although no inelastic scattering was used. The total differential cross sections show pronounced diffraction oscillations. The potentials of Reference (8) show a range of r_0 from 4 Å to 4.7 Å. One (Potential B_{He}) which fits the data well has r_0=4.518 Å which is virtually identical to the r_0=4.515 Å for neon–chlorine. The anisotropy of the helium–chlorine potentials of Reference (8) is slightly larger than for neon–chlorine resulting in $r_{m\perp}$=3.85 Å for helium–chlorine. This value is in the middle of the range of 3.8 ± 0.4 Å found from low resolution laser spectroscopy of the He-Cl_2 van der Waals molecule.[27] Although the value for He-Cl_2 is smaller than the 4.05 Å value for Ne-Cl_2, the results are fairly close.

The rare gas-holgen van der Waals molecule He-I_2 is reported to have a bond length of 4.47 ± .13 Å,[28] while length of 3.7 ± 0.2 has been reported for He-Br_2.[29] Both of these studies were spectroscopic. The value for He-Br_2 seems

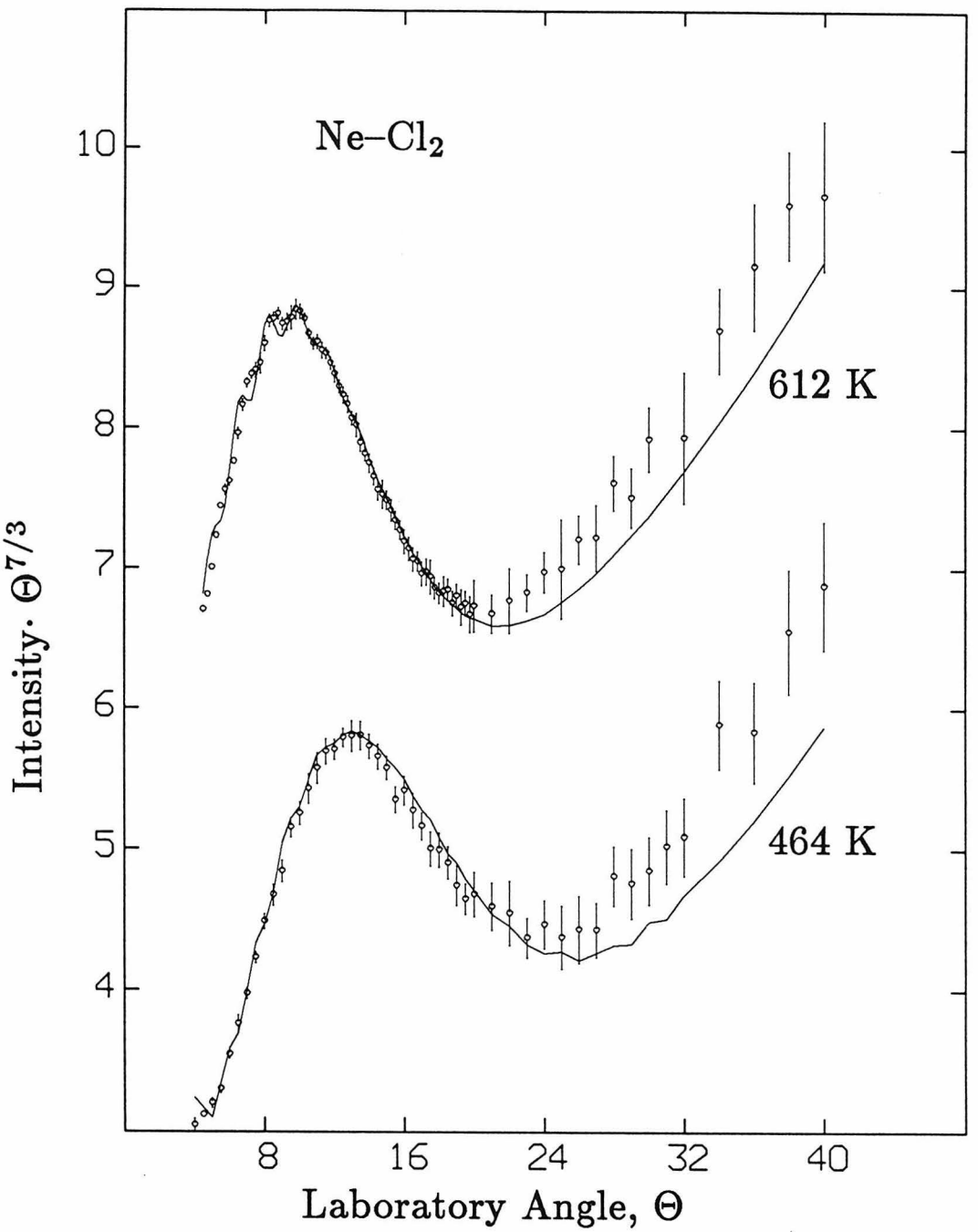

Figure 3.8 A calculation for neon–chlorine scattering from a potential with $r_{m\perp}$= 3.5 Å shows deviations in the period of the diffraction oscillations. The potential used reproduces the time-of-flight spectra accurately.

in line with the Ne-Cl_2 value of Evard, *et al.* The large He-I_2 value appears more consistent with our Ne-Cl_2 value of $r_{m\perp} = 4.05$ Å.

Examples of other systems for which experimental inelastic differential cross section data are available include helium–oxygen[30] and helium–nitrogen.[31] Potentials proposed for these systems fit the total and inelastic data well. At short ranges theoretical calculations determined the interaction energy. For helium–oxygen, $r_{m\perp}$=3.34 Å and for helium–nitrogen, $r_{m\perp}$=3.55 Å. Since oxygen and nitrogen are considerably less polarizable than chlorine, the minimum position would be expected to be significantly smaller for the oxygen and nitrogen systems.[26] Qualitatively, this is certainly consistant with our proposed potential.

The well depths of spherical interactions have been found to depend most upon the less polarizable of the two interaction partners.[26] The well parameter, ϵ_0, determined for Ne-Cl_2 is very similar to those of neon–heavier rare gas interactions.[32] The well depth in the T-shape, $\epsilon_\perp$, is very similar to those found for other neon-halogen van der Waals molecules (see Reference (8) for a comparison).

3.6 Conclusions

A model potential to describe the anisotropic interaction between a neon atom and a chlorine molecule has been determined using crossed molecular beams scattering data and the infinite order sudden approximation. The potential has been fit only to scattering data using an approximate theory, considerations which may affect its reliability.[33] The scattering data are influenced mostly by the well region and the lower part of the repulsive wall of the potential. The short range regions of the potential, which are above the scattering energies, may significantly deviate from the true potential. The long range interaction has

been approximated with van der Waals coefficients estimated from semiempirical formulas. The proposed potential does have a well depth and anisotropies which are physically reasonable. However the position of the minimum in the T-configuration appears to be approximately half an Ångstrom greater than the Ne-Cl_2 bond length found spectroscopically, a discrepancy which warrants further investigation.

3.7 References

[1] G.E. Ewing, J. Chem. Phys. **71**, 3143–3144 (1979).

[2] J.A. Beswick and J. Jortner, Adv. Chem. Phys. **47**, 363–506 (1981).

[3] K.C. Janda, Adv. Chem. Phys. **60**, 201–244 (1985).

[4] (a) D.E. Brinza, B.A. Swartz, C.M. Western and K.C. Janda, J. Chem. Phys. **79**, 1541–1542 (1983);
(b) D.E. Brinza, C.M. Western, D.D. Evard, F. Thommen, B.A. Swartz and K.C. Janda, J. Phys. Chem. **88**, 2004–2009 (1984).

[5] See, for example, U. Buck, Adv. Chem. Phys. **30**, 313 (1975).

[6] See, for example, H. Loesch, Adv. Chem. Phys. **42**, 421 (1980).

[7] For a review, see D.J. Kouri, in *Atom – Molecule Collision Theory: A Guide for the Experimentalist*, edited by R.B. Bernstein (Plenum Press, New York, 1979).

[8] M.J. O'Loughlin, *Ph.D. Thesis* (California Institute of Technology, 1985).

[9] D.D. Evard, F. Thommen and K.C. Janda, J. Chem. Phys. **84**, in press (1986).

[10] M.J. O'Loughlin, B.P. Reid, R.K. Sparks, J. Chem. Phys. **83**, 5647 (1985).

[11] For a description of cross correlation see, C.V. Nowikow and R. Grice, J. Phys. E: Sci. Instrum. **12**, 515 (1979).

[12] (a)R.T Pack, Chem. Phys. Lett. **55**, 197 (1978);
(b)R.T Pack, J.J. Valentini, and J.B. Cross, J. Chem. Phys. **77**, 5486 (1982).

[13] P.E. Siska, J.M. Parson, T.P. Schafer, and Y.T. Lee, J. Chem. Phys. **55**, 5762 (1971).

[14] G.A. Parker and R.T Pack, J. Chem. Phys. **68**, 1585 (1978).

[15] V. Khare, D.E. Fitz, and D.J. Kouri, J. Chem. Phys. **73**, 2802 (1980).

[16] J.S. Cohen, J. Chem. Phys. **68**, 1841 (1978).

[17] R.T Pack, J. Chem. Phys. **81**, 1841 (1984).

[18] G.L. Cutchen, J. Husain, and R.N. Zare, J. Chem. Phys. **69**, 1737 (1978).

[19] M. Abromowitz and I.A. Stegun, editors, *Handbook of Mathematical Functions* (Dover Publication, New York, 1965).

[20] H. Meyer, *Ph.D. Thesis* (Max-Planck-Insitut für Strömungsforchung, Göttingen, 1985).

[21] D. Bassi, A. Boschetti, S. Marchetti, G. Scoles, and M. Zen, J. Chem. Phys. **74**, 2221 (1981).

[22] See, for example, R. Schinke, H.J. Korsch, and D. Poppe, J. Chem. Phys. **77**, 6005 (1982).

[23] For examples, see, M. Keil, J.T. Slankas and A. Kuppermann, J. Chem. Phys. **70**, 541–551 (1979);
R.T Pack, E.Piper, G.A. Pfeffer, and J.P. Toennies, J. Chem. Phys. **80**, 4940 (1984) and Reference (12b).

[24] G. Rotzoll and A. Lübbert, J. Chem. Phys. **71**, 2275 (1979).

[25] M.A. Hoffbauer, S. Burdenski, C.F. Giese and W.R. Gentry, J. Chem. Phys. **78**, 3832–3837 (1983).

[26] G. Scoles, Ann. Rev. Phys. Chem. **31**, 81 (1980);
G. Luiti and F. Pirani, Chem. Phys. Lett. **122**, 245 (1985).

[27] J.I. Cline, D.D. Evard, F. Thommen, and K.C. Janda, J. Chem. Phys. **84**, 1165 (1986).

[28] R.E. Smalley, L. Wharton and D.H. Levy, J. Chem. Phys. **68**, 671 (1978).

[29] L.J. van de Burgt, J.-P. Nicolai, and M.C. Heaven, J. Chem. Phys. **81**, 5514 (1984).

[30] M. Faubel, K.H. Kohl, J.P. Toennies, and F.A. Gianturco, J. Chem. Phys. **78**, 5629 (1983).

[31] P. Habitz, K.T. Tang and J.P. Toennies , Chem. Phys. Lett. **85**, 461 (1981).

[32] R. Candori, F.Pirani, and F. Vecchiocattivi, Mol. Phys. **49**, 551 (1983).

[33] G.C. Maitland, M. Rigby, E.B. Smith, W.A. Wakeman, *Intermolecular Forces* (Oxford University Press, New York, 1981).

Chapter 4

UV Photofragmentation of 1,2-Diiodotetrafluoroethane

4.1 Introduction

Photodissociation studies of organic iodides have provided interesting systems for the study of intramolecular energy dynamics.[1] The absorption of an ultraviolet photon excites a highly repulsive electronic state causing very quick dissociation of the carbon-iodine bond. The energy of the photon, beyond that which is required to break the C–I bond, goes into fragment internal and translational energy. The iodine fragment may be in the ground electronic state ($^2P_{\frac{3}{2}}$) or in a spin-orbit excited state ($^2P_{\frac{1}{2}}$), denoted as I*. The organic fragment will have a distribution of internal energies, and if this fragment has enough internal excitation, secondary dissociation may occur.[2–5] Recently Knee, Khundkar, and Zewail have observed product formation in the photodissociation of 1,2-diiodotetrafluoroethane ($C_2F_4I_2$) at 280 nm with picosecond time resolution.[6] They report the formation of I* with a single time constant of less than a picosecond, while the formation of ground state iodine can be modeled by two different rates, one with a time constant of less than a picosecond and the other with a time constant of 32 picoseconds. The fast formation of I* is similar to the observed dissociation of other flourinated alkyl iodides containing a single iodine atom, in which virtually all dissociated iodine was electronically excited.[7] The I* from the $C_2F_4I_2$ dissociation is thus

presumed to result from an initial dissociation. The formation of unexcited iodine is suggested to occur as a secondary, unimolecular dissociation of the C_2F_4I fragment. The distribution of internal energies in the excited C_2F_4I radical may be responsible for the two appearance rates of the ground state iodine. We report here a crossed molecular-laser beams photofragmention study of 1,2-diiodotetrafluoroethane at 266 nm. The measured time-of-flight distributions of I and C_2F_4 provide translational energy distributions which are consistent with this proposed two step dissociation process.

4.2 Experimental Procedure

The crossed molecular beams apparatus has been described in previous experiments reported from this laboratory.[8] The molecular beam of 1,2-diiodotetrafluoroethane was formed by bubbling neon through a glass frit submersed in $C_2F_4I_2$ (obtained from SCM Chemicals and used without further purification) at room temperature (vapor pressure of ~30 torr). The mixture was expanded through a quartz nozzle with a 0.11 mm opening. To inhibit cluster formation, the tip of the nozzle was heated so that the gas near the opening was at 85° C. The expansion was skimmed and collimated using two stages of differential pumping, producing a beam with a 1.4° width and a 2.8° height. Table 4.1 summarizes the beam source conditions and velocity.

The 266 nm light source for the dissociation was a frequency quadrupled Nd:YAG laser from Quanta-Ray (model DCR 2A-10 with harmonic generator and prism separator). The laser was operated at 10 Hz, and the measured energy output was between ~10 and 40 mJ per pulse with a factory specified length of 5 ns. A 50 cm focal length fused silica lens outside the scattering chamber focused the light through a fused silica window into the chamber at a right angle to the

Table 4.1

Beam source conditions for the dissociation of $C_2F_4I_2$ at 266 nm. The velocity distributions were fit to the form $v^2 \exp(S^2(\frac{v}{v_0} - 1)^2)$.

Carrier gas	Ne
$C_2F_4I_2$ temperature	22°C
Stagnation pressure	300 torr
Nozzle temperature	85°C
Flow velocity, v_0	675 m/s
Speed ratio, S	13
Angular width	1.4°
Angular height	2.8°
Nozzle diameter	0.11 mm

molecular beam. At the intersection point, the laser beam had a diameter of about 2 mm and was linearly polarized in the plane defined by the two beams.

The detector, which rotates in the plane of the beams, had apertures which allowed 1° angular resolution. Photodissociated particles must traverse 34.5 cm from the beam intersection region before being ionized by an electron impact ionizer, mass filtered and detected. The discriminated data pulses were counted by a 4096 channel scaler. Data was collected by detecting m/e = 127 amu (I), at 10°, 15°, 20°, 25°, 30°, 40°, and 50° from the direction of the $C_2F_4I_2$ beam. Data for m/e = 100 amu (C_2F_4) was also detected at 20° and 30°. No C_2F_4I fragments could be observed as scattered products.

4.3 Analysis

To analyze the data, two distinct dissociation processes were assumed:

$$C_2F_4I_2(1) + h\nu(2) \rightarrow C_2F_4I(3) + I^*(4), \qquad (4.1a)$$

and

$$C_2F_4I(3) \rightarrow C_2F_4(5) + I(6). \qquad (4.1b)$$

The observation of iodine will include contributions from both proccesses while the observation of C_2F_4 will have only one contribution but one that is convoluted over both dissociation processes.

A diagram showing the velocities involved in these processes is shown in Figure 4.1. For simplicity the diagram shows only velocities in the plane defined by the beams and the detector, although scattering will occur in all three dimensions. The parenthetical labels in Equations 4.1a and 4.1b are used as subscripts in the notation to identify the different reactants and products, while the labels "a" and "b" will be used to identify each reaction. In the diagram and

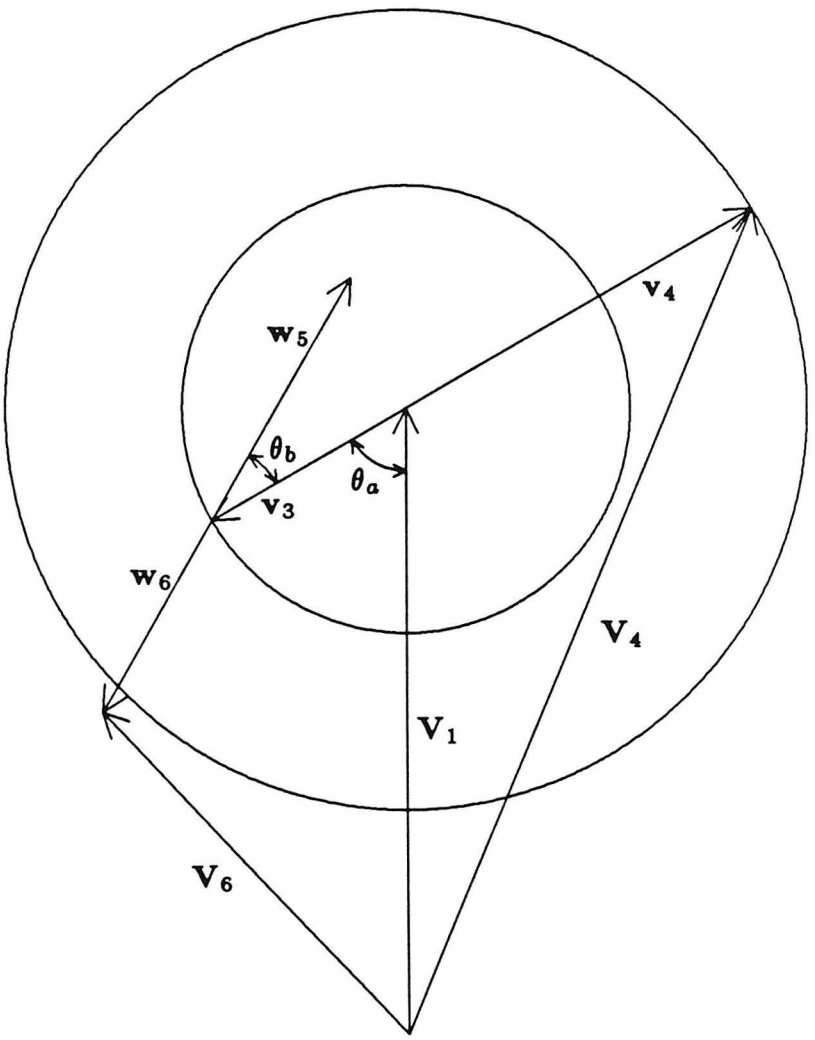

Figure 4.1 Newton diagram for the $C_2F_4I_2$ dissociation processes. The velocity of the molecular beam of $C_2F_4I_2$ is $\mathbf{V}_1$. Possible velocity vectors from the first dissociation, $\mathbf{v}_3$ for C_2F_4I and $\mathbf{v}_4$ for I^*, are shown at the tip of $\mathbf{V}_1$. The Newton circles indicate that these vectors may be oriented in any direction. The vectors also have a distribution of lengths. At the tip of the C_2F_4I velocity, $\mathbf{v}_3$, possible velocity vectors, $\mathbf{w}_5$ for C_2F_4 and $\mathbf{w}_6$ for I, are shown. The laboratory velocities for I, $\mathbf{V}_6$, and I^*, $\mathbf{V}_4$, are indicated. θ_a and θ_b denote the scattering angles for the two processes.

in the following analysis, coordinates in upper case letters refer to the laboratory frame of reference. Coordinates in lower case refer to quantities measured in center-of-mass reference frames. Because of the double dissociation, two different center-of-mass reference frames are used in the analysis. For the first dissociation process (Equation 4.1a) the center-of-mass velocities are measured in the frame of reference in which the $C_2F_4I_2$ is at rest and the polar coordinates have the direction of the molecular beam as the pole. Velocities in this frame are denoted by v's. Center-of-mass velocities of the products from the second dissociation (Equation 4.1b) are measured in the reference frame in which the C_2F_4I fragment is at rest and the angular coordinates have the direction of the C_2F_4I velocity in the $C_2F_4I_2$ reference frame as the pole. Velocities in this frame are denoted by w's.

Since the energy resolution of the experiment cannot resolve internal rovibrational energy states of the products, the scattering can be considered a continuous function of both angle and velocity. Thus, cross sections differential with respect to both angle and velocity can be defined for both dissociations described in Equations 4.1a and b. We define $\frac{d^2\sigma_j}{dv_i d\omega_j}$ to be such a cross section so that $\frac{d^2\sigma_j}{dv_i d\omega_j} dv_i d\omega_j$ is proportional to the probability that scattering from dissociation j produces fragment i with a velocity vector having magnitude between v_i and $v_i + dv_i$ and direction within the solid angle $d\omega_j = d\cos\theta_j d\phi_j$. It is convenient to relate these to a flux distribution, $F_j(E_j, \theta_j)$, as a function of the relative translational energy of the recoiling fragments, $E_j = \frac{1}{2}\mu_j v_j^2$, where μ_j is the appropriate reduced mass and v_j is the relative velocity of the fragments recoiling from disscociation j. This flux distribution is defined in Equation 4.2:

$$F_j(E_j, \theta_j) \propto \frac{d^2\sigma_j}{dv_i d\omega_j} \frac{M_j - m_i}{M_j m_i v_i}, \tag{4.2}$$

in which M_j is the total mass of the fragments recoiling from dissociation j, and m_i is the mass of fragment i. The flux distribution is proportional to the probability of products scattering with center-of-mass angle θ_j and with relative translational energy E_j, per unit time.

Laboratory scattering intensities which are functions of laboratory velocity and angle, can be related to the differential cross sections and flux distribution defined above by applying appropriate transformations. The laboratory distribution for iodine scattered from the first dissociation is given in Equation 4.3:

$$S_4(V_4,\Theta) \propto \frac{1}{V_4}\frac{d^2\sigma_a}{dv_4 d\omega_a} J(\frac{v_4,\omega_a}{V_4,\Omega}); \qquad (4.3a)$$

$$\propto \frac{m_4 m_1 V_4}{m_3 v_4} F_a(E_a,\omega_a), \qquad (4.3b)$$

where the subscripts refer to those of Equation 4.1. The m's are the masses of the indicated species and the J is the Jacobian of the transformation from the center-of-mass reference frame to the laboratory frame. A factor of $\frac{1}{V_4}$ converts the flux to number density, to which the electron impact ionization detector is sensitive.

The iodine observed from the second dissociation depends upon the fragment distribution from the first dissociation. This situation is handled in a manner similar to that used by Kroger and Riley to model the two-step, three-body dissociation of CH_3COI.[2] The probablity of the second dissociation producing scattering at a given laboratory velocity is integrated over all possible velocities of the C_2F_4I fragment. Equation 4.4 describes this procedure:

$$S_6(V_6,\Theta) \propto \frac{1}{V_6}\int_{v_3}\int_{\theta_3}\int_{\phi_3} \frac{d^2\sigma_a}{dv_3 d\omega_a}\frac{d^2\sigma_b}{dw_6 d\omega_b} J(\frac{w_6,\omega_b}{V_6,\Omega})\, d\phi_3\, d\cos\theta_3\, dv_3; \quad (4.4a)$$

$$\propto \frac{m_3^2 m_1 V_6}{m_5} \int_{v_3} \int_{\theta_3} \int_{\phi_3} \frac{v_3}{w_6} F_a(E_a, \omega_a) F_b(E_b, \omega_b)\, d\phi_3\, d\cos\theta_3\, dv_3. \tag{4.4b}$$

Similarly for detecting C_2F_4,

$$S_5(V_5, \Theta) \propto \frac{m_3^2 m_1 m_5 V_5}{m_6^2} \int_{v_3} \int_{\theta_3} \int_{\phi_3} \frac{v_3}{w_5} F_a(E_a, \omega_a) F_b(E_b, \omega_b)\, d\phi_3\, d\cos\theta_3\, dv_3. \tag{4.5}$$

S_4, S_5, and S_6 have been calculated from assumed F_a and F_b distributions and compared with experiment. The F_a and F_b flux distributions were than adjusted in a trial-and-error procedure so that the simulations matched the experimental data. To make this problem tractable, analytic forms for F_a and F_b were chosen.

The angular dependence of F_a for a single photon dissociation in the electric dipole approximation, is expected to have the form:[9]

$$F_a(E_a, \theta_a) = P_a(E_a) \frac{1}{4\pi} \left[1 + \beta P_2(\cos\theta_a)\right]. \tag{4.6}$$

The angle θ_a is measured from the direction of the molecular beam. The parameter β lies between -1 and 2. For fast dissociation, the rotational motion of the molecule can be neglected. In this limit, and for polarized light, a pure parallel type transition will have β=2, while a perpendicular transition will have β=-1. Deviation of β from these limits indicates impure transitions or a finite dissociation time. Since no distributions which are purely from the first dissociation were observed, it is not possible to estimate a center-of-mass energy flux distribution, $P_a(E_a)$, from a direct inversion of the time-of-flight distributions. For simplicity the analytical form,[10]

$$P_a(E_a) \propto (E_{max} - E_a)^{\alpha_1} (E_a - E_{min})^{\alpha_2}, \tag{4.7}$$

was chosen, where α_1, α_2, E_{max}, and E_{min} are adjustable parameters.

The energy flux distribution $F_b(E_B, \omega_b; E_f)$ for the second dissociation will depend upon the energy, E_f, in the C_2F_4I fragment, which is available to go into translation. If the energy of the photon is $E_{h\nu}$, the internal energy above the zero point for $C_2F_4I_2$ before photon absorption is E_{int}, the energy of the excited iodine is E_{I^*}, the dissociation energy for $C_2F_4I_2 \rightarrow C_2F_4I$ is $D(C_2F_4I\text{–}I)$, the dissociation energy for $C_2F_4I \rightarrow C_2F_4$ is $D(C_2F_4 - I)$ and E_a is the relative translational energy of the fragments from first dissociation, then E_f is

$$E_f = E_{h\nu} + E_{int} - E_{I^*} - D(C_2F_4I - I) - D(C_2F_4 - I) - E_a. \tag{4.8}$$

In modeling the second dissociation, the energy flux distribution was assumed to be a separable function of energy and angle:

$$F_b(E_b, \theta_b; E_f) = P_b(E_b; E_f) T_b(\theta_b). \tag{4.9}$$

This assumption facilitates the numerical modeling, and should be reasonable for a long lived complex. While several forms for the angular function were tried, a flexible form which allows asymmetric, forward-backward peaked distributions was used:

$$T_b(\theta_b) = \begin{cases} g_0 + g_1 \cos^m \theta_b & \text{for } \theta_b \leq 90° \\ g_0 + g_2 \cos^m \theta_b & \text{for } \theta_b \geq 90°, \end{cases} \tag{4.10}$$

where m is an even integer and g_0, g_1 and g_2 are adjustable constants. The form for $P_b(E_b)$ was chosen to be similar to that for P_a:

$$P_b \propto (E_f + aE_z - E_b)^{\gamma_1} E_b^{\gamma_2}, \tag{4.11}$$

where γ_1, γ_2, and aE_z are adjustable parameters.

The form given by Equation 4.11 was chosen to facilitate comparison with translational energy distributions characteristic of statistical processes. For statistical processes with no barrier in the exit channel, Quack has proposed a relatively simple formula for translational energy distributions which mimics the results from detailed statistical calculations.[11] This is given in Equation 4.12:

$$P(E_t; E) = C E_t^n \rho(E_f - E_t). \tag{4.12}$$

In this equation, C is a proportionality constant, E_t is the amount of energy in translation, n is an adjustable parameter, and $\rho(E - E_t)$ is the combined density of internal rovibronic states of the dissociation fragments. Quack has shown that variation of the parameter n over the range of zero to three can reproduce the effects of potential surface parameters of detailed statistical calculations.

The estimation of the combined density of states, ρ, for Equation 4.1b is simplified because the final fragments are tetraflouroethene and iodine. If electronic excitation of the iodine is neglected, the combined density of states of the products is only the density of states of the tetrafluoroethene. The Whitten-Rabinovitch approximation to the density of vibrational states, combined with a classical treatment of the rotational degrees of freedom,[12] gives,

$$\rho(E_f - E_t) = (E_f - E_t + aE_z)^{s+\frac{1}{2}}, \tag{4.13}$$

in which E_z is the zero point energy, s is the number of vibrational degrees of freedom, and a is an energy dependent variable. Using Equation 4.13 in Equation 4.12 gives:

$$P_b(E_b; E_f) = C E_b^n (E_f - E_b + aE_z)^{s+\frac{1}{2}} \tag{4.14}$$

This form is, in fact, the same form as that chosen for the analysis in Equation 4.11, with $\gamma_1 = n$, $\gamma_2 = s + \frac{1}{2}$, and the energy dependent parameter, a, approximated by a constant.

Using these analytical forms for $F_a(E_a, \theta_a)$ and $F_b(E_b, \theta_b)$, the scattering distributions can be calculated using Equations 4.3 through 4.5 and compared to the experimental data. The integrals in Equations 4.4 and 4.5 were evaluated numerically over the kinematically accessable regions. The resulting laboratory velocity distributions were then averaged over the beam velocity spread and detector aperture. The averaged velocity distributions were averaged over the finite length of the ionizer and transformed to time space.

The possibility of two photon processes must be considered, since the scheme:

$$C_2F_4I_2 \xrightarrow{h\nu,k_1} C_2F_4I \xrightarrow{h\nu,k_2} C_2F_4, \tag{4.15}$$

results in the same dissociation products as Equation 4.1. If the cross sections for the first and second photon absorptions are similar in magnitude, then a dependence of the scattered distributions upon the laser power might be expected. For laser powers ranging over a factor of four, no significant difference in the iodine distributions was observed. The distributions would probably be fairly insensitive to some fraction of the fragments absorbing a second photon, since, considering the energy distributions found below (see Section 4.4), all the fragments are expected to dissociate spontaneously. However, a significantly larger amount of total energy is available for the two photon process. The distributions expected from the two photon process can be modeled in the same manner as described above, with the modification of the energy and angular distributions to those appropriate for the absorption of a photon. When this is performed, significant intensity of the products is predicted at laboratory

velocities larger than those experimentally observed. Also, nearly all of the slow laboratory products are found to be absent. This modeling suggsets that, while a small fraction of the C_2F_4I fragments may absorb a second photon, most decompose spontaneously. This appears reasonable when the rate for absorption of a second photon is compared with the rate for spontaneous decay. An estimate of the average photon intensity, I, for this experiment is $\sim 1 \times 10^{17}$ photons/cm^2 ns. A typical absorption cross section, σ , on the order of 1×10^{-18} cm^2 would yield a rate constant, $k = I\sigma$, of 0.1 ns^{-1} corresponding to a time constant of 10 ns. This is some 300 times longer than the 32 ps time constant found in the picosecond spectroscopy experiments.[6] Since our experiments were performed with a photon energy ~6 kcal/mole greater than that of the picosecond spectroscopy experiment (266 nm *vs.* 280 nm), this suggests that for the two photon process to compete with spontaneous second dissociation, the cross section for absorption by C_2F_4I would have to be on the order of 10^{-16} cm^2 or larger. In the the two photon dissociation of CH_2I_2, the cross section for CH_2I (1×10^{-19} cm^2) was actually smaller than that for CH_2I_2 (2×10^{-18} cm^2).[13] However, in the case of CH_2Br_2, the cross section for CH_2Br was found to be larger than that for CH_2Br_2.[14] The necessity of a large cross section for the occurance of two photon events and the observed velocities suggest that two photon processes can be largely neglected in this analysis.

4.4 Results

Figure 4.2 shows the measured time-of-flight distributions for iodine, while Figure 4.3 shows the C_2F_4 fragment distributions. These figures also show the simulations produced by the method described in the preceding section. For the iodine distributions, the dashed lines show the modeled contributions for the two

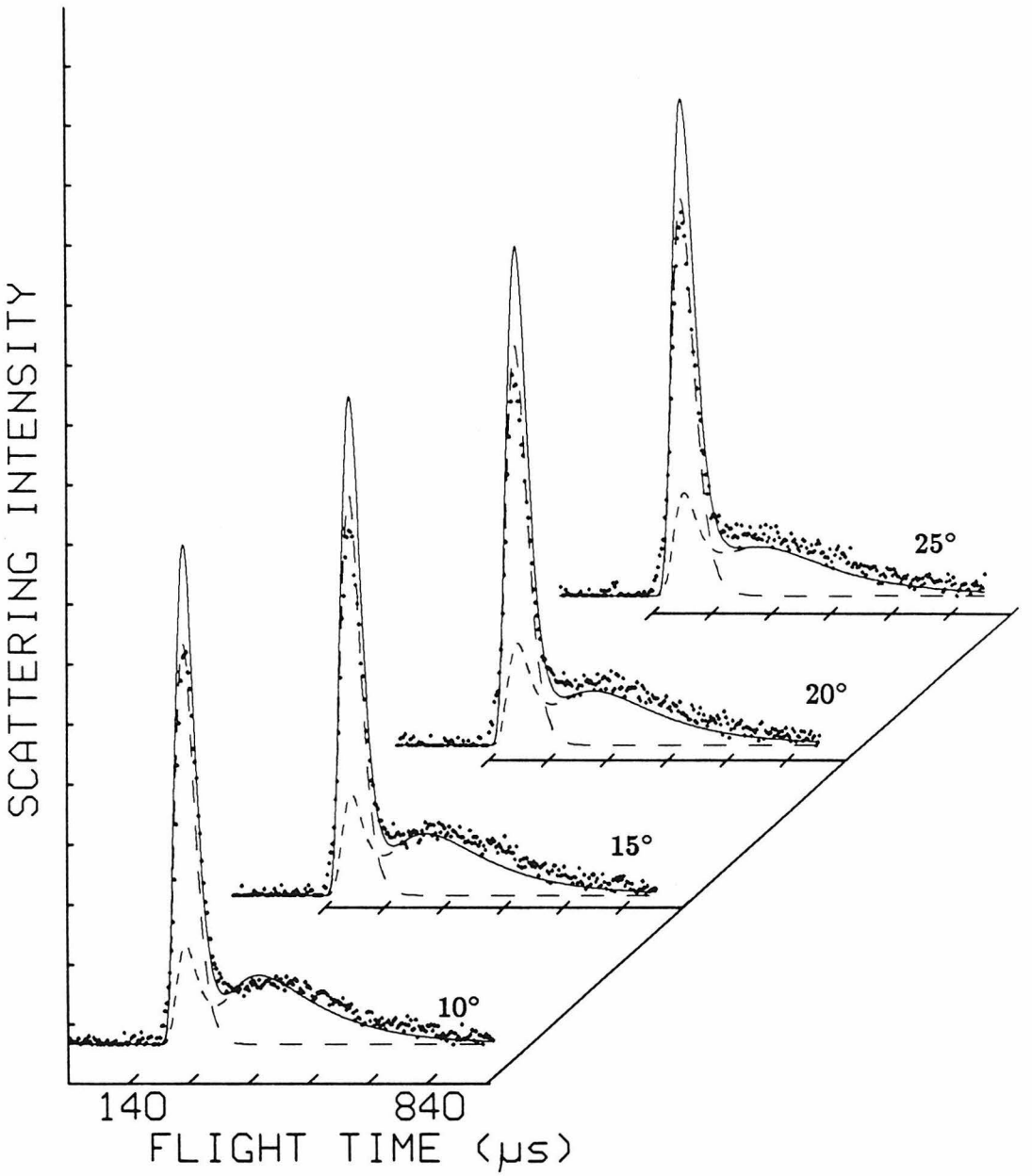

Figure 4.2a The experimental time-of-flight spectra (points) for iodine at 10°, 15°, 20°, and 25° are displayed along with the simulated spectra. The long dashed line indicates the contributions to the simulation from the first dissociation process. The short dashed line is for the second dissociation and the solid line is the sum of the two contributions.

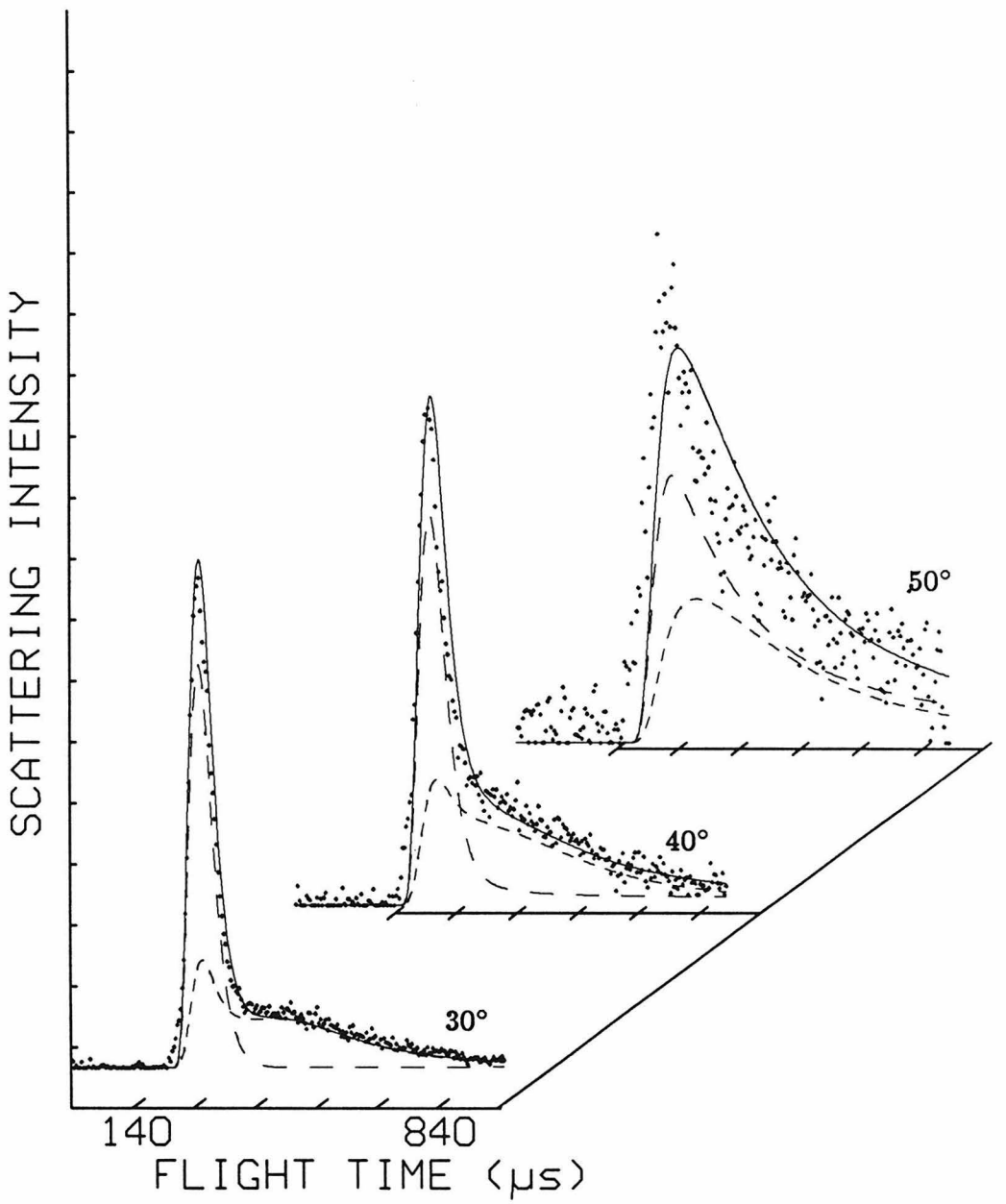

Figure 4.2b The iodine time-of-flight spectra at angles 30°, 40°, and 50°. Simulation and data are displayed as described in the caption of Figure 4.2a.

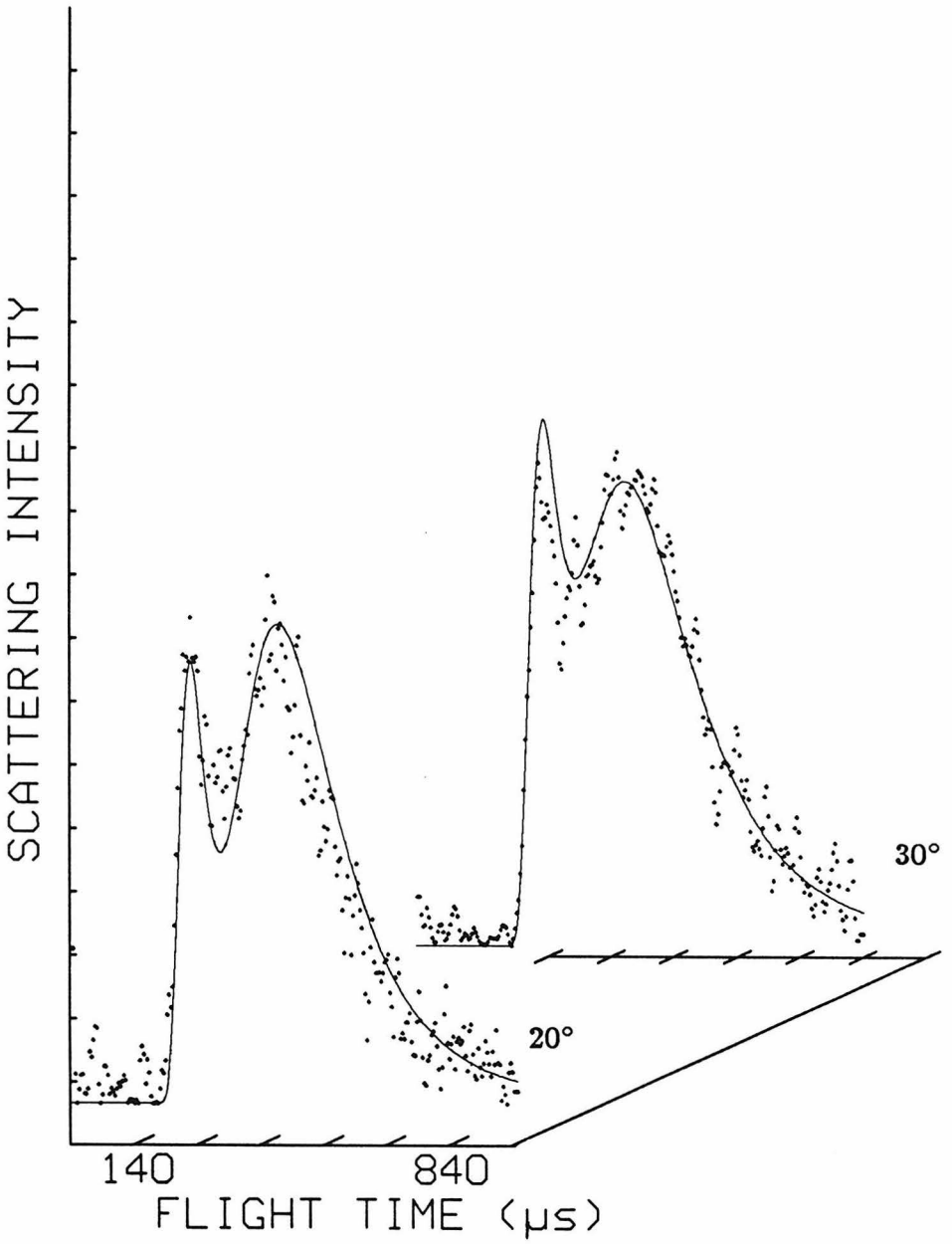

Figure 4.3 The C_2F_4 time-of-flight spectra at 20° and 30°. The solid line is the simulation of the data points. The data points have been smoothed.

dissociation processes of Equations 4.1a and 4.1b, while the solid line is their sum. Figure 4.4 shows the time integrated iodine intensities as a function of laboratory angle. The functions $P_a(E_a)$, $P_b(E_b)$, and $T_b(\theta_b)$ are shown in Figures 4.5, 4.6, and 4.7, respectively.

The parameters were determined as follows. The parameter β=1.65, which describes the angular distribution of the initial dissociation, was determined mainly by fitting the angular distributions of Figure 4.4 and the shape of the time-of-flight spectrum of iodine at 50°, shown in Figure 4.2. The inseparability of the two dissociation processes makes the determination of β somewhat uncertain. The parameter E_{max}, found in the expression for the energy flux distribution from the first dissociation (see Equation 4.7), was estimated as the photon energy minus the C–I bond energy and the I* excitation energy:

$$E_{max} = E_{h\nu} - D(\mathrm{C_2F_4I - I}) - E_{I^*} = 107.1 - 52.5 - 21.7 \approx 33 \text{ kcal/mole.}$$

The value for $D(\mathrm{C_2F_4I–I})$ was assumed to be the same as for $D(\mathrm{C_2F_5–I})$.[15] The α_1 and α_2 parameters were then determined largely from the positions and widths of the fast peaks in the iodine distributions. Of course, reasonable fits to the second dissociation had to be obtained before the parameters for $P_a(E_a)$, the estimated flux from the first dissociation, could be accurately determined.

The parameters for asymmetric angular distribution from the second dissociation (see Equation 4.10) were determined by the relative intensities of the dual peaks in the $\mathrm{C_2F_4}$ distributions. The translational energy parameters for the second dissociation were adjusted so that the positions of the $\mathrm{C_2F_4}$ peaks and the small, broad iodine peaks were in the proper locations. These parameters could be adjusted over a fairly wide range and still fit the data adequately. The average amount of translational energy was similar in the different cases,

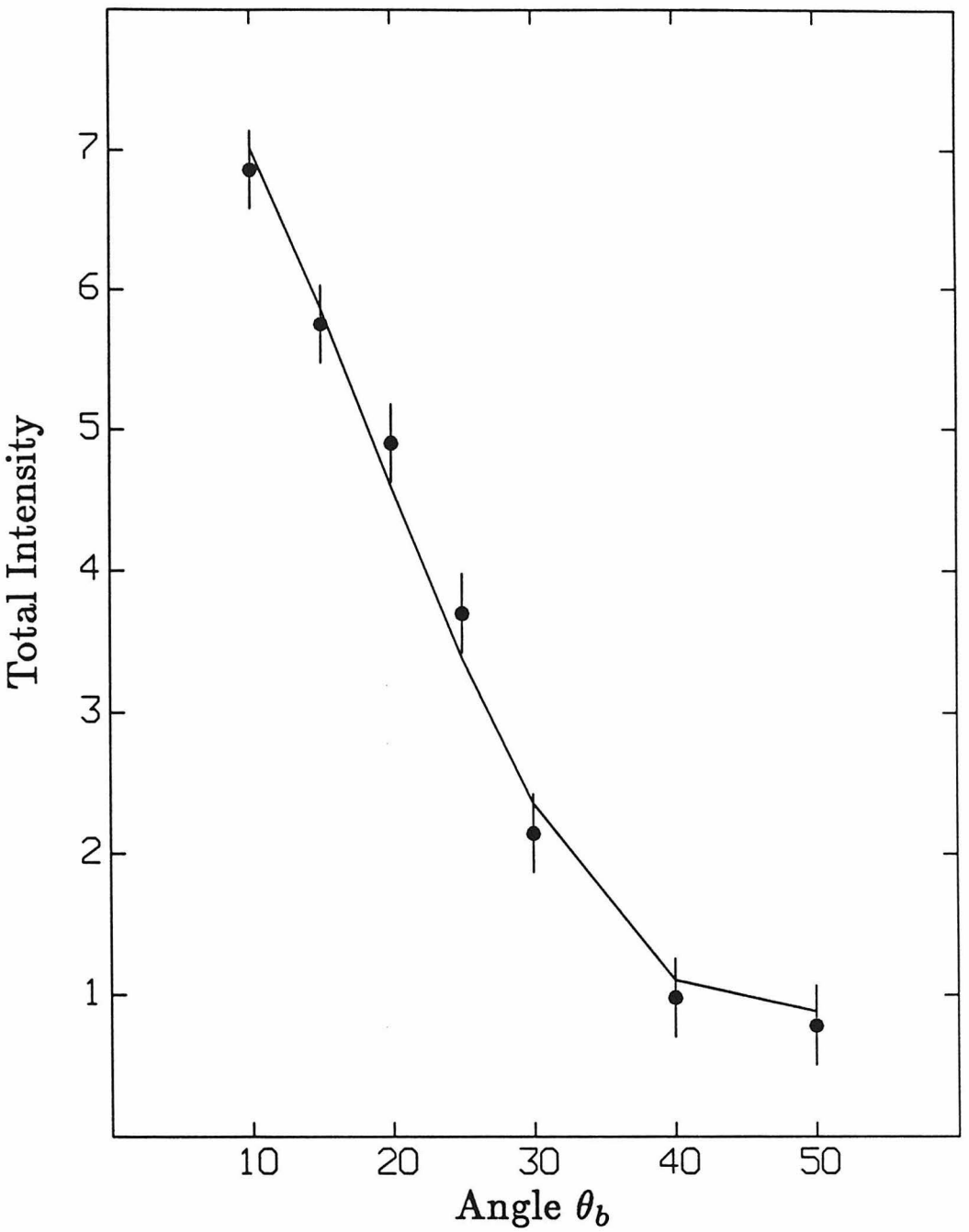

Figure 4.4 The total angular intensities for iodine are shown with the calculated intensities. Error bars are chosen to account for beam source and laser fluctuations.

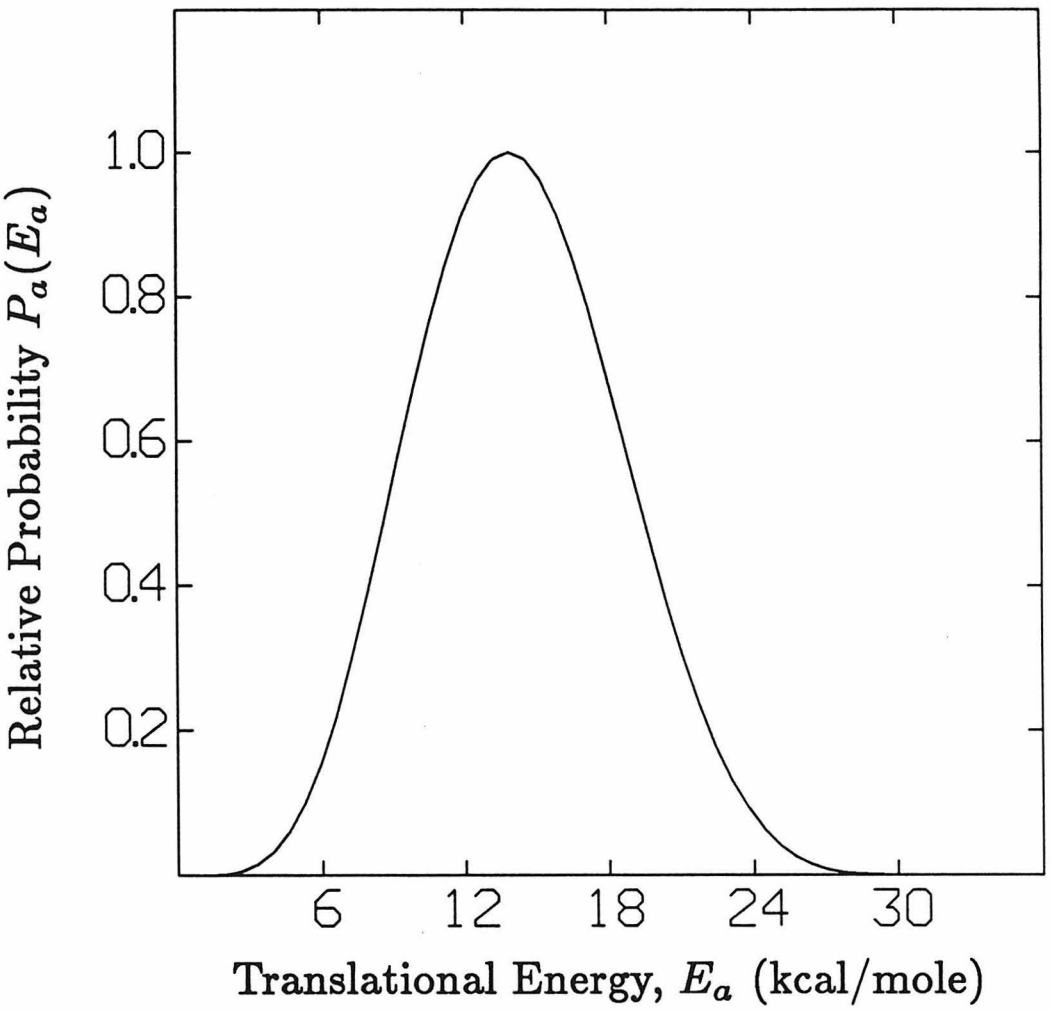

Figure 4.5 The energy flux distribution for the first dissociation, $P_a(E_a)$ is shown. The distribution peaks at 14 kcal/mole and has a full width at half the maximum (FWHM) of 11 kcal/mole.

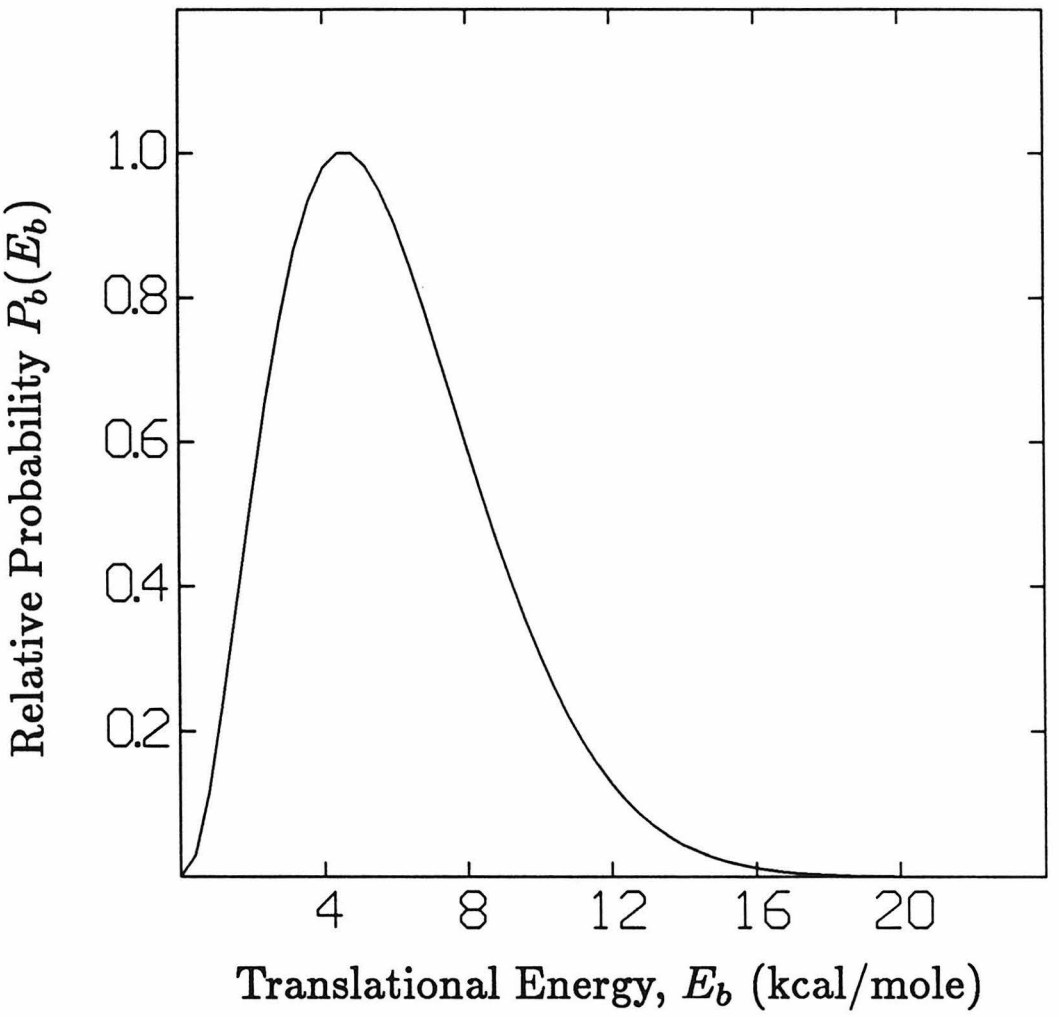

Figure 4.6 The energy flux distribution $P_b(E_b; E_f)$ is shown for the case when the C_2F_4I fragment energy is 20 kcal/mole.

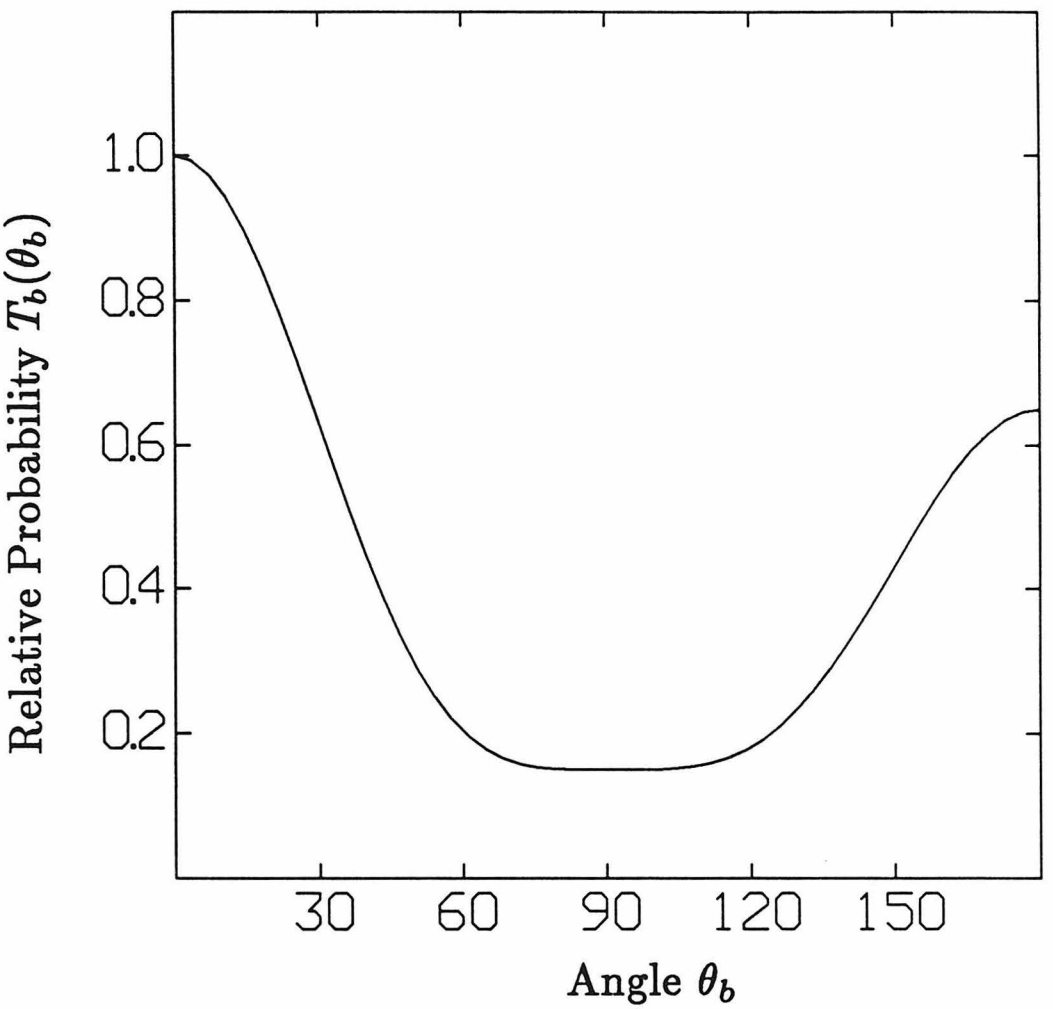

Figure 4.7 The angular distribution $T_b(\theta_b)$ for the second dissociation is shown. The angle θ_b is measured between the direction of the C_2F_4I velocity and the iodine velocity.

although the peaks and widths of the distribution could vary. To evaluate the expression for E_f (Equation 4.8), the value D(C_2F_4I-I)=0 kcal/mole, estimated by Krajnovich, *et al.* was assumed, along with no significant internal excitation of the $C_2F_4I_2$. The fit shown was chosen so that γ_1=12.5. This corresponds to choosing s = 12, which is the number of vibrational degrees of freedom in C_2F_4. The value a=0.8, was chosen to approximate the more accurate Whitten-Rabinovitch approximation for the energies encounterd. E_z was chosen as the zero point energy of C_2F_4, 13.4 kcal/mole, as calculated from the vibrational frequencies.[16] With these selections, the value of $n = \gamma_2$ was found to be 2.2.

4.5 Discussion

The initial dissociation can be compared to the photofragmentation of alkyl monoiodides. In the fragmentation of CH_3I, for example, two time-of-flight peaks are observed which correspond to the formation of excited and ground state iodine.[17] In the present case, initial dissociation to produce both ground and excited state iodine would also be expected to give two peaks; the ground state peak, however, would have laboratory velocities higher than those observed. This indicates that there is little formation of ground state I ($^2P_{\frac{3}{2}}$) from the first dissociation. This is consistent with the nearly exclusive formation of I* ($^2P_{\frac{1}{2}}$) seen for other fluorinated iodides.[7]

Impulsive models have been used to describe these fast photodissociation reactions.[18] In the "soft radical" impulsive limit, the iodine is pictured as recoiling only against the carbon atom. When the carbon atom then recoils against the rest of the fragment, rotational and vibrational modes can be excited. This limit produces high internal excitation and low translational energy. In the "rigid radical" limit, the iodine recoils against a rigid fragment with energy

partitioned only in translation and rotation. In the initial dissociation, the average fraction of available energy going into product translation, 42%, is smaller than the 53% for C_2F_4BrI,[4] indicating that the $C_2F_4I_2$ dissociation may be more toward the "soft radical" limit of impulsive models. The width of the translational energy distribution, 11 kcal/mole FWHM, is the same as that for C_2F_4BrI. The value of the angular parameter β=1.65 is slightly smaller than the 1.8 value for C_2F_4BrI, but the transition would appear to still be close to parallel to the C–I bond. The value reported here also has more uncertainty associated with it, since the second dissociation interferes with the angular distribution of the first dissociation.

The angular distribution of the second dissociation (Figure 4.7) is forward–backward peaked with respect to the direction of the C_2F_4I velocity, v_3. This behavior, observed for complexes which live longer than a rotational period, can be understood in terms of angular momentum constraints.[19] If the rotational angular momentum of the $C_2F_4I_2$ is small, then the rotational angular momentum of the C_2F_4I fragment will be approximately equal and opposite to the orbital angular momentum of the iodine and C_2F_4I fragments. This implies that the rotational angular momentum vector of the C_2F_4I will be perpendicular to its velocity. If the C_2F_4I dissociates so that most of its rotational angular momentum becomes orbital angular momentum of the C_2F_4 and I fragments, then the relative velocity of the recoiling fragments will be perpendicular to the rotational angular momentum of the C_2F_4I. The combination of the rotational angular momenta of C_2F_4I distributed uniformly but perpendicular to the C_2F_4I velocity, and the recoil velocities of the C_2F_4 and I fragments distributed uniformly but perpendicular to the C_2F_4I rotational angular momentum, yields a distribution for the recoil velocities of the C_2F_4 and

I fragments which is peaked in the forward and backward directions relative to the C_2F_4I velocity. The strongly peaked distribution seen in Figure 4.7 suggests these angular momentum constraints are very important in this system. The distribution should be symmetric in the forward and backward direction if all intermediates are long lived.

Figure 4.7, however, shows a distribution which is not symmetric. The asymmetry has been determined from the relative heights of the dual peaks in the C_2F_4 distributions. Since one of the corresponding peaks for the iodine is obscured by the initial dissociation, it is not possible to confirm this behavior with the presumably complementary behavior of iodine. There is also some discrepancy in the relative heights of the iodine peaks at the smaller angles. It is also conceivable that inadequacies of the model force the asymmetry. However, assuming that the distribution is qualitatively correct, it appears that 58% of the C_2F_4 is scattered backwards with respect to the C_2F_4I velocity. This might be expected if a fraction of the C_2F_4I fragments decay before rotating several times, a likely situation for highly internally excited fragments. Assuming this, the implication of the asymmetric, forward-backward peaked distribution is that many of the complexes are long lived with respect to a rotational period, but some complexes may live only on the order of one rotational period.

To make a rough estimate of the rotational period for the complex, we assumed the first dissociation occurs with the iodines of $C_2F_4I_2$ in an *anti* configuration, not an unreasonable assumption for a cold, supersonic expansion. The center-of-mass of the C_2F_4I fragment is then in the plane formed by the I–C–C–I chain. If we assume a geometry of the C_2F_4I fragment similar to that of the $C_2F_4I_2$, then the moment of inertia of the fragment about an axis perpendicular to the aforementioned plane and through the center of mass is approximately

600 g/mole Å^2. To determine the amount of energy imparted to the rotation of this fragment from the first dissociation requires further assumptions. In the "rigid radical" limit,[18] the amount of rotational excitation of the C_2F_4I fragment would be 10% to 20% of the available energy. Assuming a value for the rotational energy of ~3 kcal/mole gives a rotational period of ~3 ps. Using this simple estimate with the above arguments would suggest that many C_2F_4I radicals live significantly longer than 3 ps while some may survive only for about 3ps. This is simply an estimate, and our data are not particulary sensitive to the lifetime, or distribution of lifetimes, of the complex. The estimate does seem to be consistent with the two time constants of 0.5 and 32 ps for the rate of ground state iodine formation seen in the picosecond monitoring experiment.[6]

The translational energy distribution for the second dissociation (Figure 4.6) is peaked at about 25% of the available energy of the C_2F_4I fragment. As mentioned previously, the form for the translational energy distribution of the second dissociation was chosen so that it could be easily compared with statistical distributions. The value for n of 2.2 is within the range of 0 to 3 given by Quack for distributions which are consistent with statistical process.[11] Values larger than three would be considered out of the range of statistical behavior. Although this value of n is in the upper end of the region, it should be noted that an exit channel barrier is conceivable. The energy of activation for Equation 4.1b is probably in the range of the value estimated for loss of iodine from a hydrocarbon radical (~2 kcal/mole)[20] and the value estimated by Knee, *et al.* to simulate the two rates of formation seen in their experiment (~5 kcal/mole).[6] The energy of a barrier in the exit channel, the activation energy minus $D(C_2F_4\text{-}I)$, might also be on the order of 2 or 3 kcal/mole. The energy of such a barrier would be expected to appear mostly in translation, effectively decreasing the value of n.

4.6 Conclusions

The molecular-laser beams photofragmentation study of $C_2F_4I_2$ shows translational energy distributions of iodine and tetrafluoroethane which are consistent with two, stepwise dissociation processes. The first dissociation is typical for the ultraviolet absorption of alkyl iodides while the second appears to result from a unimolecular decay of the C_2F_4I fragments having a range of lifetimes from a picosecond to many picoseconds.

4.7 References

[1] S.R. Leone, Adv. Chem. Phys **44**, 255 (1982).

[2] P.M. Kroger and S.J. Riley, J. Chem. Phys. **67**, 4483 (1977).

[3] P.M. Kroger and S.J. Riley, J. Chem. Phys. **70**, 3863 (1979).

[4] D. Krajnovich, Z. Zhang, R.J. Brudzynski, and Y.T. Lee, J. Phys. Chem. **88**, 4561 (1984).

[5] T.K. Minton, P. Felder, R.J. Brudzynski, and Y.T. Lee, J. Chem. Phys. **81**, 1759 (1984).

[6] J.L. Knee, L.R. Khundkar, and A.H. Zewail, J. Chem. Phys. **83**, 1996 (1985).

[7] T. Donohue and J.R. Wisenfeld, J. Chem. Phys. **63**, 3130 (1975).

[8] M.J. O'Loughlin, B.P. Reid, and R.K. Sparks, J. Chem. Phys. **84**, 5647 (1985).

[9] R.N. Zare, Molec. Photochem. **4**, 1 (1972);
S. Yang and R. Bersohn, J. Chem. Phys. **61**, 4400 (1974).

[10] J.M. Parson and Y.T. Lee, J. Chem. Phys. **55**, 4658 (1972).

[11] M. Quack, Chem. Phys **51**, 353 (1980).

[12] Forst and Holbrook, *Theory of Unimolecular Reactions* (Academic Press, New York (1973));
P.J. Robinson and K.A. Holbrook, *Unimolecular Reactions* (Wiley, New York (1972)).

[13] P.M. Kroger, P.C. Demou, and S.J. Riley, J. Chem. Phys. **65**, 1823 (1976).

[14] D. Krajnovich, L.J. Butler, and Y.T. Lee, J. Chem. Phys. **81**, 3031 (1984).

[15] E.-C. Wu and A.S. Rodger, J. Am. Chem. Soc. **98**, 6112 (1976).

[16] J.R. Nielsen, H. Claussen and D.C. Smith, J. Chem. Phys. **18**, 812 (1950).

[17] R.K. Sparks, K. Shobatake, L.R. Carlson, and Y.T. Lee, J. Chem. Phys. **75**, 3838 (1981).

[18] S.J. Riley and K.R. Wilson, Farad. Dis. Chem. Soc. **53**, 132 (1972).

[19] W.B. Miller, S.A. Safron, and D.R. Herschbach, Farad. Disc. Chem. Soc **44**, 108 (1967).

[20] S.W. Benson, K.W. Egger and D.M. Golden, J. Am. Chem. Soc. **87**, 468 (1965).

Appendix A

Methane-Methane Laboratory Scattering Intensities

This appendix contains the laboratory scattering intensities measured in the methane-methane experiments described in Chapter 2. The scattering intensities (signal) are listed by laboratory angle (Θ). The uncertainties (Δ) used to determine the deviations of calculated distributions from these data are also given.

Table A.1. Methane-methane collision energy 1180 K

Θ	Signal	Δ	Θ	Signal	Δ
2.50	1128.06	64.30	13.00	40.48	2.34
3.00	779.10	38.40	14.00	31.87	2.24
3.50	639.82	26.14	15.00	25.89	2.18
4.00	568.32	18.13	16.00	23.63	2.18
4.50	524.68	11.89	17.00	21.60	2.20
5.00	480.67	6.64	18.00	21.95	2.22
5.50	427.72	6.60	19.00	20.43	2.24
6.00	388.27	6.48	20.00	20.56	2.00
6.50	333.66	6.36	22.00	18.02	2.02
7.00	287.76	6.24	24.00	16.14	2.00
7.50	243.07	4.88	26.00	15.88	2.00
8.00	201.02	4.68	28.00	13.16	1.96
8.50	168.60	4.46	30.00	13.19	1.94
9.00	139.61	4.24	33.00	14.91	1.90
9.50	116.77	3.98	36.00	13.74	1.86
10.00	100.00	1.28	39.00	11.64	1.72
11.00	70.21	2.98	42.00	13.56	1.70
12.00	53.07	2.60	45.00	12.21	1.66

Table A.2. Methane-methane collision energy 745 K

Θ	Signal	Δ	Θ	Signal	Δ
2.50	906.96	50.25	13.50	50.98	1.46
3.00	605.69	28.61	13.75	46.34	1.74
3.50	410.69	16.44	14.00	45.79	1.42
4.00	296.16	9.90	14.25	43.42	1.72
4.50	223.67	6.08	14.50	42.17	1.40
5.00	187.99	3.88	14.75	37.23	1.66
5.25	170.78	4.62	15.00	36.60	1.38
5.50	162.87	3.86	15.50	34.32	1.44
5.75	155.70	4.56	16.00	31.61	1.58
6.00	151.24	3.82	16.50	28.16	1.42
6.25	142.42	4.48	17.00	25.29	1.56
6.50	146.09	4.68	17.50	23.56	1.40
6.75	142.68	4.46	18.00	22.28	1.56
7.00	144.90	4.56	18.50	20.56	1.38
7.25	135.94	4.36	19.00	20.29	1.54
7.50	137.23	3.60	19.50	19.08	1.38
7.75	132.52	3.44	20.00	17.50	0.90
8.00	129.17	3.46	20.50	16.98	1.20
8.25	126.29	3.36	21.00	15.19	0.84
8.50	123.27	3.36	22.00	15.10	1.02
8.75	118.02	3.22	23.00	13.54	1.02
9.00	119.96	3.20	24.00	12.75	1.04
9.25	110.21	3.04	25.00	13.53	1.04
9.50	108.25	3.04	26.00	12.93	0.94
9.75	106.67	2.90	27.00	10.43	1.86
10,00	100.00	0.68	28.00	11.84	0.82
10.25	95.28	2.52	29.00	10.45	1.28
10.50	92.93	2.30	30.00	10.34	0.80
10.75	88.36	2.34	31.00	9.88	1.26
11.00	85.95	2.12	32.00	9.72	0.80
11.25	80.08	2.14	33.00	9.22	1.26
11.50	76.38	1.96	34.00	9.25	0.78
11.75	75.23	1.98	35.00	9.27	1.26
12.00	69.60	1.80	36.00	9.52	0.78
12.25	65.85	1.80	38.00	9.42	0.78
12.50	63.52	1.66	40.00	9.13	0.76
12.75	59.64	1.98	42.00	7.50	0.76
13.00	56.50	1.56	44.00	8.87	0.74
13.25	53.26	1.86			

Table A.3. Methane-methane collision energy 448 K

Θ	Signal	Δ	Θ	Signal	Δ
2.00	1512.74	100.08	11.50	85.20	3.18
2.25	1105.30	69.01	12.00	81.40	2.96
2.50	867.37	53.01	12.50	78.09	2.78
2.75	790.64	42.90	13.00	79.64	2.64
3.00	630.81	31.95	13.50	77.87	2.54
3.25	545.37	25.53	14.00	73.65	1.82
3.50	479.22	20.60	14.50	74.29	1.82
3.75	452.83	17.36	15.00	70.22	1.80
4.00	428.46	14.47	15.50	66.12	1.90
4.25	397.94	11.79	16.00	66.51	1.84
4.50	373.26	9.47	16.50	64.09	1.92
4.75	346.87	7.43	17.00	63.02	1.86
5.00	329.31	5.78	17.50	61.37	1.96
5.25	307.38	5.66	18.00	59.10	1.86
5.50	291.80	5.70	18.50	57.21	1.62
5.75	276.64	5.64	19.00	52.14	1.56
6.00	254.48	5.68	19.50	53.04	1.62
6.25	236.67	5.54	20.00	48.27	1.54
6.50	216.46	5.48	21.00	45.64	1.60
6.75	206.10	5.44	22.00	42.01	1.90
7.00	196.10	5.42	23.00	39.00	1.90
7.25	183.95	5.30	24.00	34.51	1.90
7.50	170.62	5.24	25.00	31.79	1.88
7.75	159.12	5.12	26.00	31.10	1.74
8.00	149.51	4.34	27.00	26.20	1.62
8.25	137.59	4.22	28.00	25.51	1.66
8.50	129.80	4.18	29.00	22.85	1.58
8.75	126.44	4.06	30.00	21.51	1.62
9.00	117.52	3.96	32.00	18.89	1.48
9.25	112.68	4.48	34.00	19.31	1.52
9.50	109.24	4.40	36.00	15.67	1.50
9.75	103.70	4.22	38.00	15.66	1.54
10.00	100.00	0.88	40.00	14.14	1.52
10.50	93.83	3.62	42.00	13.77	1.54
11.00	87.76	3.42	44.00	12.36	1.64

Appendix B

Viscosity Calculations

The transport of momentum through a dilute gas is described by the coefficient of viscosity. This transport is dependent upon scattering due to collisions of the gas molecules and hence is also dependent upon the intermolecular potential. In determining our isotropic methane potential of Chapter 2 and the neon-methane and argon-methane potentials of Reference (1) we have used literature viscosity data as a constraint. This appendix describes the details of our calculation of viscosity coefficients from a potential energy funtion.

B.1 Equations for Viscosity

At a temperature, T, the coefficient of viscosity, η, for a pure, dilute gas is given by Equation B.1,

$$\eta = f_\eta \frac{5 k_B T}{8\Omega^{(2,2)}} , \qquad (B.1)$$

in which k_B is the Boltzmann constant. In the first order Chapman-Enskog[2,3] approximation, f_η is 1 and when the second order Kihara[3,4] approximation is added,

$$f_\eta = 1 + \frac{3}{49}\left[\frac{4\Omega^{(2,3)}}{\Omega^{(2,2)}} - \frac{7}{2}\right]^2 . \qquad (B.2)$$

The collision (or omega) integrals $\Omega^{(n,s)}$, which are referred to in Equations B.1 and B.2, are given in general by Equation B.3.

$$\Omega^{(n,s)} = \frac{1}{2}\left(\frac{k_B T}{2\pi\mu}\right)^{1/2} \frac{1}{(k_B T)^{s+2}} \int_0^\infty E^{s+1} e^{\frac{-E}{k_B T}} Q^{(n)}\, dE \qquad (B.3)$$

In this equation μ is the reduced mass for a collision between two of the particles in the gas, at energy E and with generalized cross sections $Q^{(n)}$. These generalized cross sections are given by the quantum mechanical expression of Equation B.4:

$$Q^{(n)} = 2\pi \int_0^{\pi} (1 - \cos^n \chi) \frac{d\sigma}{d\omega} \sin\chi \, d\chi. \qquad (B.4)$$

The differential cross section, $2\pi \frac{d\sigma}{d\omega}$, for scattering at energy E into angle χ, is found by using a partial wave expansion to solve the Schrödinger equation. The differential cross sections are given in terms of phase shifts, η_l, for each term in the expansion. For n=0 the generalized cross section reduces to the ordinary total collision cross section. For n=1 and 2, the quantum mechanical expressions can be written in the forms given by equations B.5 and B.6, respectively:[3]

$$Q^{(1)} = \frac{4\pi}{k^2} \sum_{l=0}^{\infty} (l+1) \sin^2[\eta_{l+1} - \eta_l]; \qquad (B.5)$$

$$Q^{(2)} = \frac{4\pi}{k^2} \sum_{l=0}^{\infty} \frac{(l+1)(l+2)}{(2l+3)} \sin^2[\eta_{l+2} - \eta_l]. \qquad (B.6)$$

We obtained a slightly more complicated, but still relatively simple formula for n=3 as shown in Equation B.7:

$$Q^{(3)} = \frac{4\pi}{k^2} \sum_{l=0}^{\infty} \left[\frac{(l+3)(l+2)(l+1)}{(2l+5)(2l+3)} \sin^2(\eta_{l+3} - \eta_l) + \frac{3(l^2+2l-1)(l+1)}{(2l+5)(2l-1)} \sin^2(\eta_{l+1} - \eta_l) \right]. \qquad (B.7)$$

In these expressions, k, the wave number of the collision is defined by $E = \hbar^2 k^2$. The cross section $Q^{(2)}$ of Equation B.6, when used in Equations B.1, B.2, and B.3, is all that is needed to define the viscosity of a pure gas.

When a gas is a mixture of two components the expression for η given by B.1 is not sufficient. In this case, to first order,[3]

$$\eta_{mix} = \frac{H_{22}x_1^2 - 2H_{12}x_1x_2 + H_{11}x_2^2}{H_{11}H_{22} - H_{12}^2}, \qquad (B.8)$$

in which

$$H_{11} = \frac{x_1^2}{\eta_1} + \frac{2x_1x_2}{m_1 + m_2}\left[\frac{16\mu_{12}\Omega_{12}^{(1,1)}}{3k_BT} + \frac{m_2\mu_{12}}{m_1\eta_{12}}\right], \qquad (B.8a)$$

$$H_{22} = \frac{x_2^2}{\eta_2} + \frac{2x_1x_2}{m_1 + m_2}\left[\frac{16\mu_{12}\Omega_{12}^{(1,1)}}{3k_BT} + \frac{m_1\mu_{12}}{m_2\eta_{12}}\right], \qquad (B.8b)$$

and

$$H_{12} = -\frac{2x_1x_2}{m_1 + m_2}\left[\frac{16\mu_{12}\Omega_{12}^{(1,1)}}{3k_BT} - \frac{\mu_{12}}{\eta_{12}}\right]. \qquad (B.8c)$$

The mole fractions of components 1 and 2 in the mixture are x_1 and x_2, their masses are m_1 and m_2, and their reduced mass is μ_{12}. The viscosity coefficients of these pure gases are η_1 and η_2. The subscript on $\Omega_{12}^{(1,1)}$ indicates that the collision integral is for collisions between the two different gas components. Second order corrections are more complicated, involving higher order collision integrals and cross sections ($Q^{(3)}$, for example), and were not used.

B.2 Numerical Evaluation

The general method used to evaluate the equations of Section B.1 is that outlined and used by Pack.[5,6] To evaluate the collision integrals, whence the viscosities are calculated, ten point Gauss-Laguerre quadrature was employed. The integrand must be evaluated at each of the ten points in the quadrature for each of the 18 temperatures at which the calculations were compared with

experimental methane data. To perform these evaluations, generalized cross sections (and hence phase shifts) have to be calculated at 180 energies. Instead of performing the evaluation of the cross sections at all energies, the phase shifts were evaluated at 30 energies logarithmically spaced between 13 and 30,000 K. Below 60 K an exact quantum routine was used to determine the phase shifts, while above this energy JWKB phase shifts were employed. The maximum partial wave used in the summations of equations B.5 and B.6 was given by $50+12k$ where k is the wave number in atomic units. The generalized cross sections obtained at the 30 energies were then used along with four point Lagrange interpolation to determine the integrands of the collision integrals at all 180 points.

B.3 Computer code

The FORTRAN subroutine VISCOUS is used to calculate viscosities from an intermolecular potential provided by the user. It was designed to be used with our modified version of program ELASTIC written by M. F. Vernon.[8] ELASTIC provides the input for VISCOUS as well as for elastic scattering[8] and virial coefficient calculations.[9] A program to run the subroutine alone is provided here to indicate necessary input.

The calculations follow the method outlined above. The potential is generated within the program by calls to a subroutine, POT, which is external for versatility. POT operates in a reduced format (input is $x = r/r_m$ and output is $V(x) = U(r)/\epsilon$) and calculates an analytical potential from parameters passed to the subroutine in array A. Examples of such potentials can be

found in Reference 8. The input data, including the experimental values of the viscosity, the associated errors, and parameters for the calculation are passed to the subroutine from the calling program through the common block, COMMON/VIS. The calculated viscosities are then passed back to the calling program in that same common block.

The collision integrals generated by this routine were compared with those given by Pack *et al.*[7] for Kr-Xe and were found to be in good agreement. The phase shift routines JWPS, for JWKB phase shifts, and EXPS, for exact phase shifts, were modified from the phase shift routines of Reference (8). The phase shifts generated from both routines for a Lennard-Jones 6:12 potential were found to be in very good agreement with those given by Bernstein.[9]

```
C     SUBROUTINE VISCOUS calculates viscosity and diffusion
C     coefficients for a given potential
C
C     SUBROUTINES needed are POT, and versions of the EXACT and
C     JWKB phase shift routines entitled EXPS and JWPS
C
C     VARIABLES:
C
C     A(15) = potential parameters
C     OMEGA1(25) = (1,1) collision integral
C     OMEGA2(25) = (2,2) collision integral
C     ENERGY(50) = energies at which generalized cross
C     sections are evaluated
C     Q1(50) = 1st generalized cross section
C     Q2(50) = 2nd generalized cross section
C     U(25) = points for Gauss-Laguerre quadrature
C     W(25) = weights for Gauss-Laguerre quadrature
C     ETA(2500) = phase shifts
C     variables in POTX - see exact phase shift routine
C     ELOW = lowest energy for cross section calculation
C     EHIGH = highest energy for cross section calculation
```

```
C     NEN = number of energies at which cross sections are calculated
C     at each energy LMAX = YIL+YSL*K phase shifts are calculated
C     K is the wavenumber of the system in atomic units
C     at energies<ESW use exact phase shifts;
C     at energies>ESW use JWKB approximation
C     IPRV = 0 no printing of intermediate results
C     = 1 causes printing intermediate results
C     = 2 causes more printing
C     VISCD(25,10) = viscosity data
C     (temperature,mole fraction of component No. 1)
C     (Quantities in parentheses refer to the quantities which vary when
C     (the indices of the array variables vary.)
C     VISC1(25) = viscosity of pure component No. 1
C     (temperature) - for mixtures
C     VISC2(25) = viscosity of pure component No. 2
C     (temperature) - for mixtures
C     VISCE(25,10) = viscosity errors (temperature,mole fraction)
C     VISCT(25) = temperature of viscosity data
C     NT = number of temperatures for which there are data
C     VISC(25,10) = calculated viscosities (temperature,mole fraction)
C     IVFLAG = 0 for no viscosity calculation
C     = 1 for a pure gas viscosity calculation
C     = 2 for a mixture viscosity calculation
C     PRIM = mass of component No. 1
C     SECM = mass of component No. 2
C     NX(25) = number of mole fractions for which there are data
C     (temperature)
C     NVIS = total number of different viscosities calculated
C     XMOLE = mole fraction of component No. 1 (temperature, mole fraction)
C     NGL = number of points in Gauss-Laguerre quadrature
C     NL = number of points in Legendre interpolation of cross sections
      SUBROUTINE VISCOUS(VISDEL2,A,RM)
      DIMENSION A(15),OMEGA1(25),OMEGA2(25)
      DIMENSION X(10),ENERGY(50),Q1(50),Q2(50)
      DIMENSION U(25),W(25)
      DIMENSION V1(10),VP(10)
      COMMON/ATE/ETA(2500)
      COMMON/POTX/V(2001),XM2(2001),XSTART,XSTEP,RNPHAS
     &,ERROR
      COMMON/VIS/ELOW,EHIGH,NEN,YIL,YSL,ESW,IPRV,
     &VISCD(25,10),VISC2(25)
     &,VISCE(25,10),VISCT(25),NT,VISC(25,10),IVFLAG,SECM
```

```
     &,PRIM,VISC1(25)
     &,NX(25),NVIS,XMOLE(25,10)
      DATA BZ/20.7477/
      DATA NGL/10/,NL/6/
      DATA (U(I),I=1,10)/29.920697,21.996586,16.279258,11.843786,
     &8.330153,5.552496,3.4014337,1.8083429,.72945455,.13779347/
      DATA (W(I),I=1,10)/9.911827E-13,1.839565E-9,4.249314E-7,
     &2.825923E-5,7.530084E-4,9.501517E-3,6.208746E-2,2.180683E-1,
     &4.011199E-1,3.084411E-1/
C
C    Initialize OMEGA arrays
C
      DO 2 I=1,25
      OMEGA1(I)=0.
2     OMEGA2(I)=0.
C
C    Set up potential array for calculation of exact phase shifts
C
      IF(ELOW.GT.ESW) GOTO 12
      XMIN=XSTART
      XH=XSTEP
      L=INT(RNPHAS)
      X(1)=XMIN-XH
      DO 10 I=1,L
      X(1)=X(1)+XH
      CALL POT(X,A,V1,VP,1,RM)
      V(I)=V1(1)*BZ
      XM2(I)=1./(X(1)*X(1))
10    CONTINUE
12    IF(IPRV.NE.2) GOTO 15
      WRITE(6,11) (XM2(I),V(I),I=1,L)
11    FORMAT(2X,6E10.4)
15    CONTINUE
C
C    Set up energies at which generalized cross sections
C    are calculated
C
      DE=(EHIGH/ELOW)**(1./(FLOAT(NEN)-1.))
      ENERGY(1)=ELOW
      DO 100 I=1,NEN
      RK=0.107428*SQRT(RM*ENERGY(I))
      LMAX=INT(YIL+YSL*RK)
```

```
      IF (LMAX.GT.2500) LMAX=2500
      IF (ENERGY(I).GT.ESW) GOTO 50
C
C     Do exact phase shifts
C
      ZE=ENERGY(I)*0.001987
      IF (IPRV.EQ.2)WRITE(6,2000) ENERGY(I),LMAX
2000  FORMAT(' ENTERING EXPS AT ENERGY ',F10.4,' AND LMAX = '
     &,I10)
      CALL EXPS(A,RM,ZE,LMAX,0)
      GOTO 60
C
C     Do JWKB phase shifts
C
50    ZE=ENERGY(I)*0.001987
      IF (IPRV.EQ.2)WRITE(6,2001) ENERGY(I),LMAX
2001  FORMAT(' ENTERING JWPS AT ENERGY ',F10.4,' AND LMAX = '
     &,I10)
      CALL JWPS(A,RM,ZE,LMAX,0)
60    Q1(I)=0.
      Q2(I)=0.
C
C     Calculate generalized collision cross sections
C
      DO 70 J=1,LMAX-2
      RJ=FLOAT(J)
      Q1(I)=Q1(I)+RJ*(SIN(ETA(J+1)-ETA(J))**2)
70    Q2(I)=Q2(I)+RJ*(RJ+1.)/(RJ+.5)*(SIN(ETA(J+2)-ETA(J))**2)
      RJ=RJ+1.
      J=LMAX-1
      Q1(I)=Q1(I)+RJ*(SIN(ETA(J+1)-ETA(J))**2)
      QU1=3.51894E-20/(RK*RK)
      Q1(I)=QU1*Q1(I)
      Q2(I)=QU1*.5*Q2(I)
      ENERGY(I+1)=ENERGY(I)*DE
100   CONTINUE
C
C     At each temperature Legendre interpolation is used to
C     determine the generalized cross sections at the points
C     where Gauss-Laguerre quadrature is performed to compute
C     the integral cross sections OMEGA1 and OMEGA2
C
```

```
C       Calculations are done at NT temperatures
C
        DO 300 N=1,NT
        OMEGA3=0.
        INDEX=NEN+1
C
C       OMEGAS are calculated using NGL point quadratures
C
        DO 200 I=1,NGL
        EK=U(I)*VISCT(N)
C
C       Find range of NL points for interpolation
C
110     INDEX=INDEX-1
        IF(EK.GT.ENERGY(INDEX).OR.INDEX.LE.1) GOTO 120
        GOTO 110
120     ITOP=MIN0(INDEX+NL/2,NEN)
        ITOP=MAX0(ITOP,NL)
        ITOP=ITOP+1
C
C       Do interpolation
C
        Q1I=0.
        Q2I=0.
        DO 140 J=1,4
        PROD=1.
        DO 130 K=1,4
        IF (J.EQ.K) GOTO 130
        PROD=PROD*(EK-ENERGY(ITOP-K))
       & /(ENERGY(ITOP-J)-ENERGY(ITOP-K))
130     CONTINUE
        Q1I=Q1I+Q1(ITOP-J)*PROD
        Q2I=Q2I+Q2(ITOP-J)*PROD
140     CONTINUE
C
C       Do quadrature
C
        TEMP=U(I)*U(I)*W(I)
        OMEGA1(N)= OMEGA1(N)+Q1I*TEMP
        QQQ=Q2I*TEMP*U(I)
        OMEGA2(N)= OMEGA2(N)+QQQ
        OMEGA3=OMEGA3+QQQ*U(I)
```

```
200     CONTINUE
        TEMP=18.188*SQRT(VISCT(N)/RM)
        OMEG1=OMEGA1(N)
        OMEG2=OMEGA2(N)
        OMEGA3=OMEGA3/4.
        FK=1.+3./49.*(4.*OMEGA3/OMEG2-3.5)**2
        OMEGA1(N)=OMEGA1(N)*TEMP
        OMEGA2(N)=OMEGA2(N)*TEMP
C
C       If the calculation is for a mixture use OMEGAS and pure viscosities
C       to calculate mixture viscosity
C
        IF (IVFLAG.EQ.2) GOTO 225
C
C       For a pure gas calculate viscosty from OMEGA2
C       FK is a factor for the second order Kihara approximation
C
        VISC(N,1)=FK*8.627E-17*VISCT(N)/OMEGA2(N)
        GOTO 240
225     HTEMP=11.58866E+16*RM/((SECM+PRIM)*VISCT(N))
        H11TEMP=HTEMP*(.6666667*OMEGA1(N)+.2*SECM/PRIM
       & *OMEGA2(N))
        H22TEMP=HTEMP*(.6666667*OMEGA1(N)+.2*PRIM/SECM
       & *OMEGA2(N))
        H12TEMP=HTEMP*(.6666667*OMEGA1(N)-.2*OMEGA2(N))
        DO 230 J=1,NX(N)
        X1=XMOLE(N,J)
        X2=1.-XMOLE(N,J)
        H11=X1*X1/VISC1(N)+X1*X2*H11TEMP
        H22=X2*X2/VISC2(N)+X1*X2*H22TEMP
        H12=-X1*X2*H12TEMP
        HDIF=H11*H22-H12*H12
        VISC(N,J)=(H22*X1*X1-2.*H12*X1*X2+H11*X2*X2)/HDIF
230     CONTINUE

240     CONTINUE
        IF(IPRV.EQ.0) GOTO 300
        DO 245 J=1,NX(N)
245     WRITE(6,250) VISCT(N),VISC(N,J),OMEGA1(N),OMEGA2(N)
250     FORMAT(1X,' AT ',F7.2,' K VISCOSITY = ',E15.5,
       &' OMEGA1 = ',E15.5,' AND OMEGA2 = ',E15.5)
300     CONTINUE
```

```
      S=0.
C
C     Calculate deviation from experimental data
C
      DO 400 I=1,NT
      DO 400 J=1,NX(I)
      D=(VISC(I,J)-VISCD(I,J))/VISCE(I,J)
      S=S+D*D
400   CONTINUE
      IF(IVFLAG.EQ.1) NVIS=NT
      VISDEL2=S/FLOAT(NVIS)
      RETURN
      END
```

```
C
C       Test program for SUBROUTINE VISCOUS
C
        DIMENSION A(15),X(10),VA(10),VP(10)
        COMMON/PHSWTS/XQ(10),WQ(10),NXQ
        COMMON/POTX/V(2001),XM2(2001),XSTART,XSTEP,
       & RNPHASE,ERROR
        COMMON/VIS/ELOW,EHIGH,NEN,YIL,YSL,ESW,IPRV,
       & VISCD(25,10),VISC2(25)
       & ,VISCE(25,10),VISCT(25),NT,VISC(25,10),IVFLAG,SECM,
       & PRIM,VISC1(25),NX(25),NVIS,XMOLE(25,10)
        DIMENSION GXQ(10),GWQ(10)
C
C       Data for Gausian quadrature for JWKB phase shifts.
C
        DATA (GXQ(I),I=1,7)/.20119,.39415,.57097,.72442,.84821,.93727,
       & .98799/
        DATA (GWQ(I),I=1,7)/.19843,.18616,.16627,.13957,.10716,.07037,
       & .03075/
C
C       Read input data.
C       PRIM and SECM are the mass(es) of the components of the
C       gas. If PRIM=SECM then the gas is pure; if PRIM is not equal
C       to SECM then the gas is a binary mixture.
C
        READ(5,1) PRIM,SECM
        IVFLAG=1
        IF (PRIM.NE.SECM) IVFLAG=2
C
C       ELOW,EHIGH,YIL,YSL, and ESW are parameters that depend upon the
C       desired calculation, its accuracy and speed. See SUBROUTINE
C       VISCOUS for details.
C
        READ(5,1) ELOW,EHIGH,YIL,YSL,ESW
1       FORMAT(8F10.3)
C
C       XSTART,XSTEP,RNPHASE, and ERROR are used by the exact phase
C       shift routine. See M.F. Vernon thesis, U.C. Berekely 1981.
C
        READ(5,1) XSTART,XSTEP,RNPHASE,ERROR
C
C       NEN is the number of energies at which to calculate phase shifts.
```

```
C
      READ(5,2) NEN
2     FORMAT(I3)
C
C     Read in potential parameters, reduced mass and the number of
C     temperatures at which to calculate viscosities.
C
      READ(5,1) (A(I),I=1,15)
      READ(5,1) RM
      READ(5,2) NT
C
C     Write out input.
C
      WRITE(6,1) ELOW,EHIGH,YIL,YSL,ESW
      WRITE(6,2) NEN
      WRITE(6,1) (A(I),I=1,15)
      WRITE(6,1) RM
      WRITE(6,2) NT
      IF(IVFLAG.EQ.2) GOTO 203
C
C     If gas is pure, read in temperatures of viscosity data, the data
C     itself, and the associated uncertainty in the data.
C
      READ(5,1) (VISCT(I),VISCD(I,1),I=1,NT)
      READ(5,1) (VISCE(I,1),I=1,NT)
      WRITE(6,1) (VISCT(I),VISCD(I,1),I=1,NT)
      WRITE(6,1) (VISCE(I,1),I=1,NT)
      GOTO 204
C
C     If the gas is a binary mixture, read in the number of
C     mole fractions of component 1 at each temperature.
C
203   READ (5,2) (NX(I),I=1,NT)
      WRITE(6,2) (NX(I),I=1,NT)
      NVIS=0
      DO 201 I=1,NT
      NVIS=NVIS+NX(I)
C
C     Read in the viscosity temperatures and the pure viscosities
C     of the components at those temperatures.
C
      READ(5,1) VISCT(I),VISC1(I),VISC2(I)
```

```
      WRITE(6,1) VISCT(I),VISC1(I),VISC2(I)
C
C     Read in the mole fractions, experimental viscosities and errors.
C
      READ(5,1) (XMOLE(I,J),VISCD(I,J),VISCE(I,J),J=1,NX(I))
201   WRITE(6,1) (XMOLE(I,J),VISCD(I,J),VISCE(I,J),J=1,NX(I))
      WRITE(6,1) (VISCT(I),I=1,NT)
204   NXQ=7
C
C     Set up Gaussian quadrature for JWKB phase shifts.
C
      DO 5 I=1,NXQ
      XQ(I)=1.-GXQ(I)*GXQ(I)
      WQ(I)=2.*GXQ(I)*GXQ(I)*GWQ(I)
      5 CONTINUE
      WRITE(6,1) (XQ(I),WQ(I),I=1,NXQ)
      CALL VISCOUS(VISDEL2,A,RM)
C
C     Write out results.
C
      DO 200 I=1,NT
      IF(IVFLAG.EQ.1) NX(I)=1
      DO 200 J=1,NX(I)
      WRITE(6,100) VISCT(I),VISC(I,J),VISCD(I,J),VISCE(I,J)
100   FORMAT(1X,'AT ',F7.1,' VISC= ',F10.3,' EXPT= ',E15.5,' ERROR'
     &,'=',F5.2)
200   CONTINUE
      CALL EXIT
      END
```

B.4 References

[1] M.J. O'Loughlin, B.P. Reid, and R.K. Sparks, J. Chem. Phys. **85**, 5656, (1985).

[2] S. Chapman and T.G. Cowling , *The Mathematical Theory of Non-Uniform Gases* (Cambrige University Press, New York, 1952).

[3] J.O. Hirschfelder, C.F. Curtis, and R.B. Bird, *Molecular Theory of Gases and Liquids* (John Wiley and Sons, New York, 1954).

[4] T. Kihara, *Imperfect Gases* (Asakusa Bookstore, Tokyo, 1949).

[5] G.A. Parker and R.T Pack, J. Chem. Phys. **68**, 1597, (1978).

[6] R.T Pack, J. Chem. Phys. **70**, 3424, (1979).

[7] R.T Pack, J.J. Valentini, and J.B. Cross, J. Chem. Phys. **77**, 5486, (1982).

[8] M.F. Vernon, *Ph.D. Thesis* (University of California, Berkeley, 1981).

[9] M.J. O'Loughlin, *Ph.D. Thesis* (California Institute of Technology, Pasadena, 1986).

[10] R.B. Bernstein, , J. Chem. Phys. **33**, 795, (1960).

[11] M. Abromowitz and I.A. Stegun, editors, *Handbook of Mathematical Functions* (Dover Publications, New York, 1965).

Appendix C

Neon-Chlorine Time-of-Flight Data

This appendix lists the distributions of chlorine scattering from neon which were analyzed in Chapter 3. Included are data for both an angular and time-of-flight distributions. The angular intensity distributions include laboratory angle (Θ), intensity, and experimental uncertainty (Δ). The time-of-flight distributions have been normalized to the angular intensities. The time corresponding to the center of each channel is found by multiplying the channel number by 8 microseconds and subtracting on offset of 28 microseconds, which accounts for the ion flight time.

Table C.1. Neon-Chlorine angular distribution for collision energy 1476 K.

Θ	Intensity	Δ
6.0°	1575	10
10.0°	1000	2
14.0°	796	6
18.0°	701	4
22.0°	787	4
26.0°	848	3
30.0°	564	2

Table C.2. Neon-chlorine time-of-flight data for collision energy 1476 K.

Channel	6°	10°	14°	18°	22°	26°	30°
33	6	84	98	0	0	0	0
34	53	0	74	12	0	0	0
35	5	58	44	1	0	0	0
36	769	974	646	33	0	0	0
37	4489	4632	3026	1171	56	0	0
38	14046	11367	7681	4278	1022	0	0
39	25497	16630	11493	8325	3197	232	0
40	29293	15285	11003	10456	6062	1209	0
41	23239	10114	7343	9225	7721	3187	66
42	14577	5852	3970	6218	7778	5047	446
43	8689	3520	2347	3503	7098	5580	1118
44	5519	2339	1702	1873	5794	5199	2389
45	3810	1771	1335	983	4155	4747	3749
46	2578	1370	1034	535	2722	4416	4279
47	1831	1082	869	283	1599	4236	4139
48	1333	782	656	163	1081	4074	3645
49	968	599	504	153	695	3955	3154
50	772	628	549	177	516	3671	2754
51	688	480	483	118	436	3369	2542
52	658	483	367	199	501	3107	2297
53	550	386	264	162	635	2898	2101
54	271	284	191	48	610	2536	1986
55	309	237	205	113	739	2302	1891
56	180	225	156	190	907	2113	1780
57	73	146	99	183	1102	1943	1646
58	8	124	122	274	1258	1765	1569
59	-62	115	248	401	1281	1520	1585
60	268	229	389	680	1424	1418	1488
61	342	365	464	826	1506	1352	1368
62	531	488	598	934	1350	1232	1315
63	743	639	705	1092	1323	1157	1342

- continued -

Table C.2. continued

Channel	6°	10°	14°	18°	22°	26°	30°
64	937	750	910	1267	1352	1139	1163
65	1044	848	916	1239	1190	1103	1018
66	1214	1042	1123	1159	1119	1042	944
67	1387	1243	1186	1169	969	1016	886
68	1426	1273	1177	1121	910	932	760
69	1507	1237	1216	1071	933	942	594
70	1342	1170	1109	1053	1026	915	429
71	1185	1179	1069	975	931	853	330
72	1257	1163	1028	847	830	662	294
73	1268	1068	1034	891	882	623	282
74	1176	992	932	923	940	562	178
75	1046	879	875	784	769	439	71
76	753	811	806	712	627	325	72
77	637	732	722	558	484	273	134
78	551	716	734	615	506	202	2
79	385	558	641	440	314	151	4
80	393	543	623	393	255	104	0
81	501	454	485	367	216	105	0
82	419	413	380	312	172	123	0
83	222	283	311	149	99	50	0
84	136	201	258	106	59	19	17
85	267	278	243	155	119	91	22
86	217	155	220	108	115	27	0
87	74	82	176	30	58	23	35
88	145	274	203	86	144	51	0
89	191	240	201	70	76	45	0
90	134	151	151	74	20	1	98
91	104	220	103	96	96	89	69
92	156	148	174	111	186	87	49
93	107	119	155	97	68	104	0
94	136	80	133	68	128	53	23

Appendix D
Rotationally Inelastic Scattering Simulation

D.1 Computer Code

A computer code was developed to simulate the rotationally inelastic scattering described in Chapter 3. The program calculates laboratory time-of-flight spectra as well as laboratory total angular distributions (total differential cross sections) including proper transformation of the individual inelastic cross sections from the center-of-mass frame to the laboratory frame. The routine LSTSQ, an overall least squares fitting program employing MINPACK routines,[1] was modified from the elastic scattering program developed by Vernon at Berkeley.[2] The function which is used in the least squares routine, includes calls to the routine CMLB, a modified version of a reactive scattering program also developed at Berkeley.[3] CMLB calculates center-of-mass and laboratory coordinates for Newton diagrams corresponding to the experimental conditions. CMLB calls the routine EVAL which evaluates the scattering into a specified region in velocity space. EVAL is included below to describe the implementation of the IOSA equations presented in Chapter 3 which calculate the rotationally inelastic scattering. The potential and phase shift routines called in EVAL are similar to those described in Reference (2). EVAL uses vector and matrix routines available for the Floating Point Systems 164 attatched processor, to facilitate the quadrature needed for the IOS approximation. Standard FORTRAN routines which emulate these special FPS 164 routines are also included here.

```
C
C
C     ************************************************
      SUBROUTINE EVAL(A,NSET)
C     ************************************************
C
C
C     This routine is for use with a center-of-mass to lab
C     transformation program.
C
C     On the initial call this
C     routine determines center-of-mass differential
C     cross sections at given collision energies and center-of-
C     mass angles from 0 to 180 degrees for an atom-diatom collision,
C     using the Infinite Order Sudden approximation.
C
C     On subsequent calls scattering from
C     all transitions which can contribute to flux into a region
C     in laboratory velocity space is calculated from the
C     differential cross sections.
C
C     Written 1985-1986 Brian Reid
C
C
      DIMENSION P(250),V(75),DCS0(71,200,24)
      DIMENSION PG(80,80),PGT(80,80),CETA(250,80),SETA(250,80)
      DIMENSION CA(80,200),S(80,200),WGAMMA(80)
      DIMENSION ETA(250,12),COSGAM(80),A(15)
      DIMENSION TLP1(250),ANGLE(200),AI(12),XI(12),WI(12),PX(12,12)
      DIMENSION PXT(12,12),ETAT(12,250),ETAL(12,250)
      DIMENSION W2M(4),VLAB(8),TDCS(200,24),FC(80)
      DIMENSION TLAB(8),THETA(8),D1(75),D0(75),FS(80)
      DIMENSION XII(7),WII(7)
      DIMENSION VLIM2(2),BX(2)
C
C     The common blocks EVALS and SAVE are used for least
C     squares fitting of one or more sets of data.
C
      COMMON/EVALS/MAXJI,NETA,MAXJF,ROTJ(20)
      COMMON/SAVE/NVS(2,3),NGAMS(3),NGRIDS(3),HWIDBS(3),
     & VPARS(2,2,3),CXYZS(200,3,3),URS(200,3,3),
     & CMS(200,3,3),CS(200,3),ES(200,3),US(200,3),
     & FABGS(200,3),MIJKS(3),TPPS(200,3),CSQS(200,3)
     & ,THCS(200,3),NANGS(3),NVLS(3),V0S(3),VDS(3),ANGS(100,3)
     & ,BS(100,3),VLS(300,3),NATOFS(3),STDS(100,3),MAXJIS(3)
     & ,NETAS(3),MAXJFS(3),ROTJS(20,3),NSETS,GBS(2,3),GCMS(3)
     & ,G3S(3)
     & ,XCS(3),YCS(3),DRS(3),NDETS(3)
C
```

```
C       The common block WIGNER is used to store and retrieve Wigner
C       3-j coefficients.
C
        COMMON/WIGNER/W3J(900,76)
C
C       The common block NDPAR contains parameters associated
C       with each Newton diagram for which cross sections or
C       scattering may be calculated.
C
        COMMON/NDPAR/NONPL,NV(2), NGAM,NGRID,GB(2),GCM,G3
       & ,GAMMA,HWIDB,VPAR(2,2)
       & ,CXYZ(200,3),UR(200,3),CM(200,3),C(200),E(200),
       & U(200),FABG(200),MIJK,TPP(200),CSQ(200),THC(200)
C
C       The common block EVALN contains passes information about
C       the particular call to EVAL.
C
        COMMON/EVALN/ECM,PP,COLLEN,CTH,ESWITCH,LSWITCH,
       & COST,EP,NLEGV,PPP(16),BB(9),IJK,ALIM(2),VLIM(2),VALUE,
       & COSA(2),SINA(2),ALAB,ALIMA,ALIMB,ALIMC
        COMMON/PHSWTS/XQ(10),WQ(10),NXQ
        DIMENSION GXQ(10),GWQ(10)
        LOGICAL ESWITCH,LSWITCH
        DATA PI,PI2,U2TOEN/3.141592654,6.283185308,1.19503E-3/
        DATA LO/6/
C
C       Data for quadratures and interpolations are stored
C       in this section.
C
C       AI contains angles corresponding to the arccos of
C       the XI point of a KQUAD Gaussian quadrature.
C       WI are the associated quadrature weights.
C       These are the atom-molecule orientations at which
C       phase shifts are evaluated.
C
C       COSGAM contains the NQUAD points for a Gaussian
C       quadrature. WGAMMA contains the corresponding weights.
C       This is for integration over the atom-molecule orientations
C       to determine state-to-state differential cross sections.
C
C       GXQ and GWQ contain points and weights for Gaussian
C       to evaluate the JWKB phase shifts.
C
        DATA KQUAD/12/
        DATA AI/1.37846,1.12931,.878689,.627741,.376676,.125563,
       &-.125563,-.376676,-.627741,-.878689,-1.12931,-1.37846/
        DATA XI/-.981561,-.904117,-.769903,-.587318,-.367832,-.125233
       & ,.125233,.367832,.587318,.769903,.904117,.981561/
```

```
      DATA WI/.0471753,.106939,.160078,.203167,.233493,.249147
     & ,.249147,.233493,.203167,.160078,.106939,.0471753/
      DATA NQUAD/80/
      DATA (COSGAM(I),I=1,72)/-0.9995538226,-0.9976498643,
     & -0.9942275409,-0.9892913024,
     & -0.9828485727,-0.9749091405,-0.9654850890,-0.9545907663,
     & -0.9422427613,-0.9284598771,-0.9132631025,-0.8966755794,
     & -0.8787225676,-0.8594314066,-0.8388314735,-0.8169541386,
     & -0.7938327175,-0.7695024201,-0.7440002975,-0.7173651853,
     & -0.6896376443,-0.6608598989,-0.6310757730,-0.6003306228,
     & -0.5686712681,-0.5361459208,-0.5028041118,-0.4686966151,
     & -0.4338753708,-0.3983934058,-0.3623047534,-0.3256643707,
     & -0.2885280548,-0.2509523583,-0.2129945028,-0.1747122918,
     & -0.1361640228,-0.0974083984,-0.0585044371,-0.0195113832,
     & 0.0195113832, 0.0585044371, 0.0974083984, 0.1361640228,
     & 0.1747122918, 0.2129945028, 0.2509523583, 0.2885280548,
     & 0.3256643707, 0.3623047534, 0.3983934058, 0.4338753708,
     & 0.4686966151, 0.5028041118, 0.5361459208, 0.5686712681,
     & 0.6003306228, 0.6310757730, 0.6608598989, 0.6896376443,
     & 0.7173651853, 0.7440002975, 0.7695024201, 0.7938327175,
     & 0.8169541386, 0.8388314735, 0.8594314066, 0.8787225676,
     & 0.8966755794, 0.9132631025, 0.9284598771, 0.9422427613/
      DATA (COSGAM(I),I=73,80)/ 0.9545907663, 0.9654850890,
     & 0.9749091405, 0.9828485727,
     & 0.9892913024, 0.9942275409,
     & 0.9976498643, 0.9995538226/
      DATA (WGAMMA(I),I=1,72)/0.0011449500, 0.0026635335,
     & 0.0041803131, 0.0056909224,
     & 0.0071929047, 0.0086839452, 0.0101617660, 0.0116241141,
     & 0.0130687615, 0.0144935080, 0.0158961835, 0.0172746520,
     & 0.0186268142, 0.0199506108, 0.0212440261, 0.0225050902,
     & 0.0237318828, 0.0249225357, 0.0260752357, 0.0271882275,
     & 0.0282598160, 0.0292883695, 0.0302723217, 0.0312101741,
     & 0.0321004986, 0.0329419393, 0.0337332149, 0.0344731204,
     & 0.0351605290, 0.0357943939, 0.0363737499, 0.0368977146,
     & 0.0373654902, 0.0377763643, 0.0381297113, 0.0384249930,
     & 0.0386617597, 0.0388396510, 0.0389583959, 0.0390178136,
     & 0.0390178136, 0.0389583959, 0.0388396510, 0.0386617597,
     & 0.0384249930, 0.0381297113, 0.0377763643, 0.0373654902,
     & 0.0368977146, 0.0363737499, 0.0357943939, 0.0351605290,
     & 0.0344731204, 0.0337332149, 0.0329419393, 0.0321004986,
     & 0.0312101741, 0.0302723217, 0.0292883695, 0.0282598160,
     & 0.0271882275, 0.0260752357, 0.0249225357, 0.0237318828,
     & 0.0225050902, 0.0212440261, 0.0199506108, 0.0186268142,
     & 0.0172746520, 0.0158961835, 0.0144935080, 0.0130687615/
      DATA (WGAMMA(I),I=73,80)/
     & 0.0116241141, 0.0101617660, 0.0086839452, 0.0071929047,
     & 0.0056909224, 0.0041803131, 0.0026635335, 0.0011449500/
```

```
      DATA(GXQ(I),I=1,7)/.20119,.39415,.57097,.72442,.84821,
     & .93727,.98799/
      DATA(GWQ(I),I=1,7)/.19843,.18616,.16627,.13957,.10716,
     & .07037,.03075/
C
C     FORMAT statements for input.
C
      1 FORMAT(10F10.3)
      2 FORMAT(10I10)
C
      NLEGV=1
      IF(ESWITCH) GOTO 25
      IF(LSWITCH) GOTO 325
C
C     For initial time through read in necessary parameters and
C     do set up
C
C     PMASS = mass of primary beam in amu (g/mole)
C     SMASS = mass of secondary beam in amu (g/mole)
C     BE = rotational constant of diatomic molecule in kcal/mole (!)
C     MAXJI= maximum rotational state of initial distribution
C     MAXJF= maximum final rotational state considered
C     ISYM = 1 for heteronuclear diatomic molecule
C     ISYM = 2 for homonuclear diatomic molecule
C     ISYM = 3 for spherical calculation
C     MAXNFS = maximum number of final states needed for
C     JINITIAL=0 this is (MAXJF+1)/2 for isym=2
C     NETA = number of phase shifts used in cross section calculations
C     IPSP = print flag for phase shifts, 0=no printing 1=print
C     ROTJ(I) = relative population of ith initial rotational level
C     A() = set of potential parameters
C     JBSTEP = Every JBSTEP final J values use the same value of JBAR
C     in the ES part of the IOSA. For JBAR=0 for all
C     transitions use JBSTEP>MAXNFS. Using JBSTEP=1 will
C     calculate phase shifts for energies E-BE*JF*(JF+1)/2
C     for each J=0 to JF transition.
C
      READ(5,1) BE
      READ(5,2) MAXJI,NETA,IPSP,MAXJF,ISYM,JBSTEP
      ISYMS=ISYM
      IF(ISYM.NE.3) GOTO 26
      WRITE(LO,27)
27    FORMAT(' Calculation is spherical')
      ISYMS=1
C
C     NFLAG, NANG1, NANG2, NANG3, NANG4 are parameters to
C     determine the angles at which the differential cross sections
C     are calculated
```

```
C
26      READ (5,2) NFLAG,NANG1,NANG2,NANG
C
C       If NFLAG equals 0 then the differential cross section will be read
C       in from unit 4 using the same input format as output is done to unit 8.
C       If NFLAG equals 1 then dcs's are calculated but not written to unit 8.
C       If NFLAG equals 2 then dcs's are calculated and written to unit 8.
C
C       NANG1= no. of angles starting at 1 (zero degrees) to be spaced by
C       500ths of pi radians (.36 degrees).
C       NANG2= no. of angles starting at nang1+1 to be spaced by
C       200ths of pi radians (.9 degrees).
C       NANG= TOTAL no. of angles to fill to Pi radians
C
        IF (NFLAG.GT.0) GOTO 80
C
C       Read in angles from unit 4 if desired.
C
        OPEN(4,FILE='FOR004',STATUS='OLD')
        READ(4,8002) NANG,IDUM2
        READ(4,8003) (ANGLE(N),N=1,NANG)
        DO 804 IE=1,NGRID
        READ(4,8003) (TDCS(N,IE),N=1,NANG)
        DO 804 JFINAL=0,MAXJF+MAXJI,isymS
        READ(4,8002) JDUM
804     READ(4,8003) (DCS0(JFINAL+1,N,IE),N=1,NANG)
80      ANGLE(1)=0.
        do 81 I=2,nang1
81      ANGLE(I)=ANGLE(I-1)+.0062831853
        DO 82 I=NANG1+1,NANG2+NANG1
82      ANGLE(I)=ANGLE(I-1)+.0157079633
        NANG12=NANG1+NANG2
        DANG=(PI-ANGLE(NANG12))/(NANG-NANG12)
        DANGI=1./DANG
        DO 7 I=NANG12+1,NANG
        7 ANGLE(I)=ANGLE(I-1)+DANG
83      MAXNFS=(MAXJF+MAXJI)/ISYMS+1
        MAXJF1=MAXJF+1
        READ(5,1) (ROTJ(I),I=1,MAXJI+1)
        READ(5,1) (A(I),I=1,15)
C
C       Write out input.
C
        WRITE(LO,1002) GB(1),GB(2),BE,NETA
        WRITE(LO,1009) JBSTEP
        WRITE(10,1009) JBSTEP
        WRITE(LO,1003)
        WRITE(LO,1004) (I-1,ROTJ(I),I=1,MAXJI+1)
```

```
      write(LO,1006) MAXJF,MAXNFS
1006  FORMAT(' The maximum final J is ',i4,
     &' and the number of final states is ',i4,'.')
C     WRITE(LO,1005) (A(I),I=1,15)
      WRITE(10,1005) (A(I),I=1,15)
1002  FORMAT(/' Mass of primary beam = ',F10.4,
     &' Mass of secondary beam =',/,
     &F10.4,' Be = ',F10.5,' Number of phase shifts = ',I5)
1003  FORMAT(/' Initial rotational distribution (J and weight)')
1004  FORMAT(4(2X,I5,F8.4))
1005  FORMAT (' Potential parameters ',/,2(8F10.4,/))
1009  FORMAT (' Jbstep ',I10)
C
C     Get Wigner 3-J symbols needed for the determination of
C     the entire matrix of state-to-state dcs's from the first
C     column.
C     Symbols will be returned in two dimensional array W3J.
C     For J1,J2,J3 second array index is J1+1 and first array
C     index is (J2-J1)*((J1+2)/2)+(J3-J2+2)/2.
C     This array is not densely packed but don't worry about it.
C     The subroutine WIGVEC will make use of the array when we
C     need the symbols.
C
      CALL WIGNER3J
39    IF(NFLAG.EQ.0) RETURN
C
C     Set up gaussian quadruture points and weights for the semi-
C     classical phase shift routine.
C
      NXQ=7
      DO 15 I=1,NXQ
      XQ(I)=1.-GXQ(I)*GXQ(I)
      WQ(I)=2.*GXQ(I)*GXQ(I)*GWQ(I)
15    CONTINUE
C
C     Set up vectors to find coefficients of scattering intensity
C     expansion in Legendre polynomials.
C     PG(i,j) is an array of Legendre polynomials Pi(cos aj)
C     and PGT is its transpose.
C
      DO 11 KGAMMA=1,NQUAD
11    CALL LPOLY(COSGAM(KGAMMA),NQUAD,PG(1,KGAMMA))
      CALL MTRANS(PG,1,PGT,1,NQUAD,NQUAD)
C
C     Set up vectors to find coefficients of phase shift
C     expansion in Legendre polynomials.
C     PX and PXT are analogous to PG and PGT.
C
```

```
      DO 111 KX=1,KQUAD
111   CALL LPOLY(XI(KX),KQUAD,PX(1,KX))
      CALL MTRANS(PX,1,PXT,1,KQUAD,KQUAD)
C
C     PXT and PGT are column multiplied by the Gaussian quadrature
C     weights.
C
      DO 113 I=1,KQUAD
113   CALL VMUL(PXT(1,I),1,WI,1,PXT(1,I),1,KQUAD )
      DO 13 I=1,NQUAD
13    CALL VMUL(PGT(1,I),1,WGAMMA,1,PGT(1,I),1,NQUAD )
C
C     Set up vector of 2L+1.
C
      TLP1(1)=1
      DO 12 L=2,250
12    TLP1(L)=TLP1(L-1)+2
C
C     Phase shifts must be calculated for different orientation angles,
C     GAMMA, and for energies appropriate to a given transition. For
C     this first model I just use the initial collision energy.
C     KQUAD orientations are used. A(15) is assumed to be the
C     angle for the potential. The phase shift routine should
C     return ETA(L+1,KGAMMA) for the Lth phase shift at angle
C     GAMMA. The phase shifts are calculated at NGRID energy
C     points which are provided by the calling routine.
C
C     For ISYM=1 the calculation is for a heteronuclear diatom and the
C     maximum work must be done.
C     For ISYM=2 the calculation is for a homonuclear diatom and only
C     half the work need be done.
C     For ISYM=3 the calculation is for a spherical potential and even
C     less work is done.
C
      IF(ISYM.NE.3) GOTO 88
      KQSYM=1
      GOTO 89
88    KQSYM=KQUAD/ISYM
C
C     Save things for least squares with more than one set of data.
C
89    MAXJIS(NSET)=MAXJI
      NETAS(NSET)=NETA
      MAXJFS(NSET)=MAXJF
      CALL VMOV(ROTJ(1),1,ROTJS(1,NSET),1,20)
      RETURN
325   CONTINUE
C
```

```
C       RMASS is the reduced mass. FACTM, RKFACT and FMBE
C       are factors used in converting energy units, etc.
C
        PMASS=GB(1)
        SMASS=GB(2)
        RMASS=PMASS*SMASS/(PMASS+SMASS)
        FACTM=U2TOEN*PMASS*PMASS/RMASS
        RKFACT=1./(RMASS*20.747*4.)
        FMBE=FACTM/BE
        MAXFS=MAXJF+MAXJI
        MAXFS1=MAXJF+MAXJI+1
        MAXNFS=(MAXFS)/ISYMS+1
C
C       DELTAH and DELTAL are the max and min possible changes in
C       energy associated with inelastic transitions (in units of BE).
C
        DELTAH=MAXJF*(MAXJF1)
        DELTAL=-MAXJI*(MAXJI+1)
C
C       Set up weights for quadrature over detector limits.
C
        IQUAD=NDETS(NSET)
        CALL GLQ(IQUAD,-1.,1.,XII,WII)
        DO 110 I=1,NGRID
        DO 100 JFP1=1,MAXFS1,ISYMS
C
C       A dependence of JBAR in the IOSA upon the final J state
C       is included. This is done by asuming JBAR=
C       (SQRT(1+2*JF*JF+2*JF)-1)/2 for every JBSTEP final J value.
C
        JF=JFP1-1
        IF(BE*JF*JFP1.LT.E(I)) GOTO 218
        DO 219 N=1,NANG
        DCS0(JFP1,N,I)=0.
219     CONTINUE
        GOTO 100
218     IF(MOD(JF,JBSTEP).NE.0) GOTO 103
        ENERG=E(I)-.5*BE*JF*JFP1
        DO 220 KX=1,KQSYM
        A(15)=AI(KX)
        CALL PREPOT(A,RMASS)
220     CALL PHASE(ETA(1,KX),NETA,ENERG,1,A,RMASS,IPSP)
        IF (ISYM.EQ.2) GOTO 223
        IF (ISYM.EQ.1) GOTO 224
C
C       For spherical calculation. We now need to find the cosines and
C       sines of 2.*eta's. These manipulations are performed
C       vectorially. The routines are standard for a Floating Point
```

```
C       System Attached Processor. Standard FORTRAN routines are included
C       for general use.
C
        CALL VSMUL(ETA,1,2.,ETA, 1,NETA)
        CALL VCOS(ETA,1,CETA(1,1),1,NETA)
        CALL VSIN(ETA,1,SETA(1,1),1,NETA)
        CALL VSADD(CETA(1,1),1,-1.,CETA(1,1),1,NETA)
        CALL VMUL(CETA(1,1),1,TLP1,1,CETA(1,1), 1,NETA)
        CALL VMUL(SETA(1,1),1,TLP1,1,SETA(1,1), 1,NETA)
C
C       We now loop over all angles and take the vector product of P with
C       the cosine and sine of the vector ETA(L+1) for each GAMMA in order
C       to determine the scattering amplitude F(GAMMA).
C
        DO 350 N=1,NANG
        COSTHE=COS(ANGLE(N))
        CALL LPOLY(COSTHE,NETA,P)
C
C       We will take the vector product of P with the
C       cosine and sine of the vector ETA(L+1) for each GAMMA in order
C       to determine the scattering amplitude F(GAMMA).
C
        CALL DOTPR(CETA(1,1),1,P,1,CA(1,N),NETA)
        CALL DOTPR(SETA(1,1),1,P,1,S(1,N),NETA)
350     CONTINUE
C
C       For the spherical calculation there is only one dcs per angle.
C       It is the absolute square of the scattering amplitude and
C       is equal to the Total Differential Cross Section TDCS.
C       RK2 is a unit factor that should make the cross sections
C       come out in square angstroms.
C
        RK2=RKFACT/E(I)
        DO 3105 N=1,NANG
        FC3=CA(1,N)*CA(1,N)
        FS3=S(1,N)*S(1,N)
        TDCS(N,I)=FC3+FS3
        DCS0(1,N,I)=TDCS(N,I)*RK2
3105    CONTINUE
        CALL VSMUL(TDCS(1,I),1,RK2,TDCS(1,I), 1,NANG)
        GOTO 110
C
C       For homonuclear diatomic molecules the phase shifts
C       were calculated at only half of the orientations.
C       Now the other half of the symmetric array is filled in.
C       ETAT holds the transpose of this array.
C
223     DO 222 KX=1,KQSYM
```

```
222     CALL VMOV(ETA(1,KX),1,ETA(1,KQUAD+1-KX),1,NETA)
224     CALL MTRANS(ETA,1,ETAT,1,KQUAD,250)
C
C       Now the coefficients for expansion of the phase shifts
C       as a function of angle in KQUAD Legendre polynomials
C       are found and stored in ETAL. This is done by
C       using KQUAD quadrature and the phase shifts calculated
C       above.
C
        DO 230 L=1,NETA
        DO 225 KL=1,KQUAD
225     CALL DOTPR(ETAT(1,L),1,PXT(1,KL),1,ETAL(KL,L),KQUAD)
230     CALL VMUL(ETAL(1,L),1,TLP1,1,ETAL(1,L),1,KQUAD)
        NQUADS=NQUAD/ISYMS
        DO 50 KGAMMA=1,NQUADS
C
C       We need the phase shifts at the particluar angular orientation
C       for each point over the NQUAD Gauss-Legendre quadrature.
C       These are found from the expansion of ETA in KQUAD Legendre
C       polynomials.
C
        CALL LPOLY(COSGAM(KGAMMA),KQUAD,P)
        DO 49 L=1,NETA
49      CALL DOTPR(ETAL(1,L),1,P(1),1,ETA(L,1),KQUAD)
C
C       We really need the (2L+1)SIN(2*ETA) and (2L+1)(1-COS(2*ETA))
C       But we do not need to multiply ETA'S by 2 since the ETAL'S were
C       twice as large as they ought to have been (they were not divided
C       by two when calculated).
C       CALL VSMUL(ETA,1,2.,ETA,1,NETA)
C
C       This is similar to section above for spherical calculation.
C
        CALL VCOS(ETA,1,CETA(1,KGAMMA),1,NETA)
        CALL VSIN(ETA,1,SETA(1,KGAMMA),1,NETA)
        CALL VSADD(CETA(1,KGAMMA),1,-1.,CETA(1,KGAMMA),
        & 1,NETA)
        CALL VMUL(CETA(1,KGAMMA),1,TLP1,1,
        & CETA(1,KGAMMA), 1,NETA)
        CALL VMUL(SETA(1,KGAMMA),1,TLP1,1,
        & SETA(1,KGAMMA), 1,NETA)
        DO 50 N=1,NANG
        COSTHE=COS(ANGLE(N))
        CALL LPOLY(COSTHE,NETA,P)
C
C       We take the vector product of P with the
C       cosine and sine of the vector ETA(L+1) for each GAMMA in order
C       to determine the scattering amplitude F(GAMMA).
```

```
C
      CALL DOTPR(CETA(1,KGAMMA),1,P,1,CA(KGAMMA,N),NETA)
      CALL DOTPR(SETA(1,KGAMMA),1,P,1,S(KGAMMA,N),NETA)
50    CONTINUE
C
C     Now the differential cross sections for J=0 to JFINAL are
C     calculated for JFINAL from 0 to MXJFIN. This is done by
C     averaging the scattering amplitude over the rotational
C     wavefunctions for J=0 and JFINAL. These are just Legendre
C     polynomials (with angular momentum quantum numbers m=0).
C
      RK2=RKFACT/E(I)
103   DO 104 N=1,NANG
      if(jf.ne.0) goto 102
      CALL VMUL(CA(1,N),1,CA(1,N),1,FC, 1,NQUADS)
      CALL VMUL(S(1,N),1,S(1,N),1,FS, 1,NQUADS)
      CALL VADD(FS,1,FC,1,FC,1,NQUADS)
      CALL DOTPR(FC,1,WGAMMA,1,TDCS(N,I),NQUADS)
102   CALL DOTPR(Ca(1,N),1,PGT(1,JFP1),1,F1,NQUADS)
      CALL DOTPR(S(1,N),1,PGT(1,JFP1),1,F2,NQUADS)
      DCS0(JFP1,N,I)=F1*F1+F2*F2
104   CONTINUE
100   CONTINUE
      DO 105 N=1,NANG
      CALL VMUL(DCS0(1,N,I),ISYMS,TLP1,ISYMS,DCS0(1,N,I),
     &ISYMS,MAXNFS)
      CALL VSMUL(DCS0(1,N,I),ISYMS,
     &isyms*.5*RK2,DCS0(1,N,I),ISYMS,MAXNFS)
105   CONTINUE
      CALL VSMUL(TDCS(1,I),1,isyms*.5*RK2,TDCS(1,I), 1,NANG)
110   CONTINUE
      IF (NFLAG.NE.2) GOTO 8005
      OPEN(8,FILE='FOR008',STATUS='NEW')
      WRITE(8,8002) NANG,MAXFS1
8002  FORMAT(I10)
      WRITE(8,8003) (ANGLE(N),N=1,NANG)
8003  FORMAT(8e15.8)
      DO 8004 IE=1,NGRID
      WRITE(8,8003) (TDCS(N,IE),N=1,NANG)
      DO 8004 JFINAL=0,MAXFS,isym
      WRITE(8,8002) JFINAL
8004  WRITE(8,8003) (DCS0(JFINAL+1,N,IE),N=1,NANG)
C
C     Return here after initial call.
C
8005  RETURN
25    CONTINUE
C
```

```
C       If this is not the initial call the scattering intensity over
C       the laboratory observation area in velocity space needs to be
C       calculated. The input data to define this area are VLIM(1) and
C       VLIM(2) and ALIM(1) and ALIM(2). For both vectors value 1
C       should be less than value 2. VLIM defines the laboratory velocity
C       limits and ALIM defines the detector angular resolution limits.
C
C       C1 and C2 are the x and y components of the center-of-mass
C       velocity vector. PPP(1) and VALUE are both the scattering intensity
C       which is returned.
C
        C1=CM(IJK,1)
        C2=CM(IJK,2)
        C2SQ=C2*C2
        VALUE=0.
        PPP(1)=0.
C
C       Check for center of mass vector being in velocity region.
C       Ignore the case when it is. THC(IJK) is the angle the c-o-m
C       velocity makes with the primary beam.
C
        IF(ALIM(2).LT.THC(IJK)) GOTO 499
        IF(ALIM(1).GT.THC(IJK)) GOTO 499
        IF(VLIM(2).LT.C(IJK)) GOTO 499
        IF(VLIM(1).GT.C(IJK)) GOTO 499
        RETURN
499     K=0
C
C       We calculate the maximum and minimum velocities in the
C       center of mass frame which could give scattering into the
C       observation area. This is a geometry problem.
C
        DO 602 I=1,2
        BX(I)=C1*COSA(I)+C2*SINA(I)
        VLIM2(I)=VLIM(I)*VLIM(I)
        DO 603 J=1,2
        K=K+1
        WX=VLIM(I)*COSA(J)-C1
        WY=VLIM(I)*SINA(J)-C2
        W2M(K)=WX*WX+WY*WY
603     CONTINUE
602     CONTINUE
        W2MAX=AMAX1(W2M(1),W2M(2),W2M(3),W2M(4))
        W2MIN=AMIN1(W2M(1),W2M(2),W2M(3),W2M(4))
        ICASE=1
        IF(ALIM(2).LT.THC(IJK)) ICASE=2
        WP=C1*SINA(ICASE)-C2*COSA(ICASE)
        W2P=WP*WP
```

```
      V2P=CSQ(IJK)-W2P
      IF(V2P.LE.VLIM2(1)) GOTO 496
      IF(V2P.GE.VLIM2(2)) GOTO 496
497   W2MIN=AMIN1(W2MIN,W2P)
496   CBE=COLLEN/BE
C
C     Check to make sure any scattering is possible.
C
      DEMIN=CBE-FMBE*W2MAX
      DEMAX=CBE-FMBE*W2MIN
      IF(DEMIN.GT.DELTAH) RETURN
      IF(DEMAX.LT.DELTAL) RETURN
C
C     Now loop over initial and final rotational states to determine
C     transitions whose Newton circles intersect the observation region
C     and where the intersection occurs.
C
      DO 10 JI=0,MAXJI
C
C     Once the initial state, JI, is chosen, only a select
C     range of final states, JF, are possible. They also must
C     be of the same parity if the diatom is symmetric.
C     This is another geometry problem.
C
      JI1=JI+1
      ENJ=JI1*JI
      DISC=DEMIN+ENJ
      IF (DISC.GE.0.) GOTO 606
      JFS=0
      GOTO 607
606   CJ=(-1.+SQRT(1.+4.*DISC))*.5
      JFS=INT(CJ+1.)
607   JDIF=ABS(JI-JFS)
      JFS=JFS+MOD(JDIF,ISYMS)
      DISC=DEMAX+ENJ
      IF (DISC.LT.0.) GOTO 10
      CJ=(-1.+SQRT(1.+4.*DISC))*.5
      JFE=INT(CJ)
      JDIF=ABS(JI-JFE)
      JFE=JFE-MOD(JDIF,ISYMS)
      IF (JFS.GT.MAXJF) GOTO 10
      IF (JFE.LT.JFS) GOTO 10
      IF (JFE.GT.MAXJF) JFE=MAXJF-MOD(MAXJF-JI,ISYMS)
C
C     Now we have the final state range, from JFS to JFE.
C
      DO 20 JF=JFS,JFE,ISYM
C
```

```
C       Find max and min angular momentum q-numbers which
C       can add with JI and JF.
C
C       MAXJP1 = maximum J prime plus 1
C       MINJP1 = minimum J prime plus 1
C
        MINJP=ABS(JF-JI)
        MINJP1=MINJP+1+MOD(MINJP,ISYMS)
        MAXJP=JF+JI
        MAXJP1=MAXJP+1-MOD(MAXJP,ISYMS)
        JPDELTA=(MAXJP1-MINJP1)/ISYMS+1
        IPOINT=0
        JF1=JF+1
C
C       DELTAE is the difference between the initial collison energy
C       and the final product translational energy. COLLEN is the
C       collision energy. W is the final velocity in the center of
C       mass system.
C
        DELTAE=BE*(JF1*JF-JI1*JI)
        SCATEN=COLLEN-DELTAE
        W2=SCATEN/FACTM
        W=SQRT(W2)
C
C       At this point we try to find intersections of the
C       Newton circle with radius W with ALIM'S. More geometry.
C       The number of intersections which will give scattering
C       contributions to the selected area is indexed by IPOINT.
C       The laboratory coordinates of these intersections are
C       kept in VLAB() and TLAB().
C
        DO 609 I=1,2
        B=BX(I)
        DISC=B*B-CSQ(IJK)+W2
        IF (DISC.LT.0.) GOTO 609
        SR=SQRT(DISC)
        VTRY=B+SR
        IF(VTRY.LT.VLIM(1)) GOTO 1609
        IF(VTRY.GT.VLIM(2)) GOTO 1609
        IPOINT=IPOINT+1
        VLAB(IPOINT)=VTRY
        TLAB(IPOINT)=ALIM(I)
1609    VTRY=B-SR
        IF(VTRY.LT.VLIM(1)) GOTO 609
        IF(VTRY.GT.VLIM(2)) GOTO 609
        IPOINT=IPOINT+1
        VLAB(IPOINT)=VTRY
        TLAB(IPOINT)=ALIM(I)
```

```
609     CONTINUE
C
C       Now find intersections with VLIM'S.
C
        DO 610 I=1,2
        BIG=AMAX1(VLIM(I),C(IJK),W)
        IF(BIG.GE.VLIM(I)+C(IJK)+W-BIG) GOTO 610
        CALPHA=(VLIM2(I)+CSQ(IJK)-W2)/(VLIM(I)*2.*C(IJK))
        ALPHA=ACOS(CALPHA)
        ATTRY=THC(IJK)-ALPHA
        IF(ATTRY.LT.ALIM(1)) GOTO 1610
        IF(ATTRY.GT.ALIM(2)) GOTO 1610
        IPOINT=IPOINT+1
        VLAB(IPOINT)=VLIM(I)
        TLAB(IPOINT)=ATTRY
1610    ATTRY=THC(IJK)+ALPHA
        IF(ATTRY.LT.ALIM(1)) GOTO 610
        IF(ATTRY.GT.ALIM(2)) GOTO 610
        IPOINT=IPOINT+1
        VLAB(IPOINT)=VLIM(I)
        TLAB(IPOINT)=ATTRY
610     CONTINUE
        IF(IPOINT.EQ.0) GOTO 20
C
C       Now integrate over THETA in the center of mass frame.
C       To do this we need to find the limits for integration in order
C       of increasing THETA.
C
637     DO 611 I=1,IPOINT
        WX=VLAB(I)*COS(TLAB(I))-C1
        WY=VLAB(I)*SIN(TLAB(I))-C2
        TP=ATAN(WY/WX)
        IF(WX.GT.0.) GOTO 640
        IF(WY) 638,640,639
638     TP=TP-PI
        GOTO 640
639     TP=TP+PI
640     THETA(I)=TP-TPP(IJK)
        IF(THETA(I).GT.PI) THETA(I)=THETA(I)-PI2
611     CONTINUE
C
C       Need to do bubble sort for THETA.
C
        IFLAG=0
660     DO 612 I=1,IPOINT-1
        DO 613 I2=I+1,IPOINT
        TSAVE=THETA(I)
        VSAVE=VLAB(I)
```

```
      IF(THETA(I2).GT.TSAVE) GOTO 613
      THETA(I)=THETA(I2)
      THETA(I2)=TSAVE
      VLAB(I)=VLAB(I2)
      VLAB(I2)=VSAVE
613   CONTINUE
612   CONTINUE
      IF (IFLAG.EQ.1) GOTO 661
C
C     IPOINT should be even, if it isn't then something's wrong
C
      IP2=IPOINT/2
C
C     Check to see if intersection points overlap the discontinuity
C     in the angular region for THETA, -pi to pi.
C
      DO 650 IN=1,IP2
      THETA1=THETA(IN*2-1)
      THETA2=THETA(IN*2)
      THETAB=THETA2-THETA1
      IF (THETAB.LT.PI) GOTO 650
      IFLAG=1
      THETA(IN*2-1)=THETA1+PI2
650   CONTINUE
      IF(IFLAG.EQ.1) GOTO 660
C
C     Now do IP2 integrations over THETAC
C     This is done by IQUAD point Gauss-Legendre quadrature.
C
661   DO 620 IN=1,IP2
      IN2=IN*2
      IN1=IN2-1
      THETA1=THETA(IN1)
      THETA2=THETA(IN2)
      THETAA=THETA2+THETA1
      THETAB=THETA2-THETA1
      QU=0.
      DO 621 IQ=1,IQUAD
C
C     Calculate THETAs needed for IQUAD point quadratue.
C
      TQ=(THETAB*XII(IQ)+THETAA)*.5
      OTQ=TQ
      IF(TQ.LT.0.) TQ=-TQ
      IF(TQ.GT.PI) TQ=PI2-TQ
C
C     DETWET accounts for the trapezoidal weighting function
C     over the effective detector size. To determine DETWET
```

```
C       The lab angle corresponding to TQ must be found.
C
        WLA=TPP(IJK)+OTQ
        XL=W*COS(WLA)+C1
        YL=W*SIN(WLA)+C2
        TL=ATAN(YL/XL)
        XTL=ABS(TL-ALIMA)*ALIMB
        DETWET=AMIN1(1.,(1.-XTL)*ALIMC)
        IF(TQ.GT.ANGLE(NANG12)) GOTO 631
        IF(TQ.GT.ANGLE(NANG1)) GOTO 630
        KA=INT(TQ*159.1549431)+2
        GOTO 632
630     KA=NANG1+INT((TQ-ANGLE(NANG1))*63.66197724)+1
        GOTO 632
631     KA=INT((TQ-ANGLE(NANG12))*DANGI)+NANG12+1
        KA=MIN(KA,NANG)
632     CONTINUE
C
C       Linearly interpolate DCS0 as a function of angle from the
C       table of DSC0's calculate in the initial call.
C
623     SS=1./(ANGLE(KA)-ANGLE(KA-1))
        T1=(ANGLE(KA)-TQ)*SS
        T2=(TQ-ANGLE(KA-1))*SS
        CALL VSMUL(DCS0(MINJP1,KA,IJK),ISYMS,T1,
        & D1,ISYMS,JPDELTA)
        CALL VSMUL(DCS0(MINJP1,KA-1,IJK),ISYMS,T2,
       & D0,ISYMS,JPDELTA)
        CALL VADD(D1,ISYMS,D0,ISYMS,D0,ISYMS,JPDELTA)
C
C       The dcs for ji to jf may be calculated from the
C       j=0 to jfinal dcs's via a sum over Wigner 3J coefficients.
C       These are retrieved by WIGVEC and the sum is done as
C       a dot product.
C
        CALL WIGVEC(JI,JF,V)
        CALL DOTPR(V,ISYMS,D0,ISYMS,F,JPDELTA)
C
C       Multiplication by THETAB completes the integration over
C       the center of mass theta. Multiplication by VLABA is in
C       the Jacobian for the center-of-mass phi to lab phi
C       transformation, but this is left out here
C       and we won't divided by it in CMLB. This is only
C       good for number density detection. For flux
C       detection please multiply by VLABA.
C
621     QU=QU+(2.*JF+1.)*F*THETAB*WII(IQ)*DETWET
620     CONTINUE
```

```
C
C       Divide by cm velocity which is in Jacobian for
C       center of mass phi to lab phi transformation.
C       The laboratory value of sin(Θ_lab)Δ(Φ_lab)
C       is assumed to remain constant.
C
        VALUE=VALUE+QU*ROTJ(JI1)/W
C
C       A factor for adjusting k^2's is left out as an approximation.
C       The calculations are performed at
C       constant collision energy and not constant total energy. This
C       differs by the initial rotational energy of the diatom which
C       is assumed to be small.
C
20      CONTINUE
10      CONTINUE
C       At this point we have calculated the number of particle
C       entering the detector with velocitites
C       in the selected range per unit time per unit incident flux.
C
        PPP(1)=VALUE
        RETURN
        END
```

```
C     ************************************************************
C
      SUBROUTINE LPOLY(CTH,NETA,P)
      IMPLICIT DOUBLE PRECISION (A-H,O-Z)
C
C     Subroutine to calculate legendre polynomials of COS(CTH)
C     from order zero up to NETA
C     adapted from SUBROUTINE INTENS
C     of PROGRAM ELASTIC by M.F. Vernon
C
      DIMENSION P(1000)
      X=CTH
C
C     INITIALIZE RECURSION LOOP
C
      P(1)=1.
      P(2)=X
      P0=1.
      P1=X
      DEL=3.
C
C     DO RECURSION
C
      DO 50 I=3,NETA
      P2=(DEL*X*P1-FLOAT(I-2)*P0)/FLOAT(I-1)
      P(I)=P2
C
C     UPDATE RECURSION
C
      P0=P1
      P1=P2
      DEL=DEL+2.
50    CONTINUE
C
C     THAT'S ALL.
C
      RETURN
      END
C
C     ************************************************************
C     ************************************************************
C
```

```
      SUBROUTINE WIGNER3J
      IMPLICIT DOUBLE PRECISION (A-H,O-Z)
C
C     Subroutine to produce the squares of M1=0,M2=0, M3=0 Wigner 3-J
C     symbols for integral J
C
C     Program will produce an array up to J1, J2, J3= JMAX
C     (actually J2,J3 go up to 3*JMAX/2 for some cases)
C     JMAX should be even.
C
C     The array produced is a something by JMAX2+1 array and looks
C     something like this:
C
C     (0 1 1) (1 1 2) (2 2 2) (3 3 4) ...
C     (0 2 2) (1 2 3) (2 2 4) (3 3 6) ...
C     (0 3 3) (1 3 4) (2 3 3) (3 4 5) ...
C     (0 4 4) (1 4 5) (2 3 5) (3 4 7) ...
C     (0 5 5) (1 5 6) (2 4 4) (3 5 6) ...
C     (0 6 6) ...
C     .
C     .
C     .
C
C     The three numbers in each triplet stand for J1, J2 and J3
C     JMAX has been abrieviated by J.
C     The symbols stand for Wigner 3-J symbols without the M values
C     and all other possible symbols
C     are either permutations of the above or have the value of zero.
C
C     This version has space for JMAX=75 so the dimensions of the
C     array are C(860,76).
C
      COMMON/WIGNER/C(860,76)
      JMAX=75
      IX=(3*JMAX)/2
C
C     KC WILL LABEL ARRAY COLUMNS
C     KR WILL LABEL ARRAY ROWS
C
C     CALCULATE FIRST COLUMN
C
      KC=1
```

```
      DO 10 KR=1,IX
10    C(KR,KC)=1./(2.*(KR-1)+1.)
C
C     CALCULATE OTHER COLUMNS IN LOWER PART OF ARRAY A
C
      MX=JMAX+1
      DO 20 KC=2,MX
      J1=KC-1
      R3=FLOAT(J1)
      DO 20 J2=J1,MAX(IX-J1,JMAX)
      J1EVEN=((J1+1)/2)*2-J1
      DO 20 J3=J2+J1EVEN,J1+J2,2
      J=J1+J2+J3
      R=FLOAT(J)
      R2=FLOAT(J2)
      KR=(J2-J1)*((J1+2)/2)+(J3-J2+2)/2
      KOC=J1
      JO1=J1-1
      IF(J2.EQ.J3) GOTO 14
      JO2=J2+1
      JO3=J3
      GOTO 16
14    JO2=J3
      JO3=J2+1
16    KOR=(JO2-JO1)*((JO1+2)/2)+(JO3-JO2+2)/2
      C(KR,KC)=C(KOR,KOC)*(R-2.*R2-1)*(R-2.*R3+2.)/
     &((R-2.*R2)*(R-2.*R3+1.))
20    CONTINUE
C
C     THIS SECTION IS FOR WRITING OUT THE COEFFICIENTS
C     IT IS NOT NECESSARY AS A SUBROUTINE
C
C     DO 40 J1=0,30
C     DO 40 J2=J1,30
C     DO 40 J3=J2,30
C     J=J1+J2+J3
C     JODD=(J/2)*2
C     IF (JODD.NE.J) GOTO 40
C     IF (J1+J2.LT.J3) GOTO 40
C     KC=J1+1
C     KR=(J2-J1)*((J1+2)/2)+(J3-J2+2)/2
C     VALUE=C(KR,KC)
```

```
C       WRITE(6,100) J1,J2,J3,VALUE
C       40 CONTINUE
C       100 FORMAT(1X,'(',I2,',',I2,',',I2,')',F8.5)
        RETURN
        END
C
C       ************************************************************
C       ************************************************************
C
        SUBROUTINE WIGVEC(J1,J3,V)
        IMPLICIT DOUBLE PRECISION (A-H,O-Z)
C
C       This subroutine returns a vector of the squares of Wigner 3-J
C       coefficients having the J1 and J3 given. It will do this for
C       J2 up to JMAX=75
C
        DIMENSION V(76)
        COMMON/WIGNER/C(860,76)
        DO 100 J2=0,75
        J=J1+J2+J3
        JE=(J/2)*2
        IF (J.NE.JE) GOTO 50
        K=3
        IF (J1.GT.J3) K=1
        IF (J2.GT.J1.AND.J2.GT.J3) K=2
        L=1
        IF (J2.LT.J1) L=2
        IF (J3.LT.J1.AND.J3.LT.J2) L=3
        JA=J1
        JB=J2
        JC=J3
        GOTO (10,20,30),K
10      GOTO (40,12,13),L
12      JA=J2
        JB=J3
        JC=J1
        GOTO 40
13      JA=J3
        JB=J2
        JC=J1
        GOTO 40
20      GOTO (21,40,23),L
```

```
21      JA=J1
        JB=J3
        JC=J2
        GOTO 40
23      JA=J3
        JB=J1
        JC=J2
        GOTO 40
30      GOTO (40,32,40),L
32      JA=J2
        JB=J1
        JC=J3
40      IF(JA+JB.LT.JC) GOTO 50
        KR=(JB-JA)*((JA+2)/2)+(JC-JB+2)/2
        KC=JA+1
        V(J2+1)=C(KR,KC)
        GOTO 100
50      V(J2+1)=0.
100     CONTINUE
        RETURN
        END
```

```
C
C
C       LIBRARY OF STANDARD FORTRAN ROUTINES
C       TO SIMULATE APMATH CALLS USED BY THE
C       FPS 164 ARRAY PROCESSOR
C
        SUBROUTINE DOTPR(A,IA,B,IB,C,N)
C       VECTOR PRODUCT
        DIMENSION A(IA*N),B(IB*N)
        C=0.
        JA=1
        JB=1
        DO 200 J=1,N
        C=C+A(JA)*B(JB)
        JA=JA+IA
        JB=JB+IB
200     CONTINUE
        RETURN
        END
C
C
        SUBROUTINE VMOV(A,IA,B,IB,N)
C       VECTOR MOVE
        DIMENSION A(IA*N),B(IB*N)
        JA=1
        JB=1
        DO 200 J=1,N
        B(JB)=A(JA)
        JA=JA+IA
        JB=JB+IB
200     CONTINUE
        RETURN
        END
C
C
        SUBROUTINE VSUB(A,IA,B,IB,C,IC,N)
C       VECTOR SUBTRACT
        DIMENSION A(IA*N),B(IB*N),C(IC*N)
        JA=1
        JB=1
        JC=1
        DO 200 J=1,N
        C(JC)=B(JB)-A(JA)
        JA=JA+IA
```

```
      JB=JB+IB
      JC=JC+IC
200   CONTINUE
      RETURN
      END
C
      SUBROUTINE VADD(A,IA,B,IB,C,IC,N)
C     VECTOR ADD
      DIMENSION A(IA*N),B(IB*N),C(IC*N)
      JA=1
      JB=1
      JC=1
      DO 200 J=1,N
      C(JC)=B(JB)+A(JA)
      JA=JA+IA
      JB=JB+IB
      JC=JC+IC
200   CONTINUE
      RETURN
      END
C
C
      SUBROUTINE VSIN(A,IA,B,IB,N)
C     SINE OF VECTOR
      DIMENSION A(IA*N),B(IB*N)
      JA=1
      JB=1
      DO 200 J=1,N
      B(JB)=SIN(A(JA))
      JA=JA+IA
      JB=JB+IB
200   CONTINUE
      RETURN
      END
C
C
      SUBROUTINE VSQ(A,IA,B,IB,N)
C     SQUARE COMPONENTS OF VECTOR
      DIMENSION A(IA*N),B(IB*N)
      JA=1
      JB=1
      DO 200 J=1,N
      B(JB)=A(JA)*A(JA)
      JA=JA+IA
```

```
      JB=JB+IB
200   CONTINUE
      RETURN
      END
C
C
      SUBROUTINE VCLR(A,IA,N)
C     CLEAR COMPONENTS OF VECTOR
      DIMENSION A(IA*N)
      JA=1
      DO 200 J=1,N
      A(JA)=0.
      JA=JA+IA
200   CONTINUE
      RETURN
      END
C
      SUBROUTINE VCOS(A,IA,B,IB,N)
C     VECTOR COSINE
      DIMENSION A(IA*N),B(IB*N)
      JA=1
      JB=1
      DO 200 J=1,N
      B(JB)=COS(A(JA))
      JA=JA+IA
      JB=JB+IB
200   CONTINUE
      RETURN
      END
C
      SUBROUTINE VSADD(A,IA,B,C,IC,N)
C     VECTOR SCALAR ADD
      DIMENSION A(IA*N),C(IC*N)
      JA=1
      JC=1
      DO 200 J=1,N
      C(JC)=B+A(JA)
      JA=JA+IA
      JC=JC+IC
200   CONTINUE
      RETURN
      END
C
C
```

```
      SUBROUTINE VSMUL(A,IA,B,C,IC,N)
C     VECTOR SCALAR MULTIPLY
      DIMENSION A(IA*N),C(IC*N)
      JA=1
      JC=1
      DO 200 J=1,N
      C(JC)=B*A(JA)
      JA=JA+IA
      JC=JC+IC
200   CONTINUE
      RETURN
      END
C
C
      SUBROUTINE VMUL(A,IA,B,IB,C,IC,N)
C     VECTOR MULTIPLY
      DIMENSION A(IA*N),B(IB*N),C(IC*N)
      JA=1
      JB=1
      JC=1
      DO 200 J=1,N
      C(JC)=A(JA)*B(JB)
      JA=JA+IA
      JB=JB+IB
      JC=JC+IC
200   CONTINUE
      RETURN
      END
C
C
      SUBROUTINE MTRANS(A,IA,B,IB,IC,IR)
C     MATRIX TRANSPOSE
      DIMENSION A(IR,IC),B(IC,IR)
      DO 200 JC=1,IC
      DO 200 JR=1,IR
      B(JC,JR)=A(JR,JC)
200   CONTINUE
      RETURN
      END
```

D.2 References

[1] B.S. Garbow, K.E. Hillstrom, and J.J. More, Argonne National Laboratory, Minpack Project (1980).

[2] M.F. Vernon, *Ph.D Thesis* (University of California Berkeley, 1979).

[3] K. Shobatake and R.K. Sparks, unpublished.